REPORT DOCUMENTATION PAGE

Public reporting burden for this collection of information is estimated to average 1 hour per response, including the time for reviewing instructions, searching existing data sources, gathering and maintaining the data needed, and completing and reviewing the collection of information. Send comments regarding this burden estimate or any other aspect of this collection of information, including suggestions for reducing this burden, to Washington Headquarters Services, Directorate for Information Operations and Reports, 1215 Jefferson Davis Highway, Suite 1204, Arlington, VA 22202-4302, and to the Office of Management and Budget, Paperwork Reduction Project (0704-0188), Washington, DC 20503.

1. AGENCY USE ONLY (Leave blank)	2. REPORT DATE 2/12/96	3. REPORT TYPE AND DATES COVERED Final for 1 Apr 93 - 31 Mar. 94

4. TITLE AND SUBTITLE

EXPERIMENTS IN HIGH-PERFORMANCE CONTROL OF A MULTI LINK FLEXIBLE MANIPULATOR WITH A MINI MANIPULATOR

5. FUNDING NUMBERS

F49620-93-1-0248-P00001

6. AUTHOR(S)

William L. Ballhaus
Prof. Stephen M. Rock, Principal Advisor

7. PERFORMING ORGANIZATION NAME(S) AND ADDRESS(ES)

Aerospace Robotics Laboratory
Department of Aeronautics and Astronautics
Stanford University
Stanford, CA 94305

8. PERFORMING ORGANIZATION REPORT NUMBER

SUDAAR 649

9. SPONSORING/MONITORING AGENCY NAME(S) AND ADDRESS(ES)

N/A

AFOSR/NA
Bolling AFB
Washington, DC 20332-6448

AFOSR-TR-96

11. SUPPLEMENTARY NOTES

12a. DISTRIBUTION/AVAILABILITY STATEMENT

Approved for public release,
distribution unlimited

12b. DISTRIBUTION CODE

13. ABSTRACT (Maximum 200 words)

Space-based manipulator systems like the Shuttle Remote Manipulation System contain long slender links that are inherently very flexible, which flexibility slows and degrades end-point position performance and makes high-performance control difficult. This project's research focuses on increasing the achievable slew and end-point performance of multi-link flexible manipulators through use of a small, high-bandwidth rigid robot at the tip, together with direct end-point sensing. A new soft-terminal-control approach has been developed for multi-link flexible manipulators that exploits both high-bandwidth local-manipulation capability and the redundancy intro-duced by the mani-manipulator, and the fact that the flexible main arm can be positioned more quickly to be within an area than it can be position to be at a point. In developing this new control approach, fundamental advances were made in trajectory generation, feedback-control design, and modelling of multi-link flexible manipulators.

19960614 078

14. SUBJECT TERMS

15. NUMBER OF PAGES 160

16. PRICE CODE

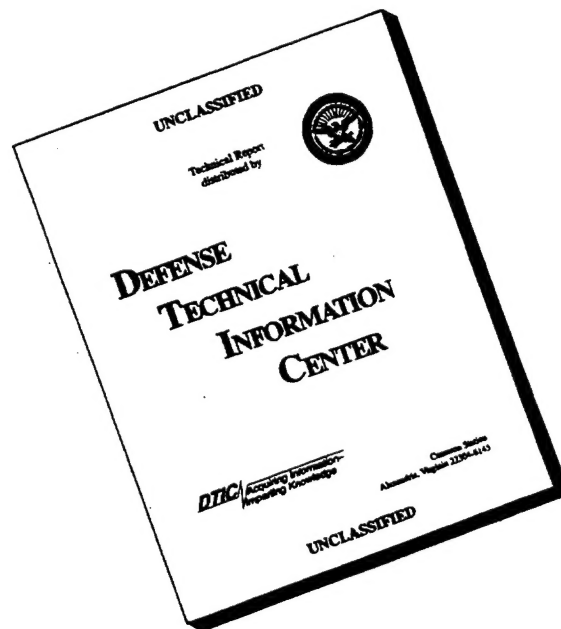| 17. SECURITY CLASSIFICATION OF REPORT	18. SECURITY CLASSIFICATION OF THIS PAGE	19. SECURITY CLASSIFICATION OF ABSTRACT	20. LIMITATION OF ABSTRACT

DISCLAIMER NOTICE

UNCLASSIFIED

Technical Report
distributed by

DEFENSE
TECHNICAL
INFORMATION
CENTER

DTIC Acquiring Information—
Imparting Knowledge

Cameron Station
Alexandria, Virginia 22304-6145

UNCLASSIFIED

THIS DOCUMENT IS BEST
QUALITY AVAILABLE. THE
COPY FURNISHED TO DTIC
CONTAINED A SIGNIFICANT
NUMBER OF PAGES WHICH DO
NOT REPRODUCE LEGIBLY.

SUDAAR 649

EXPERIMENTS IN HIGH-PERFORMANCE CONTROL
OF A MULTI-LINK FLEXIBLE MANIPULATOR
WITH A MINI-MANIPULATOR

William L. Ballhaus

Aerospace Robotics Laboratory
Department of Aeronautics and Astronautics
STANFORD UNIVERSITY
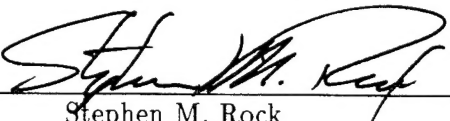*Stanford, California 94305*

April 1994

EXPERIMENTS IN HIGH-PERFORMANCE CONTROL
OF A MULTI-LINK FLEXIBLE MANIPULATOR
WITH A MINI-MANIPULATOR

A DISSERTATION

SUBMITTED TO THE DEPARTMENT OF AERONAUTICS AND ASTRONAUTICS

AND THE COMMITTEE ON GRADUATE STUDIES

OF STANFORD UNIVERSITY

IN PARTIAL FULFILLMENT OF THE REQUIREMENTS

FOR THE DEGREE OF

DOCTOR OF PHILOSOPHY

By

William L. Ballhaus

April 1994

I certify that I have read this dissertation and that in my opinion it is fully adequate, in scope and in quality, as a dissertation for the degree of Doctor of Philosophy.
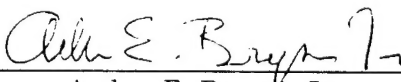
Stephen M. Rock
Department of Aeronautics and Astronautics
(Principal Adviser)

I certify that I have read this dissertation and that in my opinion it is fully adequate, in scope and in quality, as a dissertation for the degree of Doctor of Philosophy.

Robert H. Cannon, Jr.
Department of Aeronautics and Astronautics

I certify that I have read this dissertation and that in my opinion it is fully adequate, in scope and in quality, as a dissertation for the degree of Doctor of Philosophy.

Arthur E. Bryson, Jr.
Department of Aeronautics and Astronautics

Approved for the University Committee on Graduate Studies:

iii

$\sim$

Abstract

Space-based manipulator systems like the Shuttle Remote Manipulator System contain long slender links that are inherently very flexible. As a result, when moving quickly or carrying massive payloads, the links of these manipulators deflect significantly. This link flexibility slows and degrades end-point position performance and makes high-performance control of these manipulators difficult to achieve.

The research presented in this dissertation focuses on increasing the achievable slew and end-point performance of multi-link flexible manipulators through the use of a small, high-bandwidth, rigid robot (mini-manipulator) at the tip, together with direct end-point sensing. The high-bandwidth mini-manipulator can be used for rapid, precise control within a small workspace, while the main manipulator is responsible for transporting the mini-manipulator from workspace to workspace.

The overall system performance of a multi-link flexible manipulator with a mini-manipulator is limited, in part, by the ability of the flexible main arm to position quickly the mini-manipulator within the desired workspace. This is mitigated, however, by the fact that even for very high-performance control, the flexible main arm need be controlled only to an *area*, rather than to a point; an area within which the speed and precision of the mini-manipulator can then be utilized to perform the task at hand. This new generic concept of controlling to an area is pursued in this research through a new technique known as *soft terminal control*.

A new soft-terminal-control approach has been developed for multi-link flexible manipulators that exploits both the high-bandwidth local-manipulation capability and the redundancy introduced by the mini-manipulator, and the fact that the flexible main arm can be positioned more quickly to be within an area than it can be positioned to be at a point. This approach, based on a terminal-controller design, combines feedforward with feedback control. In developing this new control approach, fundamental advances were made in trajectory generation, feedback-control design, and modelling of multi-link flexible manipulators.

To aid in the development and verification of this control approach, an experimental test bed has been developed. This apparatus consists of a two-link very flexible manipulator with a mini-manipulator mounted at its tip. This system floats on an air bearing to simulate in two dimensions the zero-g, frictionless environment of space.

This dissertation contains a description of the theoretical and experimental advances made in trajectory generation, feedback-control design, and modelling of multi-link flexible manipulators. Also included are experimental results that demonstrate, for the first time, the performance advantages of a mini-manipulator and direct end-point sensing at the tip of a multi-link flexible manipulator, and of their system operation as a redundant team.

To my parents
for their love, guidance, and support.

$\sim$

Acknowledgements

I wish to thank my principal adviser, Professor Steve Rock, for his technical guidance, for his advice on various subjects, and for his friendship over the last four years. It was his ability to play the perfect devil's advocate that enabled me to complete this dissertation, in spite of myself. I am indebted to Professor Robert H. Cannon, Jr. for inviting me into the Stanford Aerospace Robotics Laboratory, for providing the ideal research environment, and for his lessons on hyphenation. His vision, his passion for research, and his energy have certainly been an inspiration to me. I would also like to thank Professor Art Bryson for his technical guidance over the years, and for his careful review of this dissertation.

Life in the Aerospace Robotics Laboratory has been a truly enjoyable experience, due entirely to the students (past and present), the staff, and the professors associated with the lab. I would like to thank Jane Lintott for being the best administrative assistant in the world. I wish to thank Gad Shelef and Godwin Zhang for their efforts and assistance in building and maintaining the experimental apparatus. I would like to thank my mentor in flexible structures, Celia Oakley, for her invaluable assistance when I first started my research. I owe special thanks to Larry Alder and Steve Ims for their friendship, for daily discussions of the sports page, and for setting me straight on technical issues on many occasions. A special thanks is also owed to Dave Meer for tolerating my antics on a daily basis, for his friendship, and for maintaining our real-time system. I thank Stan Schneider, Marc Ullman, Vince Chen, Denny Morse, and Gerardo Pardo-Castellote for building and maintaining the wonderful computer environment in the lab. In addition, for their technical assistance and friendship, I thank Rob Vasquez, Larry Pfeffer, Bill Dickson, Ed Wilson, Tim McLain, Kurt Zimmerman, Howard Wang, Rick Marks, Jeff Russakow, Homer Stevens, and Eric Miles – they are the tools that have made the ARL #1.

Finally, and most of all, I would like to thank my Mom and Dad, as well as Jane and Chuck, for the love, guidance, and support they have given to me over the years. It is to them that I dedicate this dissertation.

~

x

Contents

List of Figures

$\sim$

Chapter 1

Introduction

This dissertation presents theoretical and experimental research on the high-performance control of generic multi-link flexible space manipulator systems, and specifically of a two-link flexible manipulator with a mini-manipulator at its tip. This research was conducted at the Stanford University Aerospace Robotics Laboratory (ARL) at Stanford University from 1991 to 1994.

1.1 Motivation

1.1.1 Robotics

Robots are well suited for many tasks performed currently by humans. Examples include high-speed pick-and-place maneuvers, automated inspection, assembly, and manufacturing tasks. Robots are especially well suited to operate in harsh environments, such as space or hazardous-waste sites, that can be potentially harmful to humans.

Present day industrial robots are typically slow and massive. In general, they are controlled at a joint level, and *infer* end-point position from joint-angle measurements. This control approach, which involves sensing and actuating at the same physical location, is known as collocated control. Obviously if any link flexibility exists, the end-point position will not correspond to the joint-angle measurements, and performance will deteriorate. Consequently, to avoid errors due to link flexibility, industrial robots have been designed to be very massive and rigid.

1

1.1.2   Flexible-Link Manipulators

Unfortunately, because of the cost of boosting mass into orbit, very massive and rigid *space-based* manipulators are uneconomical and therefore impractical. In addition, space-based manipulators are designed to have long links in order to cover a large workspace. This combination of link characteristics – long and lightweight – results in manipulators that exhibit significant link flexibility. Thus, when manipulating large payloads or operating at high speeds, the links will undergo large deflections that will reduce performance unless their end point is controlled actively and directly.

The Shuttle Remote Manipulator System (SRMS) shown in Figure 1.1 is an example of a flexible-link space-based manipulator currently in operation.   Allowing astronauts
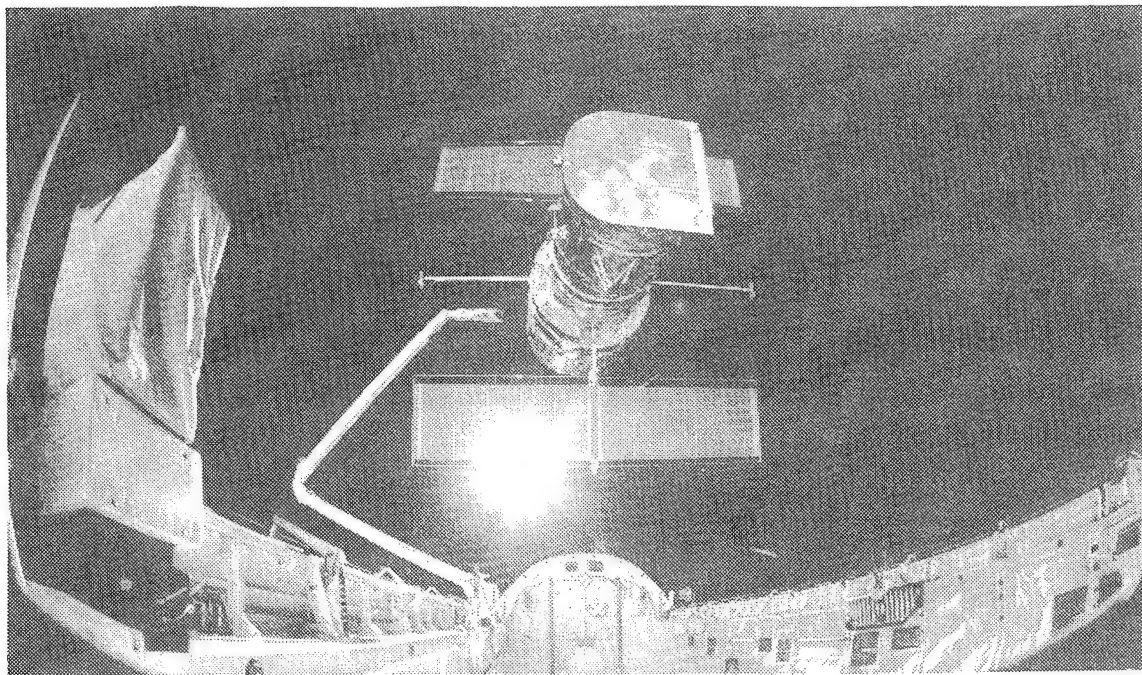
Figure 1.1: **Shuttle Remote Manipulator System**

The SRMS is a space-based manipulator system that is currently in operation. Future applications of this system will include refueling, repair, and inspection of spacecraft. The speed and accuracy of the SRMS is limited in part by the ability of its control system to control actively inherent link flexibility.

to remain within the safe and comfortable confines of the shuttle, the SRMS has been instrumental in performing numerous tasks within the shuttle bay. Figure 1.1 shows the SRMS having just deployed the Hubble Space Telescope.

The SRMS extends 15 meters, is made out of light-weight carbon-composite material, and has a mass of 450 kg. It contains significant link flexibility. Its lowest natural frequency, with locked joints, ranges from .04 to .4 Hz depending on the payload ([1] and [2]).

1.1.3 Control of Flexible-Link Manipulators

Currently, flexible-link manipulators like the SRMS are controlled at a joint level using a collocated control approach similar to most industrial robots. Because this joint-based approach is very limited in its ability to control the end point via the link flexibility, the SRMS must be moved very slowly. Typically, end-point speeds are kept below 0.06 m/sec for the fully loaded configuration and below 0.6 m/sec for the unloaded configuration [3].

Previous research has demonstrated that the performance of flexible manipulators like the SRMS can be increased through a control system that is improved in a very fundamental way: by measuring the end-point position directly, flexibility-induced errors can be reduced, and speed and precision of performance can be increased significantly ([4] and [5]).

Although end-point feedback does dramatically improve performance, there are still limitations, in terms of end-point control bandwidth and accuracy, associated with actuators separated from the manipulator end point by link flexibility. These limitations can be attributed to two factors.

- First, the accuracy with which the end point of the manipulator can be positioned is limited by the accuracy with which the joint actuators can be positioned. Fine end-point motion requires even more precise joint motion, and no change in link shape.

- Second, because the actuators are separated from the end point by a flexible link, there is a fundamental time delay associated with the actuation effort propagating down the flexible link. This delay invokes specific limits upon the end-point control bandwidth.

1.1.4 Mini-Manipulators

An intuitive way of finessing the accuracy and bandwidth limitations associated with flexible-link manipulators – and thereby increasing achievable performance – is to incorporate into the hardware design a *mini-manipulator*, or high-bandwidth, small, rigid robot, at the tip of the manipulator. The high-bandwidth mini-manipulator can be used for rapid, precise control within a small workspace, while the main manipulator is responsible for

transporting the mini-manipulator from workspace to workspace. The combination of a mini-manipulator and direct end-point sensing can therefore enable high-performance control at the tip of a multi-link manipulator despite significant link flexibility.

The concept of using a mini-manipulator and end-point sensing to increase achievable performance motivated this dissertation. Moreover, this research serves as a specific example of a more generic concept: the use of local actuation and sensing to achieve high-performance control at a specific location. This research also focused on system-level optimization to exploit the attributes of each subsystem – the long, limber main manipulator and the quick, precise mini-manipulator.

The ideas that prompted this dissertation are also the motivation behind designs envisioned for future space missions. For example, Figure 1.2 is an artist's rendition of the

Main Arm

Special Purpose
Dextrous Manipulator
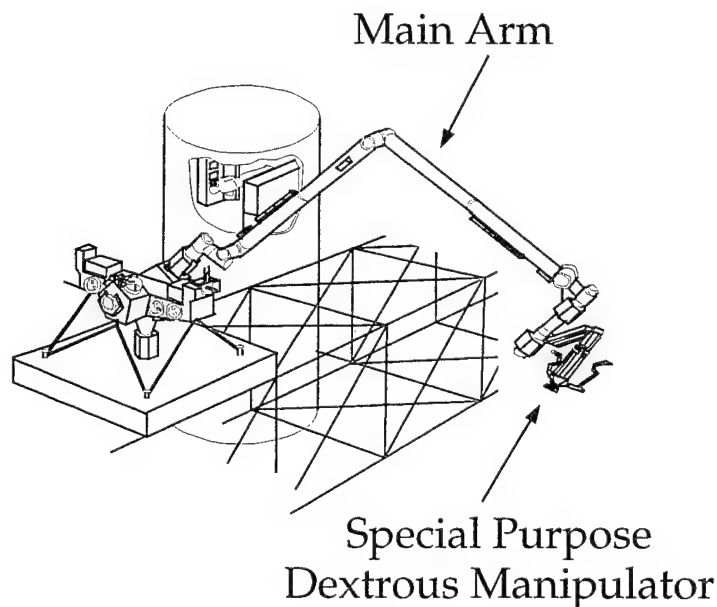
Figure 1.2: **Artist's Rendition of the Space Station Manipulator Servicer**

This servicer might be responsible for tasks such as maintenance, assembly, and transportation about the space station. To increase the speed and precision with which these tasks can be performed, a mini-manipulator has been incorporated into the hardware design of this system.

Space Station Manipulator Servicer (SSMS). This system contains a flexible main arm that

is similar to the SRMS. In addition, the SSMS includes the Special Purpose Dextrous Manipulator (SPDM), which is a small, rigid robot that is mounted at the tip of the main arm. The motivation behind the SPDM is to provide capability for local manipulation to increase achievable performance at the tip of the flexible main arm.

1.1.5 Control of a Flexible Manipulator with a Mini-Manipulator

The overall system performance of a multi-link flexible manipulator with a mini-manipulator will be limited, in part, by the ability of the flexible main arm to position quickly the mini-manipulator within the desired workspace. This is mitigated, however, by the fact that even for very high-performance control, the flexible main arm need be controlled only to an *area*, rather than to a point; an area within which the speed and precision of the mini-manipulator can then be utilized to perform the task at hand.

High-performance control, then, calls for an advanced control system that accounts for the inherently flexible links of the main arm, exploits the quick, precise, local-manipulation capabilities of the mini-manipulator, and exploits explicitly the inherently greater speed with which the end of the large flexible main arm can be positioned to within an *area* rather than it can be positioned to a *point*. This is a generic control-system concept that can enrich a variety of future automatic control systems that deliberately incorporate redundancy.

In developing this advanced control system, a number of very complex issues must be addressed:

- **Control Strategy:** Development of a specific system-control strategy is required to exploit the combination of high-bandwidth, local-manipulation benefits of the mini-manipulator with the peculiar benefits of large-slew control of the flexible main arm to a terminal area (rather than to a point).

- **Control Approach:** Formulation of the control strategy in the form of a specific control approach is needed.

- **Modelling:** Equipping a multi-link flexible manipulator with a mini-manipulator results in an extremely flexible, dynamically coupled, redundant system. Controlling this system requires first developing an accurate mathematical model to support fully control-system design, simulation, and analysis.

- **Sensor Selection:** Exploiting the benefits of the mini-manipulator, and achieving high-performance control of the main arm in the presence of link flexibility, requires end-point sensing of position and orientation.

- **Estimation:** Because it is not at all practical to measure all states of such a system, state estimation of the nonlinear multi-link main-arm/mini-manipulator system is required for those states that are not measured.

- **Multi-Link Systems:** Each of the above issues becomes considerably more complicated for manipulators with *many* flexible links. Tasks in which a manipulator must grasp an object in various configurations or tasks that require a manipulator to maneuver around a space structure are applications where a manipulator with many links would be required.

The goal of this research is to develop the basic theory and technology to enable high-performance end-point control of multi-link flexible manipulators with local end-point manipulation (systems which embody the issues just described).

1.2   Background

This section reviews some of the previous fundamental research in the control of flexible manipulators and of mini-manipulators. It is by no means intended as a complete literature review; subsequent chapters discuss relevant research in much greater detail. Note that none of this previous research has addressed how to incorporate the benefits of a mini-manipulator into a control approach for multi-link *flexible* manipulators. Hence, this dissertation addresses a totally new research area.

1.2.1   Flexible-Link Manipulators

Eric Schmitz performed at the Stanford Aerospace Robotics Laboratory (ARL) the first experimental research in the end-point control of flexible manipulators. Through experiments with a single-link flexible manipulator ([6] and [4]), he demonstrated that end-point position feedback enabled a factor of four improvement over the performance achievable with conventional joint-based collocated control.

Schmitz's work led to a sequence of experimental research achievements in the control of a single-link flexible manipulator. Maples [7] demonstrated end-point force control.

Rovner [8] showed that end-point control relied on an accurate system model. He developed an adaptive algorithm based on a self-tuning regulator approach which could successfully identify the tip payload mass in real time. Alder [9] developed an adaptive approach to identify and control dynamic payloads which had, themselves, a single, lightly-damped oscillatory mode.

Oakley ([10], [11], [12], [13], [14], and [5]) made a significant advancement at the ARL by extending Schmitz's findings to a two-link flexible manipulator. She demonstrated experimentally similar increases in performance using end-point feedback to control an extremely flexible two-link manipulator.

Since the work of Schmitz and Oakley, researchers at numerous universities and research centers have been studying various aspects of flexible-link manipulators. This work ranges from the computation of control inputs to follow a specified trajectory ([15], [16], [17], and [18]) to filtering command inputs to reduce residual vibrations ([19], [20], [21], [22], and [23]).

1.2.2 Mini-Manipulators

Other previous research at the ARL has incorporated the use of a mini-manipulator to increase the performance of a single-link flexible manipulator. The research of Chaing, Tilley, and Kraft ([24], [25], and [26]) demonstrated an order-of-magnitude improvement in position and force control over that achievable with the single-link flexible manipulator alone. Furthermore, Andersen [27] utilized a mini-manipulator to demonstrate precise force control at the end of a two-link manipulator with flexible drive trains.

1.3 Research Goals

There were two primary objectives of the research presented in this dissertation:

1. To develop a control approach that exploits in a system-optimal way the benefits of a mini-manipulator to achieve *high-performance end-point control* of multi-link, very-flexible manipulators.

2. To verify experimentally this approach on the two-link flexible manipulator with a mini-manipulator mounted at its tip as shown in Figure 1.3.
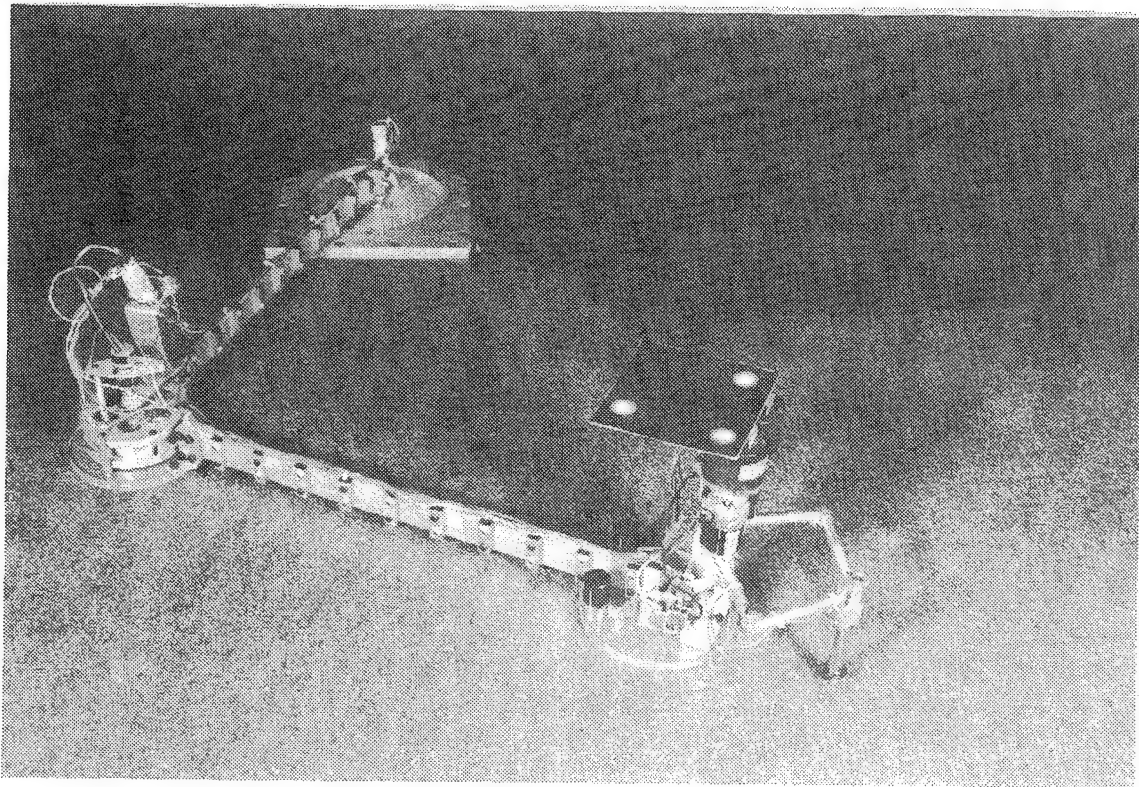
Figure 1.3: **Experimental Apparatus**

*The experimental apparatus used in this research consisted of an extremely flexible
two-link manipulator with a mini-manipulator, or small rigid robot, mounted at
its tip. This experimental system was used to verify and refine the theoretical
developments presented in this dissertation.*

The specific problem addressed in this research was to achieve high-performance point-to-point end-point control of the two-link main-arm/mini-manipulator system. A schematic of this task is shown in Figure 1.4. The point-to-point repositioning was chosen as an

Point-To-Point Repositioning

Initial Configuration
(t = 0)

Final Configuration
(t = t_f)
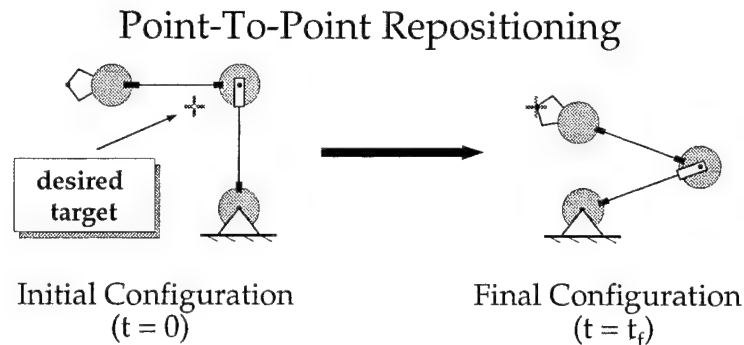
Figure 1.4: **Experimental Demonstration**

A point-to-point repositioning was chosen as an experimental demonstration of high-performance end-point control of the flexible main-arm/mini-manipulator system. With the system in an initial configuration, a desired target is specified along with a final time in which the target is to be acquired. Meeting successfully the point-to-point positioning requirements involves positioning the tip of the system over the target within the specified time, and then maintaining this tip position precisely, despite disturbances, until a new target is specified.

experimental task for two reasons. First, it is a generic task in that it is representative of many other tasks: pick-and-place maneuvers, repositioning of flexible space structures, transportation of payloads, and precision pointing of flexible spacecraft. Second, successful point-to-point repositioning requires both high-performance large-motion slews of the entire system as well as high-performance end-point control within a localized workspace.

1.4 General Approach

To exploit both the high-bandwidth local-manipulation capability and the redundancy introduced by the mini-manipulator, and the fact that the flexible main arm can be positioned much more quickly to be within an area than it can be positioned to be at a point, a new control strategy for controlling multi-link flexible manipulators has been developed. Because

the mini-manipulator provides quick, precise control only within a localized workspace, system performance for large-motion slews is limited by the speed at which the flexible main arm can transport the mini-manipulator to the area where it is to work. As a result, meeting the goals of this research resulted in a two-part control strategy:

- To control the main arm quickly to a *target area*, rather than to a precise location. This new concept of controlling to a target area is pursued in this research through a new technique known as *soft terminal control.*

- To control the mini-manipulator tip precisely to the desired target position (a *point* in space).

Soft terminal control of multi-link flexible manipulators is made possible by the speed and redundancy introduced by the mini-manipulator. Because of this redundancy, the target can be acquired with the system in more than one configuration. Figure 1.5 illustrates this concept.   Rather than controlling the flexible main arm to a specific point, successfully
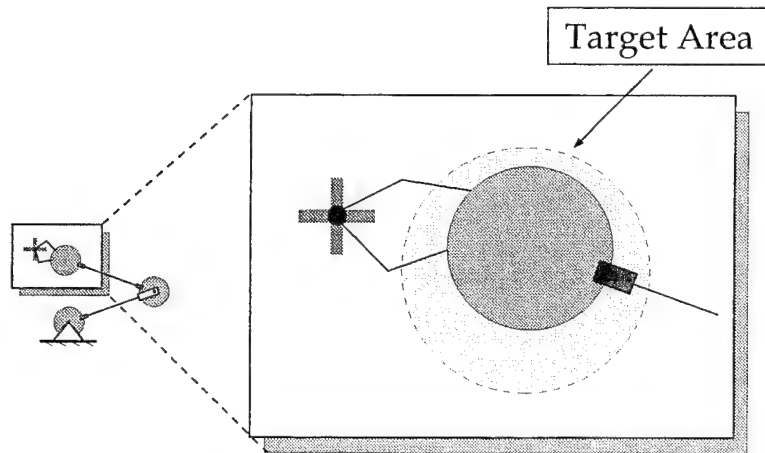
Figure 1.5: **New Performance Objective**

Because of the redundancy and high-bandwidth-manipulation capability introduced by the mini-manipulator, meeting successfully the requirements of a point-to-point repositioning depends first upon controlling quickly the main arm to a target area. The target area is defined as the region from which the mini-manipulator can acquire the desired target.   The control philosophy used for controlling to a target area, rather than to a specific point, is a fundamentally new approach to controlling multi-link flexible manipulators. It is known as soft terminal control.

meeting the repositioning requirements necessitates controlling the main arm near the target, to a target area. Then, once near the target, by taking advantage of the speed and redundancy introduced by the mini-manipulator, the mini-manipulator can acquire and maintain the desired tip position very quickly and precisely.

To position quickly the flexible main arm to the required area near the desired target, a new soft-terminal-control approach for multi-link flexible manipulators was developed. A block diagram of the solution framework in which the approach was implemented is shown in Figure 1.6. This framework merges a new trajectory-generation approach and a novel feedback-control approach to achieve high-performance control. Although the structure of this framework is not new, the novelty stems from the feedforward-trajectory generation and the feedback-control approaches developed in this research.

This control-system framework is based upon two components: the feedforward-trajectory generator and the feedback controller. The trajectory generator takes as input the reference commands, and produces the desired plant-state history and the necessary feedforward-control input to the actuators to effect this desired motion. The feedback controller incorporates measurements of plant outputs to produce a feedback-control input to the actuators. This feedback control combines with the feedforward control to regulate the plant to the desired plant state in the presence of modelling errors and disturbances.

In addition to the trajectory-generation and feedback-control approaches, a new modular modelling technique has been developed in conjunction with Steve Ims and Larry Alder [28]. This technique has enabled a modular approach to modelling multi-link flexible manipulators. The primary advantage of this approach is that it enables the modelling of multi-link flexible manipulators to be partitioned into modelling smaller subsystems, and then integrating the subsystem models to obtain a total-system model.

The next subsections give brief descriptions of new approaches developed in this dissertation to each of the three steps in the design process: feedforward-trajectory generation, feedback-control design, and modelling. Chapters 4, 5, and 3 each present a detailed description of the new approaches to one of these steps.

1.4.1 Feedforward Trajectory Generation

Trajectory generation is paramount to achieving high-performance point-to-point repositioning. In generating and effecting a complete trajectory for a point-to-point repositioning, there are two components that need to be computed. The first is the desired state history, or
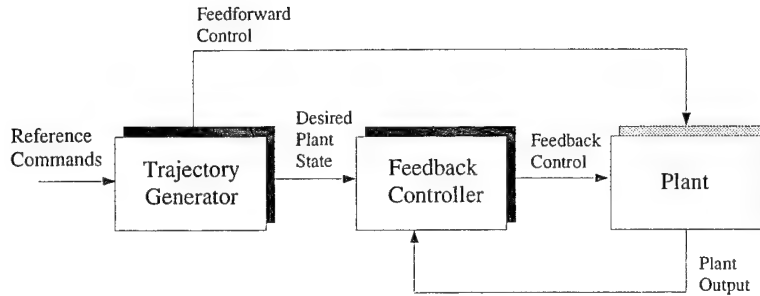
Figure 1.6: **Control Framework**

The control framework developed in this dissertation merges a new feedforward trajectory-generation scheme with feedback control to achieve high-performance soft-terminal-control of multi-link flexible manipulators. The trajectory generator computes the necessary feedforward-control input so that the plant follows the reference commands with the corresponding desired plant-state history. The feedback controller uses measurements from the plant to produce a feedback-control component. This feedback control augments the feedforward control to assure that the plant follows the desired plant state in the presence of modelling errors and disturbances.

the desired plant motion for the repositioning. The second component is the corresponding feedforward-control input to the actuators that, in the presence of an exact model, causes the desired motion.

There are three issues that make trajectory generation for multi-link flexible manipulators a challenging task. First, for real-time implementation, the trajectory generation must be numerically efficient to mitigate the computation-invoked lag time at the beginning of the trajectory. Second, finding the actuator-command history that corresponds to a desired trajectory requires, in general, inverting a high-order plant [1] for every trajectory to be followed. Because flexible manipulators are non-minimum-phase systems, plant inversion is a computationally intensive task. Finally, because high-frequency inputs can excite lightly-damped or unmodelled flexible modes, the frequency content of the prescribed trajectory should be shaped carefully.

The trajectory-generation approach developed in this dissertation is based on a model-following control framework in which a plant model is driven by the *time-varying gains* of a terminal controller. The trajectory generator produces, in real time, the optimal trajectory

---

[1] The plant's flexible-beam components result in an infinite number of natural modes of vibration.

for a finite-time point-to-point repositioning. Included in the computed trajectory are both the optimal state history and the corresponding feedforward-control inputs to the actuators.

Benefits

The primary benefit of this approach is that it provides, in real time, an optimal trajectory for the flexible main arm to follow during a point-to-point repositioning of the main-arm/mini-manipulator system. In addition to performance benefits, there are several other characteristics of this trajectory-generation approach that make it valuable in controlling multi-link flexible manipulators with local-manipulation capability.

- First, this approach exploits the speed and redundancy introduced by the mini-manipulator which makes it necessary only to quickly bring the main arm *near* the desired target. To do this, the strategy of soft terminal control is incorporated into the trajectory generation in the form of *soft terminal constraints* in the terminal-controller design.

- Second, the generated trajectory consists of both a desired state history and the corresponding feedforward control to the actuators, both of which are computed in *real time*.

- Third, the only slew-dependent precomputations of this approach are based on the specified slew time. As a result, for repositionings of the same slew time, no additional precomputations are required.

- Fourth, included in this approach is a method for shaping the frequency content of the trajectory not to excite lightly-damped or unmodelled flexible modes.

This optimal-trajectory-generation approach is discussed in detail in Chapter 4.

1.4.2 Feedback Control

In any real system, feedback control is, of course, always essential to ensure that the system – in this case a multi-link flexible manipulator – follows the commanded state history. The strength of the feedback needed will be affected by the magnitude of the process uncertainties and modelling errors present, among other things. Although methods exist for designing high-performance controllers, the goal of the approach used here is to enable

a partitioned design process, while at the same time retaining as much performance as possible.

The control approach developed in this dissertation enables the development of high-performance controllers for *predominantly* one-way coupled systems to be partitioned into sequential subsystem designs. This sequential process exploits the one-way coupling that characterizes the system within the frequency range of interest for control. Because the one-way coupling assumption is inaccurate outside of this frequency range, the subsystem controllers are designed to be robust to this model uncertainty. As a result, this approach enables the *high-performance-control* design for complex systems to be partitioned into smaller, more tractable subsets.

Benefits

There are two advantages to this sequential design approach.

- First, because of its sequential nature, this approach enables the development of a total-system controller to be separated into smaller and more tractable control-design problems. This is particularly advantageous in control design for flexible manipulators with *many* links.

- Second, for predominantly one-way-coupled systems, the robust subsystem controllers enable high-performance in the presence of modelling uncertainty outside the frequency range of interest for control.

This feedback-control approach is discussed in detail in Chapter 5.

1.4.3   Modelling

The trajectory-generation and feedback-control approaches developed in this dissertation require an accurate system model for design, simulation, and analysis. The modular modelling approach developed in this research enables the development of a total-system model to be partitioned into the modelling of smaller, less complex subsystems. After accurate modelling of each subsystem, a total-system model is obtained through a *concatenation*, or integration, of subsystem state-space models by enforcing the physical constraints that couple the subsystems. [2] This integration of accurate subsystem state-space models yields

---

[2]This approach enables the concept of model concatenation, also utilized in the research of Koningstein [29], Chen [30], and Alder [9], to be applied to *state-space* subsystem models. Consequently, this

an accurate total-system state-space model from which high-performance controllers can be designed.

Benefits

This modular modelling approach has four characteristics that make it particularly well suited to modelling *multi-link* flexible manipulators.

- First, because of the modularity of this approach, it is amenable to modelling complex systems in which the subsystems can be constrained physically in a variety of configurations.

- Second, it allows for fast rederivation of total-system models in the presence of subsystem modifications, additions, and substitutions.

- Third, the method allows the subsystem models to be in state-space form without restrictions on the elements of the state vector. Thus, the most convenient set of coordinates can be used to model the subsystems.

- Fourth, this approach yields a linear-time-invariant (LTI) system model of the form

$$\dot{\mathbf{x}}(t) = \mathbf{A}\mathbf{x}(t) + \mathbf{B}\mathbf{u}(t)$$
$$\mathbf{y}(t) = \mathbf{C}\mathbf{x}(t)$$

where $\mathbf{x}(t)$ is a vector of state elements, $\mathbf{u}(t)$ is a vector of control inputs, $\mathbf{y}(t)$ is a vector of outputs, $\mathbf{A}$ and $\mathbf{B}$ are the state transition and input matrices, and $\mathbf{C}$ is the output matrix. This is the model form required by much of the existing optimal-control theory for LTI systems.

1.5 Contributions

In meeting the goals of this dissertation, the research reported in this thesis makes the following contributions to the fields of automatic control and robotics:

---

approach enables Oakley's novel System Modes Representation modelling approach [5], from which accurate state-space models of flexible systems can be derived, to be utilized in the subsystem modelling process of a concatenation-based modelling approach.

- A generic new approach to achieving high-performance control of multi-link very-flexible manipulators has been developed. This approach incorporates local-manipulation capability, in the form of a mini-manipulator, and direct end-point sensing to remove totally the severe performance limitations imposed by the combination of link flexibility and actuation at a distance from the point to be controlled.

- A new control strategy, *soft terminal control*, has been developed to exploit the speed and redundancy of the mini-manipulator. The specific objective of this strategy is to control quickly the flexible main arm to a *target area*, rather than to a specific point, from which the mini-manipulator can acquire the desired target. The performance benefits of this strategy stem from the dramatic decrease in time required to control a multi-link flexible manipulator to an area rather than to a specific point.

- A fundamentally new optimal-trajectory-generation approach for multi-link flexible manipulators has been developed. This approach, based on a model-following implementation of a terminal controller, incorporates the novel soft-terminal-control concept of controlling the end-point of the main arm to a *target area* by establishing soft terminal constraints for the main manipulator in the terminal-controller design.

  The optimal-trajectory generation requires minimizing a finite-time, linear-quadratic performance index with soft terminal constraints, resulting in time-varying gains. The generated trajectory consists of the optimal state history as well as the corresponding optimal control-command history. This new approach generates trajectories that correspond to "near-minimum-time" repositionings. Furthermore, all of the significant non-slew-specific computations can be performed ahead of time, since these computations are independent of initial and final configurations. As a result, this approach offers benefits in terms of implementation and design.

- A method has been developed to shape the frequency content of the generated trajectories not to excite lightly-damped unmodelled flexible modes. This method involves frequency weighting the finite-time, linear-quadratic cost function. As a result, this approach is directly applicable to manipulators exhibiting link and/or drive-train flexibility.

- A method for achieving an essentially bumpless control-mode transfer at the end of large-motion slews has been developed. This method involves time weighting the cost

function in conjunction with implementing the terminal controller in a model-following control framework.

- This optimal-trajectory-generation approach was tested successfully and verified on a physical two-link, extremely flexible manipulator. These experiments demonstrated for the first time the use of a terminal-controller-based approach to reposition rapidly a lightly-damped multi-input-multi-output flexible manipulator.

- A feedback-control approach has been developed for a class of multi-link flexible manipulators containing subsystems that are predominantly one-way coupled. By exploiting this limited-coupling characteristic, this control approach enables a sequential design process. The subsystem controllers are made robust to model uncertainty outside the frequency range of interest through a frequency-shaped control design. Because system-level coupling information is fully utilized in this process, and not overlooked, high performance is achieved; yet, through a sequential control-design process.

- A generic modelling approach has been developed, based on the model concatenation technique presented in [28], that facilitates the modelling of a wide class of multi-link flexible structures. This method enables the development of a total-system model through a concatenation of subsystem models. This approach is inherently modular, and is extensible to any number of links and degrees of freedom. This method was used to develop an accurate *total-system* model of the two-link-flexible-manipulator/mini-manipulator system.

- This research culminated with the first-ever demonstration of end-point control of a mini-manipulator mounted at the tip of an extremely flexible multi-link manipulator. High-performance end-point position control was demonstrated for large slews of the total system and for disturbance rejection at the tip of the mini-manipulator/two-link-flexible-manipulator system. For the system repositionings presented in this dissertation, the mini-manipulator enabled nearly a factor of two decrease in repositioning times. Also, the mini-manipulator reduced tip errors due to tip disturbances by a factor of 25.

- Each of the above contributions represents valuable progress toward the general problem of controlling a system made up of many (n) very flexible substructures for which

a distributed set of many actuators can be used. For the experiments presented in this dissertation, $n = 3$, which connotes considerable generality.

1.6   Reader's Guide

This chapter has served as an introduction to the research that is presented in this dissertation. The remainder of this thesis is organized as follows:

Chapter 2 gives a description of the experimental apparatus. Included in this chapter is a detailed description of the two-link flexible manipulator and of the mini-manipulator mounted at its tip, as well as a description of the real-time computer hardware and software environment.

In Chapter 3, the generic modular modelling approach is described. This chapter also contains a specific application of this approach to modelling the two-link flexible manipulator with the mini-manipulator mounted at its tip.

Chapter 4 describes the new optimal-trajectory-generation approach. To illustrate the trajectory-generation-design process, optimal trajectories are generated and presented for the flexible main arm.

Chapter 5 contains a description of the sequential control approach for predominantly one-way-coupled systems. Also included in this chapter is an application of this control approach to the experimental apparatus.

Chapter 6 integrates the optimal-trajectory generator of Chapter 4 and the feedback controller of Chapter 5 to demonstrate high-performance point-to-point repositionings of the experimental mini-manipulator/main-arm system. The necessary contributions of feedback and feedforward control in meeting successfully the system repositioning requirements are illustrated. Also presented in this chapter is a description of the graphical user interface to the experimental apparatus.

Chapter 7 concludes this dissertation with a summary of results and recommendations for future research.

Appendix A presents the State-Space Model Concatenation Method upon which the modular modelling approach is based.

Appendix B provides important kinematic relations for the mini-manipulator.

Appendix C details the process of modelling the flexible links of the main arm.

Appendix D gives details of the terminal-controller solution, an example illustrating the performance advantages of time-varying gains, and the software used to generate the optimal trajectories.

Appendix E presents the estimator design for the flexible main arm.

Appendix F provides the specific model and controller matrices that were used in this research.

$\sim$

20

Chapter 2

Experimental System

This chapter gives a description of the experimental apparatus used to verify and refine the theoretical developments of this dissertation. Included in this chapter is a description of the hardware, the real-time-computer hardware and software environment, and the analysis software tools that were used in this research.

2.1 Design Philosophy

This section gives a brief description of the philosophy that governed the system design of the two-link flexible manipulator with the mini-manipulator shown in Figure 2.1.

2.1.1 Flexible Manipulator

The experimental manipulator was constructed to serve as a test-bed for evaluating and refining new theoretical developments for the control of flexible manipulators. The overall design strategy was to keep the design simple, yet to exaggerate link flexibility for research purposes.

The flexible main arm was designed so that damping must be provided through active control. The dimensions of each of the elastic links were chosen specifically to exaggerate their structural flexibility so that the flexibility could not be ignored. Along with exaggerating the link flexibility, the mechanical structure was designed to be lightly damped.

To isolate the effects of bending-induced flexibility, significant structural bending is limited to one plane. The two-link flexible manipulator operates in the horizontal plane. Torsional stiffness is provided for both links by the air-cushion supports at the manipulator
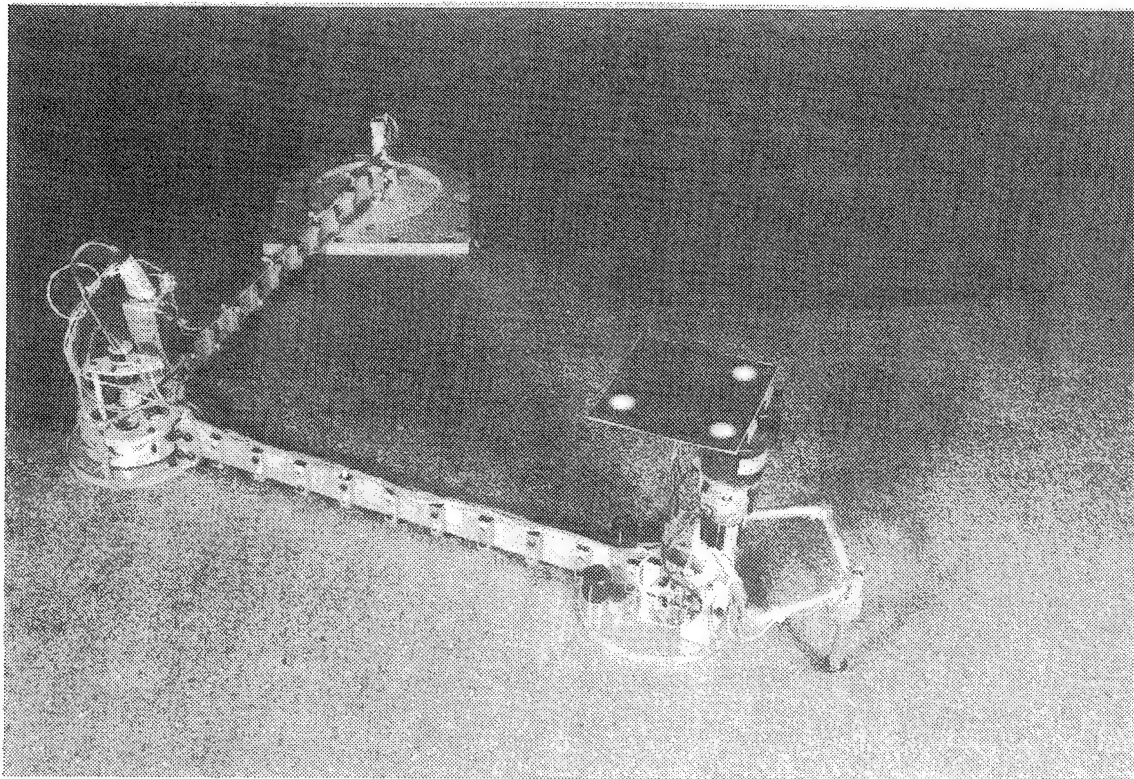
Figure 2.1: **Experimental Apparatus**

This is a photograph of the experimental manipulator system used to evaluate and refine the new theoretical developments of this research.

elbow and end point. The link cross sections were chosen to be relatively stiff in the vertical plane.

Motors located at the shoulder and elbow joints provide actuation to the manipulator. To keep the vibration frequencies of the second link low without adding unnecessary mass to the elbow joint, the elbow motor is part of the second link's hub rather than the first link's tip. Currently, sensors measure the shoulder and elbow joint angles and rates and the manipulator end-point position and orientation.

2.1.2 Mini-Manipulator

The design of the mini-manipulator was governed by the need for fast, precise end-point manipulation. The design, while kinematically and dynamically complex, is very elegant mechanically. Rather than having the actuators and sensors mounted on the links where they would slow down the end-point response, they are located at the base of the mini-manipulator. The links can therefore be made much lighter for quicker tip response.

2.2 Hardware Description

This section describes the two-link flexible manipulator and the mini-manipulator. A schematic of the experimental apparatus is shown in Figure 2.2.

2.2.1 Flexible Manipulator

The flexible main arm is a two-link flexible manipulator that operates on air cushions in the horizontal plane of a 1.2 m by 2.4 m granite table. Each of the flexible links is 0.52 m in length, and consists of an aluminum beam (cross section 1 mm by 38.1 mm) with discrete masses evenly spaced along its length. The discrete masses, or *mass intensifiers*, increase the overall beam mass without changing its flexural rigidity, and lower the natural frequencies of vibration.

The shoulder motor, mounted on the side of the granite table, can provide a peak torque of 5.43 N-m. The elbow motor, mounted on the elbow air-cushion pad, can provide a peak torque of 1.06 N-m. The motors are direct-drive, DC limited-angle torquers. Rotary-variable-differential-transformers (RVDT's) are located at each of the motor shafts and provide joint-angle measurements. A vision sensor, fully described in [31], provides end-point measurements. It consists of a CCD television camera that tracks a special variable
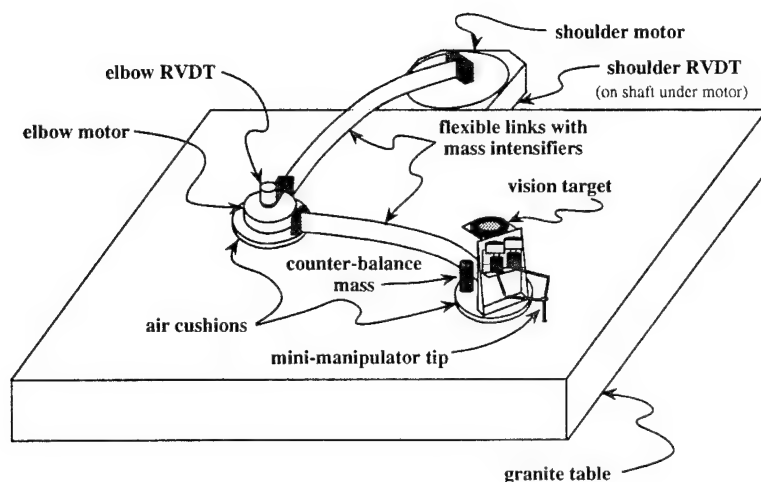
Figure 2.2: **Experimental Hardware Schematic**

Shown in this figure is a schematic of the two-link flexible manipulator with a mini-manipulator mounted at its tip.

reflectivity target located at the manipulator end point. The vision system has the capability to track multiple targets at a sample rate of 60 Hz with a resolution of approximately 1 mm over the roughly 1.5 m^2 workspace [5]. A detailed description of the flexible manipulator's parameters is given in Oakley's dissertation [5].

2.2.2   Mini-Manipulator

A two degree of freedom mini-manipulator is mounted at the tip of the two-link flexible main arm. The mini-manipulator, shown in Figure 2.3, consists of a five-link, closed-kinematic chain which operates in the horizontal plane. The base, inner, and outer links of the mini-manipulator are approximately 5.1 cm, 7.6 cm, and 10.2 cm in length respectively. To allow for quick, precise motion of the tip, the four moving links are made of hollow tubes, and are actuated by two small DC electric motors located at the base of the mini-manipulator. The motors have a peak torque of 0.35 N-m. Rotary encoders mounted on top of the motors provide angular-position and velocity information.
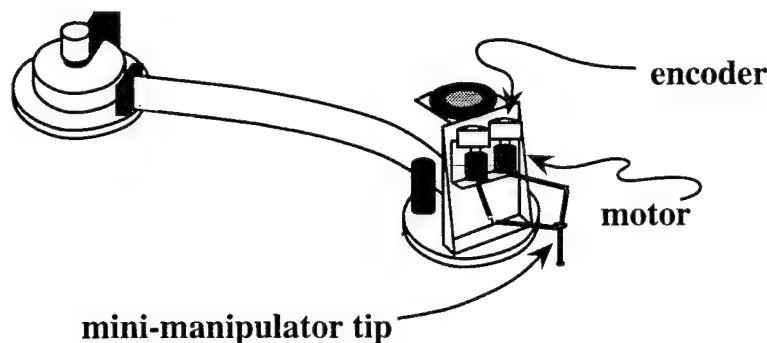
Figure 2.3: **Magnified View of the Mini-Manipulator**

This figure illustrates the mini-manipulator and its various components.

2.3 Computer System

The ARL has a user-friendly, state-of-the-art, heterogeneous computing environment. The computer system consists of Sun engineering graphics workstations interconnected by Ethernet, with a central file server. The real-time computing systems are also connected on the Ethernet. This arrangement has many advantages. For example, any real-time system can be accessed from any workstation, and the real-time systems can access files on the file server.

2.3.1 Real-Time Software

The controllers discussed in this dissertation were implemented on a digital computer. The real-time operating system was VxWorks [32]. In conjunction with VxWorks, *Control-Shell* [33] was used for real-time-software development. *ControlShell* enables a modular design and implementation of real-time software which allows a unique component-based approach to real-time-software generation and management.

2.3.2 Analysis Software

MATLAB [34], a matrix manipulation package, was used for a wide variety of analysis tasks. For example, it was used to calculate and discretize system matrices of linearized plants, to find eigenvalues and eigenvectors, to design controller gains, to check algorithms, to plot data, and to perform simulations. In addition, *StethoScope* [35], was used to collect

and monitor time traces of variables on the real-time system. The data collected using *StethoScope* was stored in MATLAB format for subsequent viewing and analysis.

2.3.3   Real-Time Hardware

The real-time hardware consisted of two Motorola MVME-167 real-time processors, a Motorola MVME-147 real-time processor, a Burr-Brown MPV954 digital-to-analog converter card, a Burr-Brown MPV950 analog-to-digital converter card, a DataCube MaxScan video frame grabber, and a DataCube RoiStore video frame memory. This real-time system hardware configuration was chosen for its easy expandability and for its compatibility with the Sun processors and VME bus.

Chapter 3

Modelling

This chapter presents a modular approach to modelling multi-link flexible manipulators. This approach is based on a new model concatenation technique, the State-Space Model Concatenation Method, that was developed in [28]. Included in this chapter is a specific application of this approach to modelling the experimental two-link flexible manipulator with a mini-manipulator at its tip.

Chapters 4 and 5 require a system model for trajectory generation and feedback-control design. Specifically, a linear-time-invariant (LTI) model is needed of the form

$$\dot{\mathbf{x}}(t) = \mathbf{A}\mathbf{x}(t) + \mathbf{B}\mathbf{u}(t)$$
$$\mathbf{y}(t) = \mathbf{C}\mathbf{x}(t)$$

where $\mathbf{x}(t)$ is a vector of state elements, $\mathbf{u}(t)$ is a vector of control inputs, $\mathbf{y}(t)$ is a vector of outputs, $\mathbf{A}$ and $\mathbf{B}$ are the state transition and input matrices, and $\mathbf{C}$ is the output matrix. The approach described in this chapter is one possible technique that can be used to develop such a model.

The modularity of the modelling approach presented here has two distinct benefits:

- First, modularity allows modelling complex systems to be partitioned into modelling smaller subsystems.

- Second, a modular approach enables fast model rederivation in the presence of subsystem modifications, additions, or subtractions, without rederiving models for the unaffected subsystems.

27

The modelling approach described in this chapter enables modelling of multi-link flexible manipulators to be partitioned into modelling smaller, less complex subsystems. After accurate modelling of each subsystem, a total-system model is obtained through a *concatenation*, or integration, of subsystem state-space models by enforcing the physical constraints that couple the subsystems. This integration of accurate subsystem state-space models yields an accurate total-system state-space model from which high-performance controllers can be designed.

Benefits   Because of its modularity, this modelling approach offers the two benefits listed above. In addition, this approach has two characteristics that make it particularly well suited to modelling *multi-link* flexible manipulators for the purposes of control design, simulation, and analysis.

- First, because of its modularity, this approach is amenable to modelling complex systems in which the subsystems can be physically constrained in a variety of configurations.

- Second, this approach allows the subsystem models to be in state-space form where the state vector is arbitrary, thus allowing the most convenient set of coordinates to be used in subsystem modelling.

3.1   Background

The idea of model concatenation is common to many well known modelling approaches. For instance, transmission line theory is a modelling technique where subsystem models, in the form of transfer function matrices, are concatenated through matrix multiplication to determine an input-output mapping from one point in the system to another [36].

In addition, the finite-element method is based on model concatenation. The finite-element modelling technique treats a system as an assemblage of elements. By imposing constraints that the elements are represented by consistent generalized coordinates, and that the displacements be equal and the forces in balance at the element interfaces, the system equations of motion can be derived by concatenating the individual elements' equations of motion [37].

Other model-concatenation-based techniques have recently been developed. References [29], [30], [38], [39], and [40] give examples of concatenation-based modelling techniques.

Reference [9] presents a method for concatenating linear-time-invariant models when the subsystem models share generalized coordinates at the shared interface. This is an extension of the finite element philosophy in that only the shared generalized coordinates must be common to both subsystem models. In addition, this method differs from transmission line theory in that it allows for model concatenation of models expressed as second-order differential equations rather than matrices of transfer functions.

The State-Space Model Concatenation Method

The modelling approach developed in this thesis is based on the State-Space Model Concatenation Method (SSMCM) [28] that generalizes the technique described in [9] to allow the concatenation of state-space subsystem models without placing restrictions on the elements of the subsystem state vectors. Furthermore, working directly in state-space form, this method enables a specification of the state vector of the resulting total-system model [28].

Problem Statement The state-space model concatenation problem involves finding a total-system model from models of two subsystems that are coupled through a *subsystem interface*. The coupling is characterized in terms of power transfer between the subsystems through the subsystem interface, using the power-conjugate signal pairs *effort* and *flow* [41]. For example, the power-conjugate signal pairs in a mechanical system can be force (effort) and velocity (flow); in an electrical system, voltage (effort) and current (flow).

A complete model of each subsystem consists of a state-space realization describing the relation from the external inputs $\mathbf{u}_i(t)$ and effort applied to the subsystem at the subsystem interface $\mathbf{e}_i$, to the monitored outputs $\mathbf{z}_i$, the flow of the subsystem measured at the subsystem interface $\mathbf{f}_i$, and the displacement, or integral of the flow, at the subsystem interface $\mathbf{d}_i$.[1] The objective is to determine a state-space realization relating the external inputs to the monitored outputs.

The general form of the state-space realization of each subsystem is given by

$$
\begin{aligned}
\dot{\mathbf{x}}_i &= \mathbf{A}_i\mathbf{x}_i + \mathbf{B}_i^u\mathbf{u}_i(t) + \mathbf{B}_i^e\mathbf{e}_i \\
\mathbf{z}_i &= \mathbf{C}_i^z\mathbf{x}_i \\
\mathbf{f}_i &= \mathbf{C}_i^f\mathbf{x}_i
\end{aligned}
\tag{3.1}
$$

---

[1] The SSMCM does not require the displacement at the interface $\mathbf{d}_i$ to be included. However, given the displacement as well as the flow, the SSMCM will perform a structured model reduction to remove the redundant coordinates from the total-system state vector [28].

$$\mathbf{d}_i \;=\; \mathbf{C}_i^d \mathbf{x}_i$$

where the dimensions for subsystem i, $i = 1,2$, are specified as the state vector $\mathbf{x}_i \in \mathbb{R}^{ns_i}$, external input vector $\mathbf{u}(t)_i \in \mathbb{R}^{nu_i}$, internal effort vector at the interface $\mathbf{e}_i \in \mathbb{R}^{ne_i}$, monitored output vector $\mathbf{z}_i \in \mathbb{R}^{nz_i}$, internal flow vector at the interface $\mathbf{f}_i \in \mathbb{R}^{nf_i}$, and internal displacement vector at the interface $\mathbf{d}_i \in \mathbb{R}^{nd_i}$, with $\mathbf{A}_i$, $\mathbf{B}_i^u$, $\mathbf{B}_i^e$, $\mathbf{C}_i^z$, $\mathbf{C}_i^f$, and $\mathbf{C}_i^d$ having consistent dimensions. These realization matrices may be time dependent. Note that consistency of power flow between the subsystems requires that the effort and flow vectors all be of the same dimension.

Finally, it is assumed that the effort at the subsystem interface satisfies an action-reaction-type relation. For mechanical systems, this would correspond to a rigid connection; in the electrical case, a short-circuit connection. The corresponding constraints are given by

$$\mathbf{e}_1 \;=\; -\mathbf{e}_2 \tag{3.2}$$

$$\mathbf{f}_1 \;=\; \mathbf{f}_2 \tag{3.3}$$

$$\mathbf{d}_1 \;=\; \mathbf{d}_2. \tag{3.4}$$

Solution Form   The output of the SSMCM is a coupled realization of the form

$$\dot{\mathbf{x}} \;=\; \mathbf{A}\mathbf{x} + \mathbf{B}\mathbf{u} \tag{3.5}$$

$$\mathbf{y} \;=\; \mathbf{C}\mathbf{x} \tag{3.6}$$

where $\mathbf{x} \in \mathbb{R}^{ns_1 + ns_2 - (nf_i + nd_i)}$ is the total-system state vector, $\mathbf{A}$ and $\mathbf{B}$ are the total-system transition and input matrices, $\mathbf{C}$ is the total-system output matrix, and the system inputs $\mathbf{u}$ and outputs $\mathbf{y}$ are defined as

$$\mathbf{u} \;=\; \begin{bmatrix} \mathbf{u}_1 \\ \mathbf{u}_2 \end{bmatrix} \tag{3.7}$$

$$\mathbf{y} \;=\; \begin{bmatrix} \mathbf{z}_1 \\ \mathbf{z}_2 \end{bmatrix}. \tag{3.8}$$

A detailed description of the solution process and the resulting solution form is given in Appendix A.

3.2 Modelling Approach

The underlying philosophy of this modelling approach is that the development of a total-system model can be simplified by first partitioning the complex system into a number of smaller subsystems, and then modelling the individual subsystems. The subsystem models can then be assembled to obtain a model of the original physical system.

The first step of this approach, therefore, involves partitioning a system into subsystems that are coupled through constraint forces at the subsystem interfaces. For example, for a planar, three-link manipulator, the partitioning can be performed as shown in Figure 3.1. The three-link manipulator with torque inputs can be represented as three subsystems that contain as inputs control torques and the constraint forces that couple the subsystems.
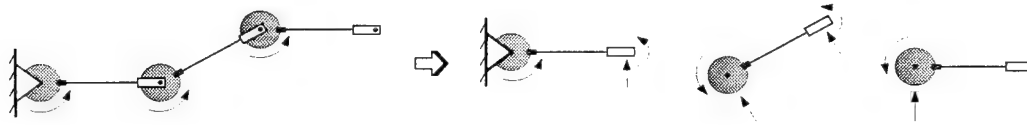
Figure 3.1: **System Partitioning**

This modular approach enables the modelling of a multi-link flexible manipulator to be partitioned into modelling subsystems, and then concatenating subsystem models to obtain a total-system model. This figure illustrates how a three-link manipulator with torque inputs can be represented as three subsystems that contain as inputs control torques and the constraint forces that couple the subsystems. The control torques are represented by curved arrows, while the straight arrows represent the constraint forces.

The second step of this approach requires developing state-space subsystem models of the form

$$
\begin{aligned}
\dot{\mathbf{x}}_i &= \mathbf{A}_i \mathbf{x}_i + \mathbf{B}_i^u \mathbf{u}_i(t) + \mathbf{B}_i^e \mathbf{e}_i \\
\mathbf{z}_i &= \mathbf{C}_i^z \mathbf{x}_i \\
\mathbf{f}_i &= \mathbf{C}_i^f \mathbf{x}_i \\
\mathbf{d}_i &= \mathbf{C}_i^d \mathbf{x}_i.
\end{aligned}
\tag{3.9}
$$

Note that the elements of $\mathbf{x}_i$ can be arbitrary allowing the most convenient set of coordinates to be utilized in the subsystem modelling process.

The third and final step of this approach involves assembling the individual subsystem models of Equation (3.9) to generate an LTI total-system state-space model. The State-Space Model Concatenation Method performs this assembly. For the system in Figure 3.1, the SSMCM takes as input two adjacent subsystem models and outputs a coupled realization of the two subsystems. The SSMCM can be applied again to concatenate this coupled realization with the third subsystem to obtain a total-system model. Section 3.3 gives an example of this approach applied to modelling the experimental apparatus.

3.3   Example: Modelling the Experimental Apparatus

Application of the modular modelling approach to the experimental system enables a total-system model to be developed by performing the following steps:

1. Partition the system into subsystems.

2. Develop subsystem models of the form of Equation (3.9).

3. Concatenate the subsystem models using the SSMCM to obtain a state-space representation of the two-link flexible manipulator with the mini-manipulator at its tip.

This section gives a detailed description of the system partitioning, the subsystem modelling processes, and the subsequent concatenation of the subsystem models.

3.3.1   System Partitioning

Figure 3.2 illustrates how the experimental apparatus can be represented as three subsystems coupled by constraint forces and control inputs. Specifically, the flexible main arm is represented by a first link that is pinned at its base and contains control inputs from both the shoulder and elbow motors. This link is coupled through constraint forces at the elbow joint to the second link. The third subsystem consists of the mini-manipulator and its control inputs, and the mini-manipulator base rigidly constrained to the second link.

3.3.2   Subsystem Modelling

With the three subsystems identified, the second step of the modelling process requires developing subsystem state-space models of the form of Equation (3.9). This section describes the subsystem modelling processes.
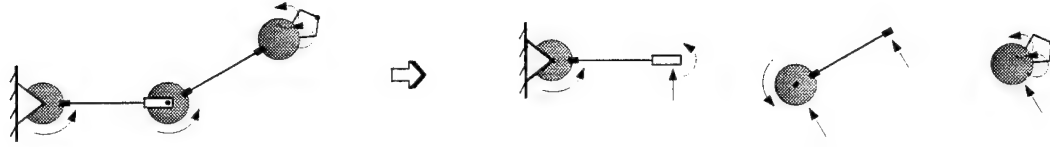
Figure 3.2: **System Partitioning of the Experimental Apparatus**

This modular approach enables the modelling of the experimental apparatus to be partitioned into modelling subsystems, and then concatenating subsystem models to obtain a total-system model. This figure illustrates how the experimental apparatus can be represented as three subsystems: two flexible links and the mini-manipulator. The control torques are represented by curved arrows, while the straight arrows represent the constraint forces.

Modelling the Mini-Manipulator

The mini-manipulator subsystem consists of a base and four dynamic links. The base is coupled to the main arm through constraint forces, and the links are actuated by two control inputs. A schematic of the mini-manipulator subsystem is shown in Figure 3.3.

As described in Chapter 2, the mini-manipulator was designed to have very light links. The lightweight nature of the links can be exploited to simplify greatly the modelling and control design for the entire system. As Kraft demonstrated [26], the lightweight links enable the dynamics of the mini-manipulator to be represented accurately as a dynamic tip mass, m_T, actuated by linear actuators, F_x and F_y. The linear forces are related to the actual control torques through the relation

$$\mathbf{T} = \mathbf{J}^T \mathbf{F} \tag{3.10}$$

where

$$\mathbf{F} = \begin{bmatrix} F_x \\ F_y \end{bmatrix} \tag{3.11}$$

$$\mathbf{T} = \begin{bmatrix} \tau_1 \\ \tau_2 \end{bmatrix} \tag{3.12}$$

$$\tag{3.13}$$

and $\mathbf{J}$ is the mini-manipulator Jacobian mapping the angular velocities at the joints, $\dot{\theta}$, to linear velocities at the tip of the mini-manipulator, $\mathbf{v}$, such that

$$\mathbf{v} = \mathbf{J}\dot{\theta}. \tag{3.14}$$
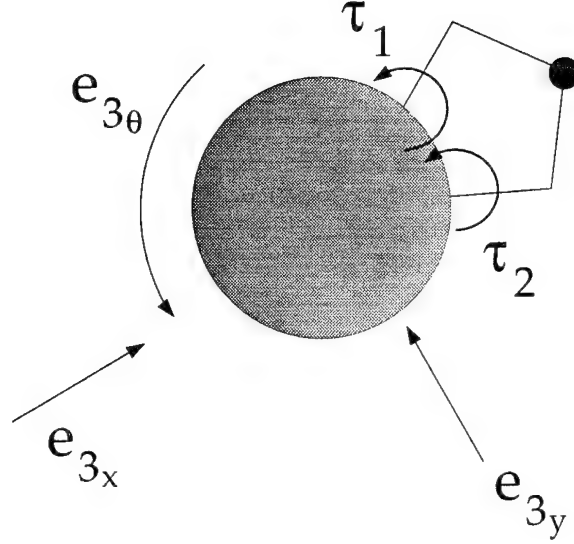
Figure 3.3: **Schematic of Subsystem 3: The Mini-Manipulator**

This figure is a schematic of the mini-manipulator subsystem. Shown in the figure are the constraint forces that couple this subsystem to the second link, as well as the mini-manipulator control torques.

Appendix B defines the Jacobian and other kinematic relationships for the mini-manipulator.

A schematic of the approximate mini-manipulator system is shown in Figure 3.4.   For the mini-manipulator utilized in this research, Andersen [27] experimentally determined an effective tip mass of $m_T = 0.065$ kg. Thus, the approximate linear equations of motion of the mini-manipulator dynamics can be written as

$$\ddot{x}_{m_B} = \frac{1}{m_B + m_T}\left(e_{3_x} - F_x\right) \tag{3.15}$$

$$\ddot{y}_{m_B} = \frac{1}{m_B + m_T}\left(e_{3_y} - F_y\right) \tag{3.16}$$

$$\ddot{\theta}_{m_B} = \frac{1}{I}\left(e_{3_\theta} - F_y x_{m_T}\right) \tag{3.17}$$

$$\ddot{x}_{m_T} = \frac{1}{m_T}F_x \tag{3.18}$$

$$\ddot{y}_{m_T} = \frac{1}{m_T}F_y \tag{3.19}$$
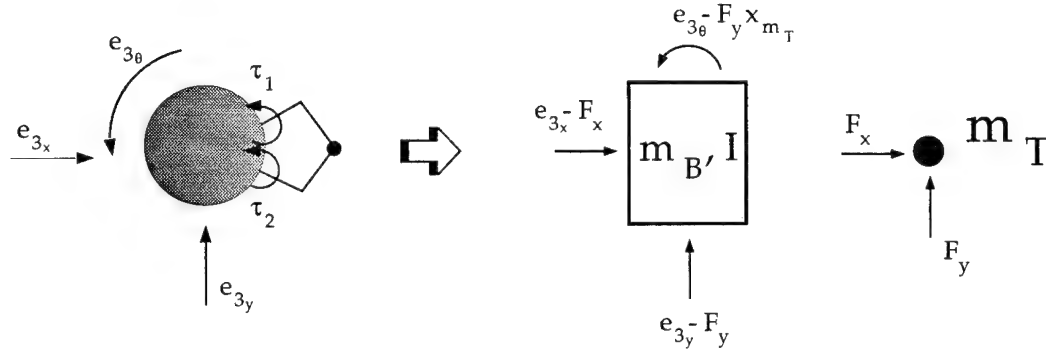
Figure 3.4: **Approximate Mini-Manipulator Model**

The complicated nonlinear dynamics of the mini-manipulator can be accurately represented as a tip mass m_T actuated by linear actuators F_x and F_y, and a base mass and inertia m_B and I.

where x_{m_B}, y_{m_B}, and θ_{m_B} represent the translational and rotational motion of the base at the point where it is connected to the second link, m_B represents the mass of the mini-manipulator subsystem minus the identified tip mass, m_t, and I represents the rotational inertia of the mini-manipulator subsystem about the point of connection with the second subsystem. x_{m_T} and y_{m_T} represent the motion of the mini-manipulator tip relative to its base.

Since the purpose of the mini-manipulator at the end of the flexible arm is to produce much higher performance than is possible with the flexible arm alone, it is reasonable and very generic to assume that the controllers for the two systems will be bandwidth separated [26]. This assumption enables Equations (3.15) through (3.19) to be simplified further to

$$\ddot{x}_{m_B} \approx \frac{1}{m_B + m_T} e_{3_x} \tag{3.20}$$

$$\ddot{y}_{m_B} \approx \frac{1}{m_B + m_T} e_{3_y} \tag{3.21}$$

$$\ddot{\theta}_{m_B} \approx \frac{1}{I} e_{3_\theta} \tag{3.22}$$

$$\ddot{x}_{m_T} = \frac{1}{m_T} F_x \tag{3.23}$$

$$\ddot{y}_{m_T} = \frac{1}{m_T} F_y. \tag{3.24}$$

Observations Equations (3.20) through (3.24) can be expressed in the form of Equation (3.9) and used in the subsystem concatenation process to develop a total-system realization of the experimental apparatus. However, the concatenation process can be facilitated by identifying and exploiting the physics inherent in Equations (3.20) through (3.24). The physical interpretation of Equations (3.20) through (3.24) is that the significant coupling effects of the mini-manipulator on the main arm are due to the mini-manipulator mass and inertia. Furthermore, Equations (3.23) and (3.24) imply that the mini-manipulator-tip dynamics are decoupled from the base. Recognizing and exploiting these physical characteristics can reduce the subsystem concatenation process from concatenating three subsystems to the concatenation of subsystems one and two, and then appending the dynamics in Equations (3.23) and (3.24). Specifically, if the low frequency dynamics (static mass and inertia) of the mini-manipulator is modelled as an effective tip mass and inertia of the second link, then the mini-manipulator tip dynamics of Equations (3.23) and Equations (3.24) can be separated from the main-arm dynamics. This has two important implications. First, it enables the mini-manipulator dynamic model to be appended simply to a model of the main arm. Second, exploiting this physical decoupling enables the control design for the main arm and the mini-manipulator to be performed independently.

Hence, given that the mini-manipulator mass, $m_B + m_T$, and inertia, I, are included in the second subsystem model as a tip mass and inertia, the mini-manipulator subsystem can be represented by

$$\ddot{x}_{m_T} = \frac{1}{m_T} F_x \tag{3.25}$$

$$\ddot{y}_{m_T} = \frac{1}{m_T} F_y. \tag{3.26}$$

Expressing the equations of motion for the mini-manipulator in the form of Equation (3.9), the mini-manipulator subsystem model is given as

$$\dot{\mathbf{x}}_3 = \mathbf{A}_3 \mathbf{x}_3 + \mathbf{B}_3^u \mathbf{u}_3(t)$$

$$\mathbf{z}_3 = \mathbf{C}_3^z \mathbf{x}_3 \tag{3.27}$$

$$\tag{3.28}$$

where

$$\mathbf{x}_3 = \begin{bmatrix} x_{m_T} \\ y_{m_T} \\ \dot{x}_{m_T} \\ \dot{y}_{m_T} \end{bmatrix} \tag{3.29}$$

$$\mathbf{u}_3 = \begin{bmatrix} F_x \\ F_y \end{bmatrix} \tag{3.30}$$

$$\mathbf{A}_3 = \begin{bmatrix} 0 & 0 & 1 & 0 \\ 0 & 0 & 0 & 1 \\ 0 & 0 & 0 & 0 \\ 0 & 0 & 0 & 0 \end{bmatrix} \tag{3.31}$$

$$\mathbf{B}_3^u = \begin{bmatrix} 0 & 0 \\ 0 & 0 \\ \frac{1}{m_T} & 0 \\ 0 & \frac{1}{m_T} \end{bmatrix} \tag{3.32}$$

The outputs of interest are the tip position relative to the base, yielding

$$\mathbf{z}_3 = \begin{bmatrix} x_{m_T} \\ y_{m_T} \end{bmatrix} \tag{3.33}$$

and

$$\mathbf{C}_3^z = \begin{bmatrix} 1 & 0 & 0 & 0 \\ 0 & 1 & 0 & 0 \end{bmatrix} . \tag{3.34}$$

Because of the approximate decoupling, concatenating this model with the model of the main arm is equivalent to appending simply the mini-manipulator model to the main-arm model.

Modelling the Second Link

Figure 3.5 illustrates the second-link subsystem. It consists of a rigid hub, a flexible link, and a rigid tip. The inputs to this system are a control torque at the hub, and constraint forces at the hub location where the link is pinned to the first link. Because the rigid tip includes the mass and inertia of the rigidly connected mini-manipulator base, there are no constraint
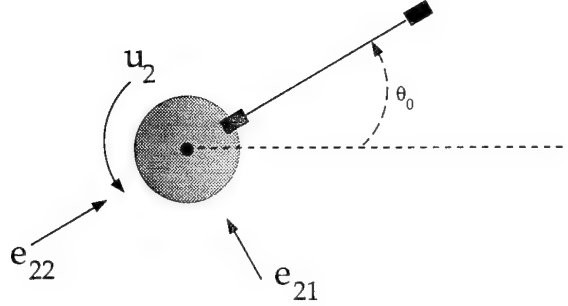
Figure 3.5: **Schematic of Subsystem 2: The Second Link**

This figure is a schematic of subsystem two. The inputs to this system are a control torque u_2 at the hub, and constraint forces e_{21} and e_{22} at the hub location where the link is pinned to the first link. Because the rigid tip includes the mass and inertia of the rigidly connected mini-manipulator base, there are no constraint forces at the tip of the second link. θ_0 is the nominal relative angle between the first and second link.

forces at the tip of the second link. Also included in the figure is a reference angle, θ_0, which is the nominal relative angle between the first and second link.   Appendix C details the modelling of the second link, based on the finite-element method, and the development of the second-subsystem model of the form

$$
\begin{aligned}
\dot{\mathbf{x}}_2 &= \mathbf{A}_2\mathbf{x}_2 + \mathbf{B}_2^u\mathbf{u}_2(t) + \mathbf{B}_2^e\mathbf{e}_2 \\
\mathbf{z}_2 &= \mathbf{C}_2^z\mathbf{x}_2 \\
\mathbf{f}_2 &= \mathbf{C}_2^f\mathbf{x}_2 \\
\mathbf{d}_2 &= \mathbf{C}_2^d\mathbf{x}_2
\end{aligned}
\tag{3.35}
$$

where the constraint-force input is given by

$$
\mathbf{e}_2 = \left[\begin{array}{c} e_{21} \\ e_{22} \end{array} \right]
\tag{3.36}
$$

and the velocity (flow) and position (displacement) at the interface, or pinned connection with the first link, are given by

$$
\mathbf{f}_2 = \left[\begin{array}{c} f_{21} \\ f_{22} \end{array} \right]
\tag{3.37}
$$

$$\mathbf{d}_2 = \begin{bmatrix} d_{21} \\ d_{22} \end{bmatrix} \tag{3.38}$$

where f_{ij} and d_{ij} are in the direction of e_{ij} shown in Figure 3.5.

Modelling the First Link

Figure 3.6 gives a schematic of subsystem one. This subsystem consists of a pinned rigid hub, and a flexible link connected to a rigid tip. The inputs to this subsystem are control inputs at both the hub and tip, and constraint forces at the tip caused by the pinned connection to the second link. Appendix C details the modelling of the first link, in which
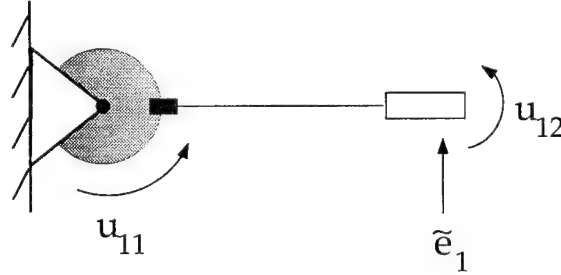
Figure 3.6: **Schematic of Subsystem 1: The First Link**

This figure is a schematic of subsystem one.

axial deflections are neglected, and the development of the first subsystem model of the form

$$
\begin{aligned}
\dot{\mathbf{x}}_1 &= \mathbf{A}_1 \mathbf{x}_1 + \mathbf{B}_1^u \mathbf{u}_1(t) + \tilde{\mathbf{B}}_1^e \tilde{\mathbf{e}}_1 \\
\mathbf{z}_1 &= \mathbf{C}_1^z \mathbf{x}_1 \\
\tilde{\mathbf{f}}_1 &= \tilde{\mathbf{C}}_1^f \mathbf{x}_1 \\
\tilde{\mathbf{d}}_1 &= \tilde{\mathbf{C}}_1^d \mathbf{x}_1
\end{aligned}
\tag{3.39}
$$

where

$$\mathbf{u}_1 = \begin{bmatrix} u_{11} \\ u_{12} \end{bmatrix}, \tag{3.40}$$

$\tilde{\mathbf{e}}_1$ corresponds to the scalar interface force on subsystem one at the pinned connection to subsystem two in the direction shown in Figure 3.6, $\tilde{\mathbf{f}}_1$ and $\tilde{\mathbf{d}}_1$ are the corresponding flow

and displacement in the same direction, $\tilde{\mathbf{B}}_1^u$ is the corresponding input matrix, and $\tilde{\mathbf{C}}_1^f$ and $\tilde{\mathbf{C}}_1^d$ are the corresponding output matrices. Because of the convention assumed by the SSMCM, Equation 3.39 must be rewritten so that the interface variables satisfy the relation

$$\mathbf{e}_1 = -\mathbf{e}_2 \tag{3.41}$$

$$\mathbf{f}_1 = \mathbf{f}_2 \tag{3.42}$$

$$\mathbf{d}_1 = \mathbf{d}_2. \tag{3.43}$$

For a nominal elbow angle θ_0, this relation can be satisfied by defining

$$\begin{bmatrix} f_{11} \\ f_{12} \end{bmatrix} = \begin{bmatrix} cos(\theta_0) \\ sin(\theta_0) \end{bmatrix} \tilde{\mathbf{f}}_1 \tag{3.44}$$

$$\begin{bmatrix} d_{11} \\ d_{12} \end{bmatrix} = \begin{bmatrix} cos(\theta_0) \\ sin(\theta_0) \end{bmatrix} \tilde{\mathbf{d}}_1 \tag{3.45}$$

$$\tilde{\mathbf{e}}_1 = \begin{bmatrix} cos(\theta_0) & sin(\theta_0) \end{bmatrix} \begin{bmatrix} e_{11} \\ e_{12} \end{bmatrix} \tag{3.46}$$

where e_{1i} is the constraint acting on subsystem one in the direction of e_{2i}, and f_{1i} and d_{1i} are the interface output of subsystem one in the same direction. Then, defining

$$\mathbf{f}_1 = \begin{bmatrix} f_{11} \\ f_{12} \end{bmatrix} \tag{3.47}$$

$$\mathbf{d}_1 = \begin{bmatrix} d_{11} \\ d_{12} \end{bmatrix} \tag{3.48}$$

$$\mathbf{e}_1 = \begin{bmatrix} e_{11} \\ e_{12} \end{bmatrix} \tag{3.49}$$

$$\mathbf{B}_1^e = \tilde{\mathbf{B}}_1^e \begin{bmatrix} cos(\theta_0) & sin(\theta_0) \end{bmatrix} \tag{3.50}$$

$$\mathbf{C}_1^f = \begin{bmatrix} cos(\theta_0) \\ sin(\theta_0) \end{bmatrix} \tilde{\mathbf{C}}_1^f \tag{3.51}$$

$$\mathbf{C}_1^d = \begin{bmatrix} cos(\theta_0) \\ sin(\theta_0) \end{bmatrix} \tilde{\mathbf{C}}_1^d \tag{3.52}$$

Equation (3.39) can be written in the necessary form to be concatenated with subsystem two

$$\dot{\mathbf{x}}_1 = \mathbf{A}_1\mathbf{x}_1 + \mathbf{B}_1^u\mathbf{u}_1(t) + \mathbf{B}_1^e\mathbf{e}_1$$

$$\mathbf{z}_1 = \mathbf{C}_1^z \mathbf{x}_1 \tag{3.53}$$
$$\mathbf{f}_1 = \mathbf{C}_1^f \mathbf{x}_1$$
$$\mathbf{d}_1 = \mathbf{C}_1^d \mathbf{x}_1.$$

Equation (3.53) is dependent on the nominal elbow angle θ_0. However, for a given configuration, the resulting system model can be obtained readily by concatenating the models expressed in Equations (3.35) and (3.53), without rederiving Equations (3.35) and (3.39).

3.3.3 Subsystem Concatenation

Section 3.3.2 pointed out that the subsystem concatenation process can be reduced to concatenating models for subsystems one and two to develop a main-arm model, and then appending the mini-manipulator tip dynamics to this realization. For a given elbow angle θ_0, the system equations generated by the SSMCM are given as

$$\dot{\mathbf{x}} = \mathbf{A}\mathbf{x} + \tilde{\mathbf{B}}\tilde{\mathbf{u}} \tag{3.54}$$
$$\mathbf{y} = \mathbf{C}\mathbf{x} \tag{3.55}$$

where $\mathbf{x} \in \mathbb{R}^{ns_1+ns_2-(nf_i+nd_i)}$ is the total-system state vector, $\mathbf{A}$ and $\tilde{\mathbf{B}}$ are the total-system transition and input matrices, $\mathbf{C}$ is the total-system output matrix, and the system inputs $\tilde{\mathbf{u}}$ and outputs $\mathbf{y}$ are defined as

$$\tilde{\mathbf{u}} = \begin{bmatrix} \mathbf{u}_1 \\ \mathbf{u}_2 \end{bmatrix} \tag{3.56}$$

$$\mathbf{y} = \begin{bmatrix} \mathbf{z}_1 \\ \mathbf{z}_2 \end{bmatrix}. \tag{3.57}$$

$\tilde{\mathbf{B}}$ and $\tilde{\mathbf{u}}$ can be simplified since one element of $\mathbf{u}_1$ is related to u_2. Specifically,

$$u_{12} = -u_2 \tag{3.58}$$

at the pinned joint. Consequently, the main-arm equations of motion can be written as

$$\dot{\mathbf{x}} = \mathbf{A}\mathbf{x} + \mathbf{B}\mathbf{u} \tag{3.59}$$
$$\mathbf{y} = \mathbf{C}\mathbf{x} \tag{3.60}$$

where

$$\mathbf{u} = \begin{bmatrix} u_1 \\ u_2 \end{bmatrix} \tag{3.61}$$

$$\mathbf{B} = \begin{bmatrix} \tilde{\mathbf{B}}(:,1) & \tilde{\mathbf{B}}(:,3) - \tilde{\mathbf{B}}(:,2) \end{bmatrix}, \tag{3.62}$$

and $\tilde{\mathbf{B}}(:,i)$ is the ith column of $\tilde{\mathbf{B}}$.

3.3.4   Comparison with Experimental Data

Because the model of the decoupled mini-manipulator dynamic tip mass was already veri-fied [27], model verification requires comparing the model of the main-arm with the exper-imental system. To verify the accuracy of the model of the flexible main arm, comparisons were made between the model and the experimental apparatus for various nominal elbow angles.   Experimental responses were obtained from sine sweep tests using a Solartron Model 1254 Frequency Response Analyzer. When necessary, very-low-gain proportional in-dependent joint controllers were implemented to keep the manipulator from drifting during the experiments. In these comparisons, the first four flexible modes were included in the model. Furthermore, the parameters used in these initial models were the actual physical parameters given in Appendix C, and were *not* altered to obtain a "best fit".

Comparisons of the collocated transfer functions for a 45 degree elbow angle are given in Figures 3.7 and 3.8.   Figure 3.7, the shoulder-joint frequency response, shows good agreement between the model and experiment for both magnitude and phase.   In this response, the second and fourth system modes are dominant, with a very small contribution from the first and third system modes. This implies that the first and third modes are barely excited by the shoulder motor in a 45 degree configuration.   The elbow-joint frequency response in Figure 3.8 contains sets of double peaks in the magnitude plot, implying that the elbow motor couples strongly into all the system modes. This figure illustrates that the model predicts accurately the low-frequency cantilevered zero, and the first, third, and fourth system modes.

Comparisons of the collocated transfer functions for a 90 degree elbow angle are given in Figures 3.9 and 3.10.   Figure 3.9 once again demonstrates excellent agreement between the model and experiment for both magnitude and phase. In this 90 degree configuration, only the second and fourth system modes are present, implying that the shoulder motor does not couple into the first and third system modes. Figure 3.10 illustrates the accuracy
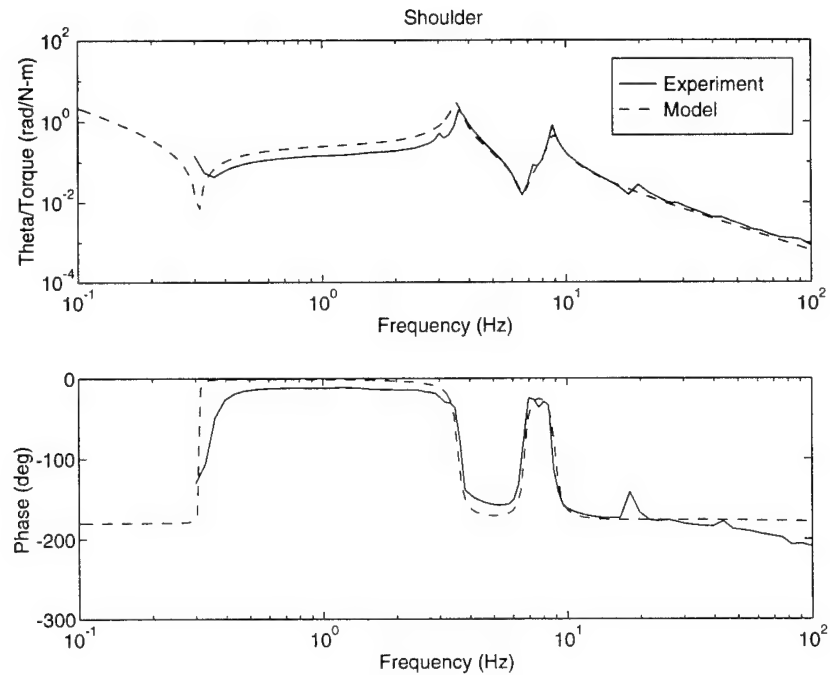
Figure 3.7: **Shoulder-Joint Frequency Response: 45 Degree Elbow Angle**

This figure shows the frequency response, both magnitude and phase, corresponding to the shoulder motor for a 45 degree nominal elbow angle. This response is dominated by the second and fourth system modes. These plots show excellent agreement between the model and experiment for both magnitude and phase.

of the model in predicting the first four flexible modes. As in the 45 degree configuration, the elbow motor couples strongly into all the system modes.
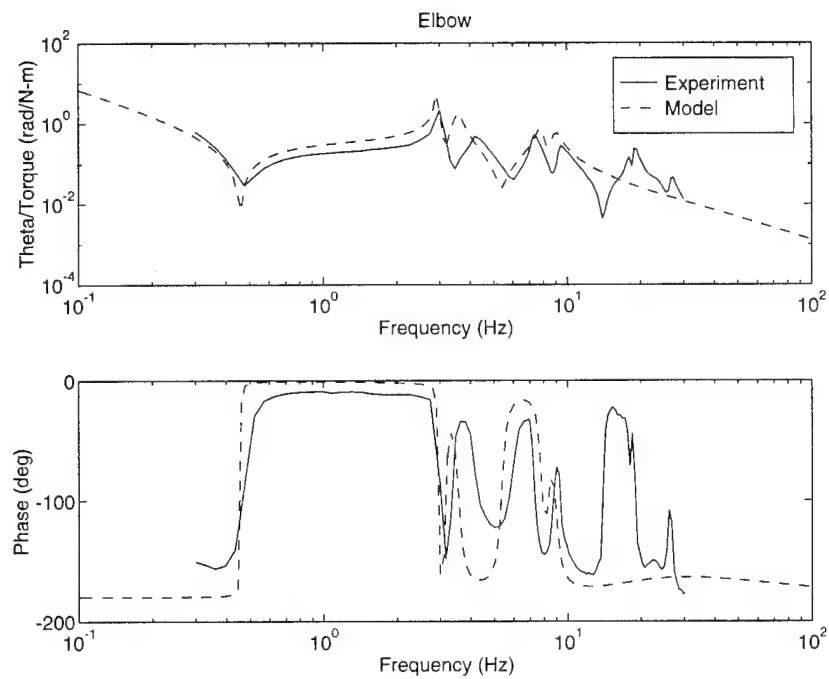
Figure 3.8: **Elbow-Joint Frequency Response: 45 Degree Elbow Angle**

For a 45 degree elbow angle, the models predicts accurately the low-frequency can-tilevered zero, and the first, third, and fourth system modes. The magnitude plot contains significant sets of double peaks, implying that the elbow motor couples strongly into all the system modes.
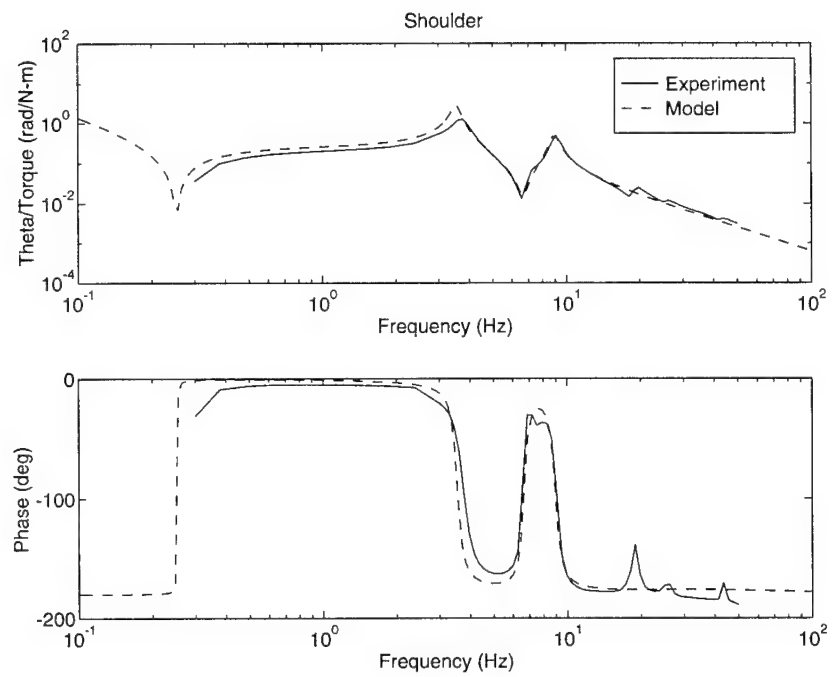
Figure 3.9: **Shoulder-Joint Frequency Response: 90 Degree Elbow Angle**
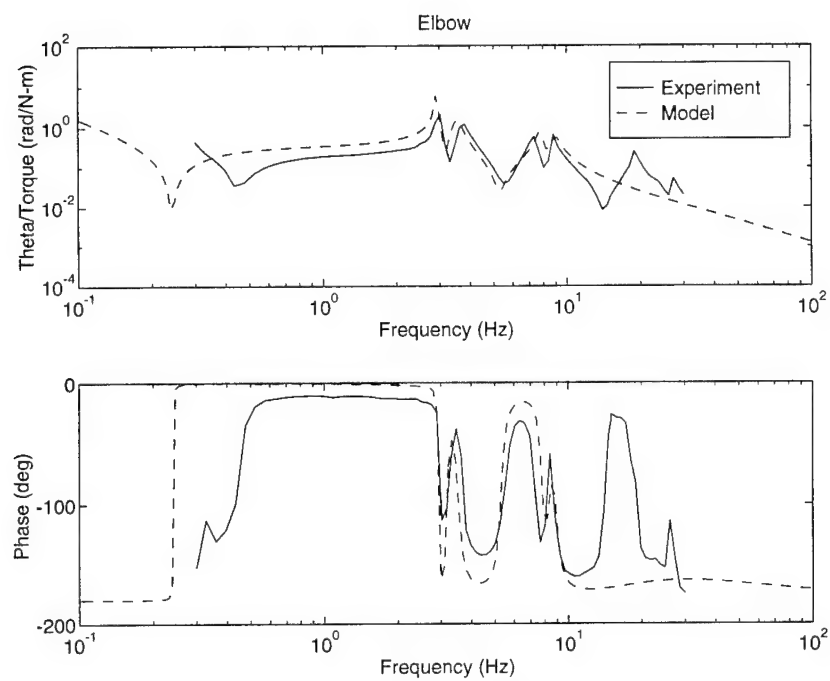
Figure 3.10: **Elbow-Joint Frequency Response: 90 Degree Elbow Angle**

Observations

Small Variation with Configuration   Figure 3.11 shows a comparison of experimental magnitude plots for a 45 and 90 degree elbow angle.   This figure indicates that the dynamics
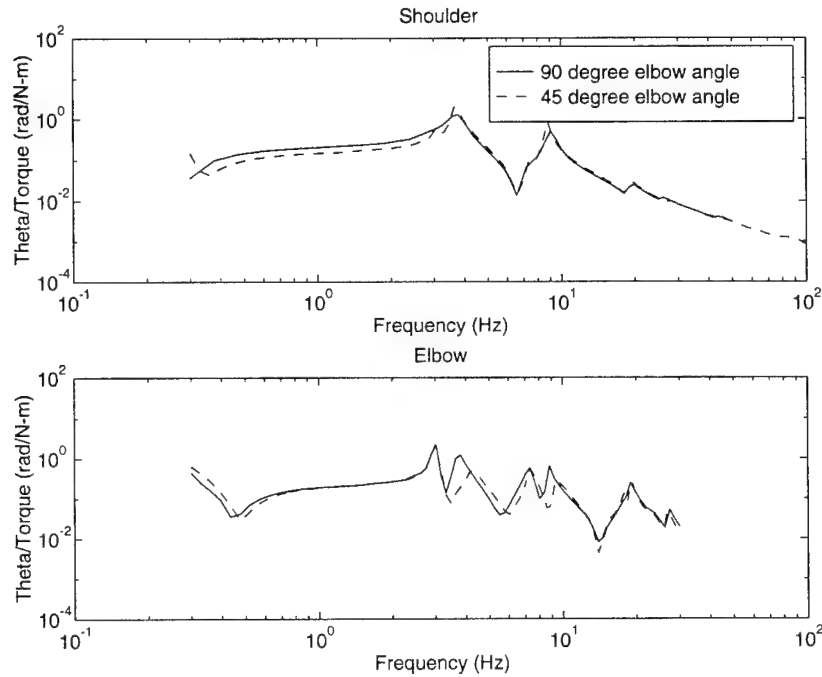
Figure 3.11: **Comparison Between a 45 and 90 Degree Configuration**

This figure shows a comparison of experimental magnitude plots for a 45 and 90 degree elbow angle. It is clear that the flexible dynamics of the manipulator vary only slightly with configuration. As a result, a single linear model can be used to represent accurately the system for a wide range of configurations.

of the system vary only slightly with configuration. As a result, a single model can be used to represent accurately the system for a wide range of configurations. This is important in terms of enabling a simplified control design. Specifically, a single controller designed for a nominal elbow angle can be used to control the manipulator, and its flexible dynamics, throughout a large portion of its workspace.

Decoupled Link Dynamics   Comparison of main-arm models for various configurations enabled some interesting observations. First of all, as verified by the experimental plots in

Figure 3.11, it was observed that the natural frequencies of the main arm are essentially constant over a wide range of elbow angles. Second, the corresponding system mode shapes are qualitatively very similar. Figure 3.12 shows comparisons of the first two theoretical flexible modes for 90 degree and 0 degree elbow-angle models. For each configuration, the first mode is primarily an excitation of the second link, and the second mode is primarily an excitation of the first link. This characteristic is independent of configuration. The physical explanation of this phenomenon is that at high-frequencies, there is very little energy exchange between the two link subsystems, due primarily to the large mass and inertia of the elbow motor. This low energy exchange implies that the link dynamics are essentially decoupled from each other, and the two subsystems are therefore only one-way coupled through the elbow-motor control input. This characteristic was first identified by Oakley [5].

Approximate System Model

These physical characteristics were exploited to develop a simplified model of the experimental system for a 90 degree elbow angle. Specifically, for an elbow angle of 90 degrees, the system behaves like two subsystems that are one-way coupled through the elbow control input. The approximate system is shown in Figure 3.13. The first subsystem represents a pinned flexible beam with an effective tip mass to account for the mass of the second-link subsystem. The second subsystem is a pinned flexible beam with an effective tip mass and inertia representing the mini-manipulator subsystem. The two subsystems are one-way coupled through the elbow motor. Because the high-frequency modes for the individual links vary only slightly with configuration, this approximate system model can be used to design a controller which operates over a wide range of elbow angles. The system matrices for this main-arm model are given in Appendix F.

To verify the accuracy of the approximate main-arm model, comparisons were made with the experimental apparatus. Figure 3.14 shows a comparison of the collocated transfer functions from torque to motor angle for both the shoulder and elbow motors for a ninety degree elbow angle. In this model, some parameters were modified slightly to obtain a better fit. Model accuracy of the first two system modes, which dominate the motion of the system, will enable high-performance control design for this system.
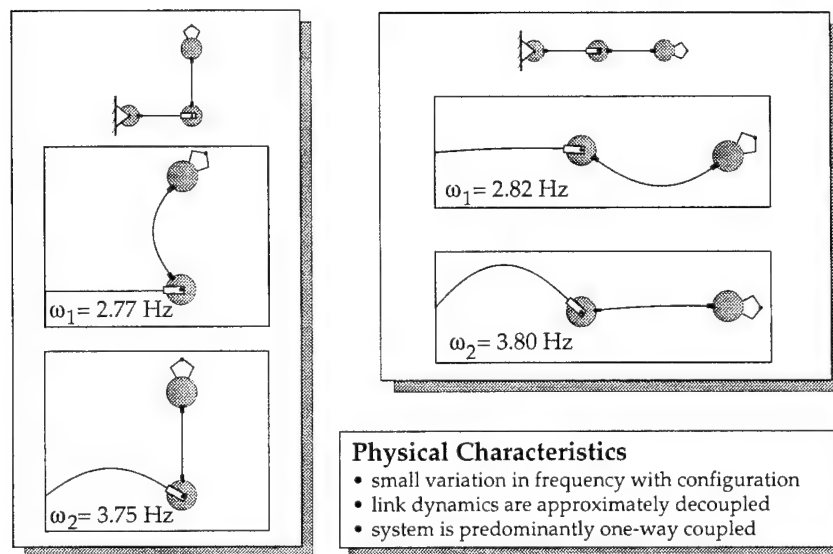
Figure 3.12: **Theoretical System Modes**

This figure illustrates the first two theoretical flexible modes shapes for two config-urations. The small variation in natural frequency and corresponding mode shapes for the flexible modes indicates that the link dynamics are essentially decoupled for a wide range of elbow angles. Thus, the two subsystems are only one-way coupled through the elbow-motor control input. This characteristic, first identified by Oak-ley, can be exploited to develop an approximate system model that is accurate over a wide range of elbow angles.
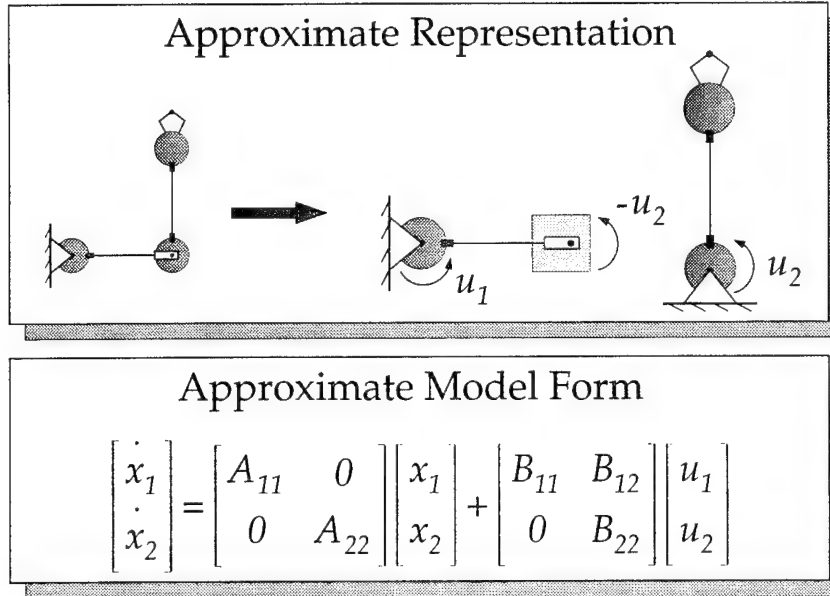
Figure 3.13: **Approximate Main-Arm Model**

Because the high-frequency link dynamics are approximately decoupled, the two-link flexible manipulator can be well approximated as two subsystems that are one-way coupled through the elbow control input. The first subsystem represents a pinned flexible beam with an effective tip mass to account for the mass of the second-link subsystem. The second subsystem is a pinned flexible beam with an effective tip mass and inertia representing the mini-manipulator subsystem. The two subsystems are one-way coupled through the elbow motor. The resulting model form will be exploited in Chapter 5 in the control-design process.

3.3.5   Total-System Model

With the accurate main-arm model developed in the last section, a total-system model is obtained by appending the model of the mini-manipulator tip dynamics. Specifically, the total-system dynamics can be represented by

$$
\begin{bmatrix} \dot{\mathbf{x}}_1 \\ \dot{\mathbf{x}}_2 \\ \dot{\mathbf{x}}_3 \end{bmatrix} = \begin{bmatrix} \mathbf{A}_{11} & 0 & 0 \\ 0 & \mathbf{A}_{22} & 0 \\ 0 & 0 & \mathbf{A}_{33} \end{bmatrix} \begin{bmatrix} \mathbf{x}_1 \\ \mathbf{x}_2 \\ \mathbf{x}_3 \end{bmatrix} + \begin{bmatrix} \mathbf{B}_{11} & \mathbf{B}_{12} & 0 \\ 0 & \mathbf{B}_{22} & 0 \\ 0 & 0 & \mathbf{B}_{33} \end{bmatrix} \begin{bmatrix} \mathbf{u}_1 \\ \mathbf{u}_2 \\ \mathbf{u}_3 \end{bmatrix} \tag{3.63}
$$

where $\mathbf{x}_1$ and $\mathbf{x}_2$ represent the dynamics of the main arm one-way coupled through the elbow control u_2, and $\mathbf{x}_3$ represents the decoupled tip dynamics of the mini-manipulator.
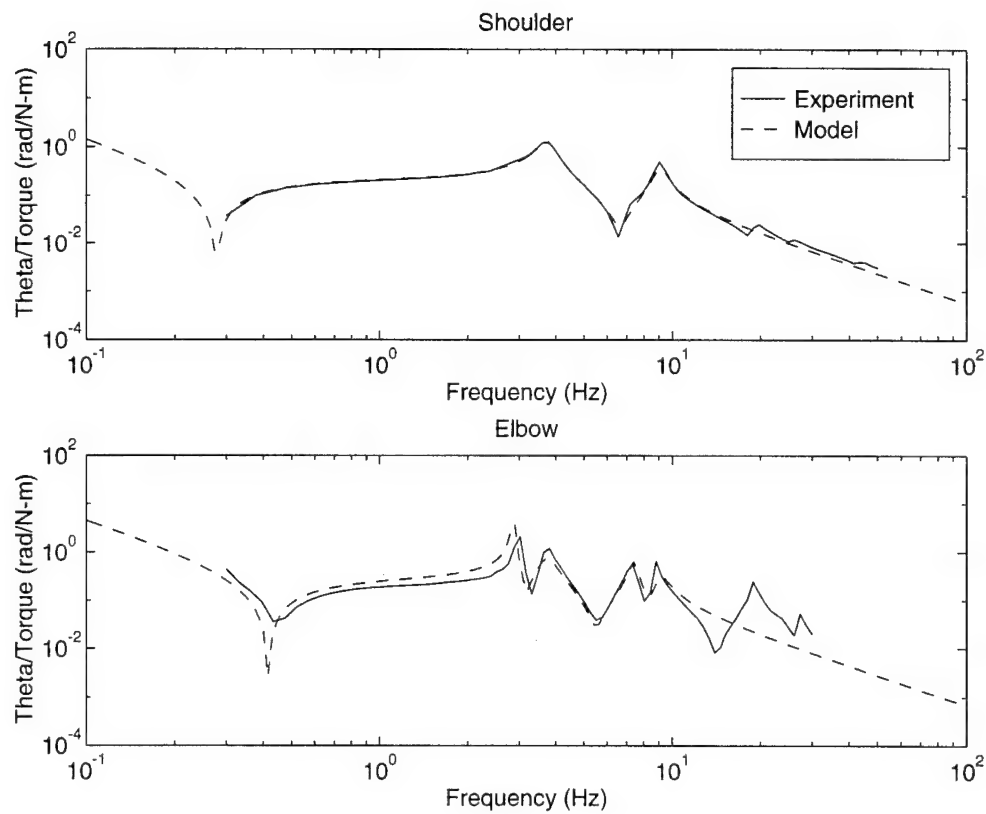
Figure 3.14: **Modelling Results**

This figure shows excellent correspondence between the approximate main-arm model with the experimental apparatus for a ninety degree elbow angle. These plots verify the approximations that led to modelling the main arm as two subsystems one-way coupled through a control input.

3.4   Summary

This chapter has presented a modular approach to modelling multi-link flexible manipulators. This approach is based on a new model concatenation technique that enables the concatenation of two state-space models that contain, as inputs, the constraint forces that physically couple the subsystems. By judiciously solving for the constraint forces, a total-system model of the coupled subsystems is attained.

The modularity of this approach leads to a number of advantages in terms of modelling multi-link flexible manipulators. First, it enables modelling complex systems to be partitioned into smaller more tractable modelling problems. A second advantage is that subsystem modifications, substitutions, and additions can be easily accommodated, without rederiving equations of motion for the unaffected subsystems. Furthermore, this approach is amenable to modelling systems in a number of configurations.

This modular approach has been applied to the experimental apparatus. The approach involved modelling independently the two flexible links, and then concatenating these subsystem models to obtain a model of the flexible main arm. This was performed for various configurations and the corresponding models were verified by comparisons with the experimental system. A total-system model of the flexible main arm/mini-manipulator system was developed by concatenating the flexible-arm model with a model of the mini-manipulator tip dynamics.

In Chapters 4 and 5, the model developed in this chapter will be used for trajectory generation and control design for the experimental apparatus.

Chapter 4

Trajectory Generation

This chapter describes a trajectory-generation approach for repositioning quickly multi-link flexible manipulators, and presents an application of this approach to the experimental apparatus. Given the reference commands as inputs, this technique generates optimal desired state histories and the corresponding feedforward-control inputs to the plant's actuators for the repositioning. Figure 4.1 illustrates how the resulting trajectory generator fits into the solution framework described in Chapter 1.
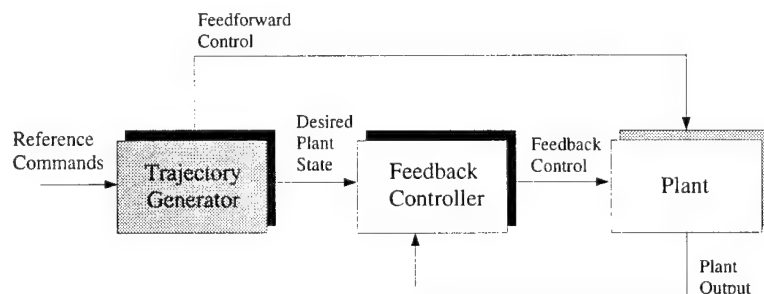
Figure 4.1: **Control Framework**

This chapter describes one component of the control-system framework: the optimal-trajectory generator. Taking the reference commands as inputs, the trajectory generator computes the desired plant-state history and the corresponding feedforward-control input to the plant's actuators to effect this desired motion.

The goal of this research is to achieve high-performance point-to-point repositioning of multi-link flexible manipulators with local end-point manipulation. In the repositioning,

only the slew time and the final tip position of the manipulator are specified. The control strategy developed to meet this goal requires transporting quickly the mini-manipulator to within a target area, so that the desired target point is within its reach. The corresponding main-arm performance objective requires repositioning quickly the main arm, and thereafter maintaining the mini-manipulator within the target area. The requirement of the trajectory generator is to provide a desired state history and feedforward-control input to the main arm to position quickly the mini-manipulator near the target.

There are two characteristics of the point-to-point repositioning problem addressed in this research that are exploited to enable a new trajectory-generation approach. First, because of the redundancy introduced by the mini-manipulator, the main arm does not need to meet *exactly* a specific terminal condition. Instead, the main arm must be positioned rapidly to any location within a very specific area near the desired end-point target. Second, because only the final tip position is specified, the main arm is not required to follow a previously specified path during the repositioning.

This trajectory-generation approach, based on a model-following implementation of a terminal controller, exploits these characteristics. Consequently, this approach offers benefits in terms of performance, simplicity, and computational cost :

- First, the main arm is not required to follow a previously specified path during the repositioning, and is therefore able to follow a "best" path. Because the terminal area to be reached is of finite size, there are a number of acceptable terminal conditions and corresponding paths that the arm can follow. Consequently, this approach generates, in *real time*, an *optimal trajectory* for the main arm. [1] Included in this trajectory is the optimal state history, and the corresponding optimal control input.

- Second, because the only slew-dependent off-line computations of this approach are based on the specified slew time, repositionings of the same slew time require *no additional off-line computations*.

- Third, the precomputations of this approach are *computationally efficient*. This efficiency, enabled by the soft terminal constraints in the terminal-controller design, offers implementation and design benefits.

These three characteristics are described in detail in this chapter.

---

[1] Optimality is defined by a linear-quadratic cost function. This is explained in Section 4.2.1.

4.1 Background

The reference commands for a point-to-point repositioning consist of the final tip position and the slew time. Generating a trajectory based on these commands requires computing a desired state history for the repositioning as well as the corresponding feedforward-control input that, in the presence of an exact model, causes the desired motion.

Typically, trajectory generation for point-to-point repositionings involves two sets of off-line computations. Figure 4.2 illustrates a typical trajectory-generation framework. The trajectory generator takes as input the desired reference commands. Within the trajectory generator, an off-line calculation is performed to compute a desired plant-state history from the reference commands. From this desired output, another off-line calculation yields the corresponding feedforward-control input to the plant's actuators.
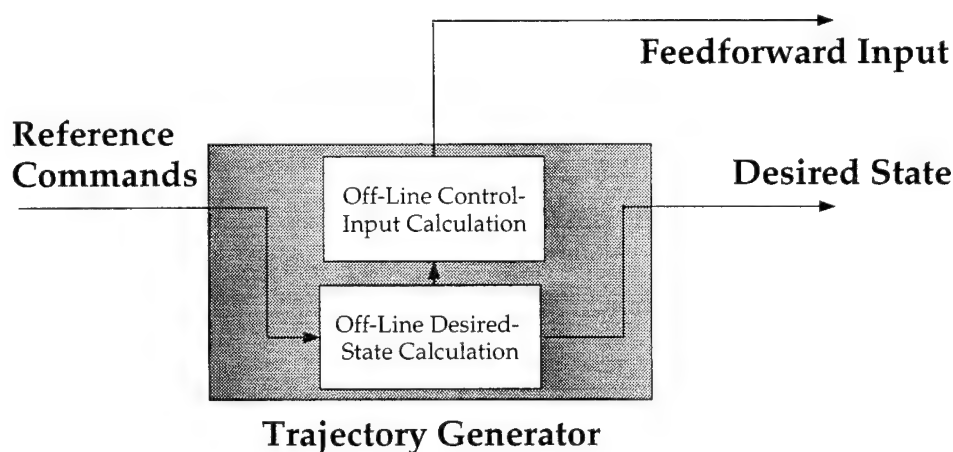
Figure 4.2: **Typical Trajectory-Generation Framework**

The trajectory generator takes as input the desired reference commands. Within a typical trajectory generator, an off-line calculation is performed to compute a desired plant-state history from the reference commands. From this desired output, another off-line computation generates the corresponding feedforward-control input.

Recent research has addressed the inverse-dynamics problem for flexible manipulators to calculate the exact control inputs to follow a *specified* manipulator end-point path. A good representation of this research can be found in [15], [16], and [17]. These methods have been verified experimentally and demonstrated to work quite well.

Furthermore, numerous methods exist for taking the reference commands of a point-to-point repositioning and generating a desired plant output. The most common method involves fitting a spline between the initial and final tip positions, and then computing desired joint angles through inverse kinematics assuming rigid links. This method, however, is sub-optimal for flexible manipulators due to the rigid-links assumption. Another method computes desired end-point histories for point-to-point motions with minimal residual vibration by setting the end-point acceleration and jerk to zero ([42] and [43]). In addition, input-shaping techniques can be applied to generate a desired output path resulting in reduced residual vibrations ([44], [20], [21], [22], [23], [45], and [19]).

4.2   Trajectory-Generation Approach

In contrast to typical trajectory-generation approaches, the approach developed in this dissertation generates in real time an optimal output for the repositioning, and generates *simultaneously* the corresponding control input. This approach is based on the model-following control framework shown in Figure 4.3 in which a plant model is regulated by a *terminal controller*. Although the structure of this framework is not new, the novelty stems from the model-following implementation of the terminal controller.

Rather than calculate off-line the desired plant output and then the corresponding control inputs, the terminal controller regulates in real time the plant *model* to the desired final position. The output of the terminal controller is also sent to the plant as a feedforward-control input.[2] The corresponding response of the plant model, assuming the model is initialized with the initial conditions of the plant, represents the desired state history for the plant to follow.

Given this model-following framework, successful trajectory generation places specific requirements on the terminal-controller design. This section presents the terminal-controller problem formulation and solution, the specific requirements of the design, and the approach developed to meet these requirements.

---

[2]Because of this model-following implementation, the terminal controller has no effect on the closed-loop stability of the actual plant.
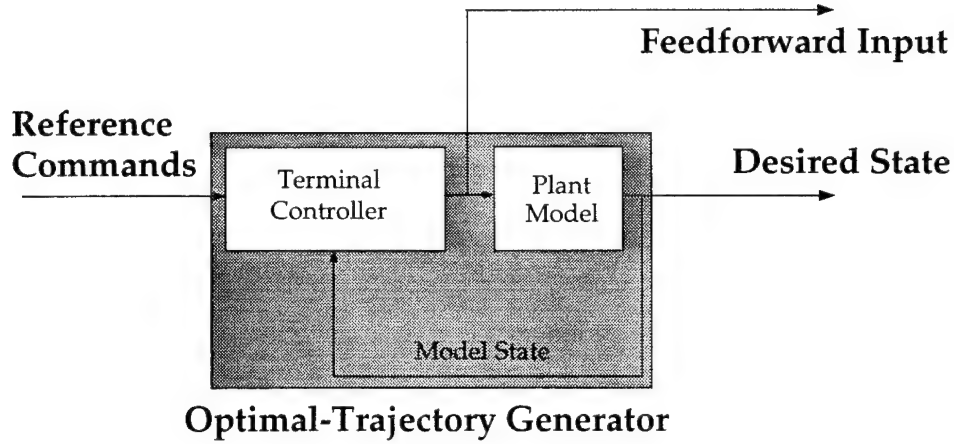
Figure 4.3: Terminal-Controller-Based Trajectory Generator

The terminal-controller-based trajectory-generation framework consists of a plant model regulated by a terminal controller. The output of the terminal controller is sent to the plant as a feedforward-control input. The corresponding response of the plant model to this same input represents the desired state history for the plant to follow during the repositioning.

4.2.1 Problem Formulation and Solution

Suitable trajectory generation reduces to designing a terminal controller that meets the main-arm requirements for a point-to-point repositioning. Specifically, the goal is to bring the main arm close to a desired final state at a specified final time, while at the same time maintaining reasonable values of the state and not exceeding acceptable levels of control effort.

An intuitive way of achieving these performance objectives is to formulate a linear-quadratic performance index that weights the quantities of interest, and then minimize the value of this cost function with respect to the control effort.

As described in Chapter 3, the main-arm dynamics are represented accurately by

$$\dot{\mathbf{x}}(t) = \mathbf{A}\mathbf{x}(t) + \mathbf{B}\mathbf{u}(t), \tag{4.1}$$

where $\mathbf{x}(t)$ is an n-component vector of state elements, $\mathbf{u}(t)$ is an m-component vector of control inputs, and $\mathbf{A}$ and $\mathbf{B}$ are constant system matrices. Control design involves minimizing the cost function

$$\mathbf{J} = \frac{1}{2}(\mathbf{x}^{\mathrm{T}}\mathbf{S}_f\mathbf{x})_{t=t_f} + \frac{1}{2}\int_{t_0}^{t_f}[\mathbf{x}(t)^{\mathrm{T}}\mathbf{Q}_x(t)\mathbf{x}(t) + \mathbf{u}(t)^{\mathrm{T}}\mathbf{Q}_u(t)\mathbf{u}(t)]dt \tag{4.2}$$

with respect to the control input $\mathbf{u}(t)$, and subject to the linear constraints imposed by Equation (4.1). $\mathbf{S}_f$ and $\mathbf{Q}_x(t)$ are positive semidefinite matrices that weight the values of the states at the terminal time $\mathbf{x}(t_f)$ and the values of the intermediate states $\mathbf{x}(t)$. $\mathbf{Q}_u(t)$ is a positive definite matrix that weights the control effort $\mathbf{u}(t)$ expended during the slew. Equation (4.2) corresponds to a regulator design where the desired terminal state is zero. As stated, this problem formulation is known as a *terminal-controller problem* [46], and its solution is well known.

Because of the soft terminal constraints on the main arm, an acceptable terminal-controller design can be determined using a finite weighting on the terminal state. This finite value of $\mathbf{S}_f$ enables a straightforward computationally efficient solution. Specifically, using methods described in [46], the optimal control input $\mathbf{u}(t)$ is found by minimizing Equation (4.2) while solving simultaneously the linear constraints in Equation (4.1). The details of this solution and the corresponding discrete formulation and solution can be found in Appendix D. The optimal feedback law is given as:

$$\mathbf{u}(t) = -\mathbf{K}(t)\mathbf{x}(t), \tag{4.3}$$

$$\mathbf{K}(t) = \mathbf{Q}_u(t)^{-1}\mathbf{B}^{\mathrm{T}}\mathbf{S}(t), \tag{4.4}$$

where $\mathbf{K}(t)$ is the optimally determined time-varying feedback gain, and $\mathbf{S}(t)$ is defined by the matrix Riccati equation

$$\dot{\mathbf{S}} = -\mathbf{S}\mathbf{A} - \mathbf{A}^{\mathrm{T}}\mathbf{S} + \mathbf{S}\mathbf{B}\mathbf{Q}_u^{-1}\mathbf{B}^{\mathrm{T}}\mathbf{S} - \mathbf{Q}_u. \tag{4.5}$$

Equation (4.5) can be integrated backward from the terminal time $\mathbf{t}_f$ to the initial time $\mathbf{t}_0$ to solve for $\mathbf{S}(t)$. Once $\mathbf{S}(t)$ has been found, the continuous control law and time-varying feedback gains can be calculated.

There are two characteristics of the terminal-controller solution that are advantageous in terms of trajectory generation:

- First, because the terminal time is the only slew parameter on which the solution depends, it is not necessary to redesign the controller for every set of initial and final slew configurations. Rather, a redesign is needed only for slews of different final times.

- Second, because the terminal-controller solution is a backward sweep and does not involve iteration, computation of the solution demands minimal processor time. This computationally efficient solution is a result of the soft terminal constraints on the main arm enabled by the redundancy of the mini-manipulator.

Design Strategy   There are a number of terminal-controller-design strategies that can be adopted. One approach involves designing at the beginning of the slew a new set of terminal-controller gains for each new terminal time. This approach results in a computational delay prior to carrying out the slew to perform the backward sweep. An alternative approach adopted in this research computes ahead of time and stores the controller gains for the repositioning times of interest. As a result, no subsequent off-line computations are required, and no delay is experienced at the beginning of the slew.

4.2.2   Benefits

The benefits of this approach stem from the fact that the trajectory generation is based on a terminal-controller design. Specifically,

- For a given performance index, the terminal controller is designed to reposition optimally the plant model. Thus, this trajectory-generation approach provides the plant with an optimal trajectory for the point-to-point repositioning.

- This approach exploits the redundancy introduced by the mini-manipulator. This idea is incorporated into the trajectory generation in the form of *soft* terminal constraints in the terminal controller design. The soft terminal constraints, rather than hard constraints, allow for the straightforward, computationally efficient terminal-controller solution.

- The slew time is the only slew-dependent parameter in the terminal-controller design. As a result, for repositionings of the same slew time, no additional precomputations are required.

4.2.3   Trajectory-Generation Requirements

This trajectory-generation approach offers benefits in terms of performance, and implementation and design simplicity. However, along with these advantages come three requirements of the resulting trajectory to achieve acceptable performance. First, as described in Chapter 1, the system will be in a regulator mode after the final time t_f. Consequently, after t_f, the desired state provided by the trajectory generator must correspond to the desired tip position. Second, at $t = t_f$ a control-mode transition occurs from sending both feedforward and feedback inputs to the plant, to feedback alone. The terminal controller must be designed

so that this transition is smooth. Finally, the design of the terminal controller is based on a model that is accurate over a limited frequency range. Therefore, the terminal-controller design must be robust to unmodelled dynamics.

Desired State After t_f

The terminal controller is designed to bring the plant model close to the reference commands by the final time. Consequently, the model state will not match exactly the reference state at $t = t_f$. Since the main arm should be regulated to the reference commands for $t > t_f$, it is necessary for the model state to correspond to the reference commands once the repositioning is complete.

The approach adopted to address this issue involves regulating the model state to the reference state for $t > t_f$. At $t = t_f$, a constant-gain regulator regulates the model state to the reference state, although the output of this controller is not sent to the actual plant. To ensure that the response of the model is smooth, the constant-gain controller is designed to be frequency limited to not excite high-frequency dynamics in the model. [3]

Smooth Transition at $t = t_f$

As described in Chapter 1, the solution framework developed in this research sums the feedforward-control input from the trajectory generator, $\mathbf{u}_f$, and the feedback-control input, $\mathbf{u}_a$, to force the plant to follow the desired plant state in the presence of disturbances and other unmodelled effects. At $t = t_f$, the control input to the plant switches from the sum of $\mathbf{u}_f$ and $\mathbf{u}_a$ to just $\mathbf{u}_a$. If the final value of the feedforward input $\mathbf{u}_f(t_f)$ is non-zero, there will be a discontinuity in the control sent to the plant. This discontinuity, if large, will result in a non-smooth control-mode transition. Consequently, an essentially bumpless control-mode transfer requires that $\mathbf{u}_f(t_f) \approx 0$.

Designing a terminal controller such that $\mathbf{u}_f(t_f) \approx 0$ can be achieved by time weighting the terminal-controller cost function. Specifically, by weighting heavily the amount of control effort used near the end of the slew, the output of the terminal controller will be small near the final time. This involves selecting $\mathbf{Q}_u(t)$ to be large for values of t close to $t = t_f$.

In addition to enabling a smooth transition at the end of the slew, time weighting the terminal-controller cost function is consistent with, and helps achieve, the first research task

---

[3]Chapter 5 provides details on designing a frequency-shaped regulator.

described in Chapter 1: to develop a main-arm control approach for positioning quickly the mini-manipulator within the desired workspace. Time weighting the cost function causes the terminal controller to perform most of the trajectory well before the final time, while the "cost" of control is low. As a result, the main arm transports the mini-manipulator to the desired target area faster.

Robustness to High-Frequency Unmodelled Dynamics

For flexible manipulators with unmodelled high-frequency modes, it is desirable to shape the frequency content of the trajectories to not excite unmodelled lightly-damped flexible modes. This can be achieved through a frequency-shaped design (described for the standard LQG design in Chapter 5) which corresponds to introducing "virtual actuator dynamics" or actuator prefilters [47].

Incorporating actuator prefilters into the terminal-controller design and implementation attenuates high-frequency inputs sent to the plant. The prefilter implementation is shown in Figure 4.4. Implementation of the actuator prefilters must be accounted for in the
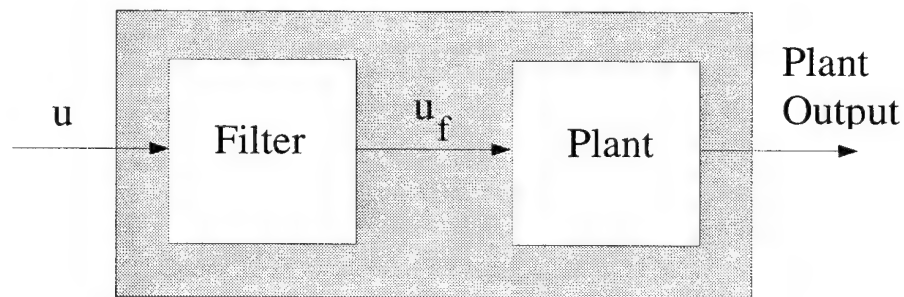
Figure 4.4: **Actuator Prefiltering**

Incorporating actuator prefilters into the terminal-controller design provides a method for achieving a frequency-shaped design. Actuator prefilters filter the control input to attenuate high-frequency inputs that would excite high-frequency unmodelled modes of the plant.

terminal-controller design. This is done by augmenting the plant state with the prefilter state, $\mathbf{x}_f$. Specifically, the performance index of Equation (4.2) must be modified to

$$\mathbf{J}_s = \frac{1}{2}(\mathbf{x}_s{}^T\mathbf{S}_{f_s}\mathbf{x}_s)_{t=t_f} + \frac{1}{2}\int_{t_0}^{t_f}[\mathbf{x}_s{}^T\mathbf{Q}_{x_s}(t)\mathbf{x}_s + \mathbf{u}^T\mathbf{Q}_{u_s}(t)\mathbf{u}]dt \qquad (4.6)$$

where $\mathbf{x}_s$ is defined as

$$\mathbf{x}_s = \begin{bmatrix} \mathbf{x} \\ \mathbf{x}_f \end{bmatrix} \tag{4.7}$$

and $\mathbf{S}_{f_s}$, $\mathbf{Q}_{x_s}(t)$, and $\mathbf{Q}_{u_s}(t)$ are weighting matrices for the augmented system defined by $\mathbf{x}_s$. The actuator prefilter state is defined by the filter state-space model

$$\dot{\mathbf{x}}_f = \mathbf{A}_f \mathbf{x}_f + \mathbf{B}_f \mathbf{u} \tag{4.8}$$

$$\mathbf{u}_f = \mathbf{C}_f \mathbf{x}_f + \mathbf{D}_f \mathbf{u} \tag{4.9}$$

where the output of the filter, $\mathbf{u}_f$, is the input to the physical plant. The terminal-controller design involves minimizing Equation (4.6) subject to the constraints

$$\dot{\mathbf{x}}_s = \mathbf{A}_s \mathbf{x}_s + \mathbf{B}_s \mathbf{u} \tag{4.10}$$

where

$$\mathbf{A}_s = \begin{bmatrix} \mathbf{A} & \mathbf{B}\mathbf{C}_f \\ 0 & \mathbf{A}_f \end{bmatrix} \tag{4.11}$$

$$\mathbf{B}_s = \begin{bmatrix} \mathbf{B}\mathbf{D}_f \\ \mathbf{B}_f \end{bmatrix}. \tag{4.12}$$

The resulting terminal controller is of the form

$$\mathbf{u}(t) = -\mathbf{K}_s(t)\mathbf{x}_s(t) \tag{4.13}$$

where

$$\mathbf{K}_s(t) = \begin{bmatrix} \mathbf{K}(t) & \mathbf{K}_f(t) \end{bmatrix} \tag{4.14}$$

and $\mathbf{K}_f(t)$ is a feedback gain on the prefilter state.

Equation (4.14) indicates that implementation of the frequency-shaped terminal-controller design includes a feedback term on the prefilter state. Figure 4.5 illustrates this implementation.

4.2.4   Design Approach

Designing a terminal controller requires selecting appropriately the weighting matrices $\mathbf{Q}_x(t)$, $\mathbf{Q}_u(t)$, and $\mathbf{S}_f$ to achieve desired performance most closely. For a system with n
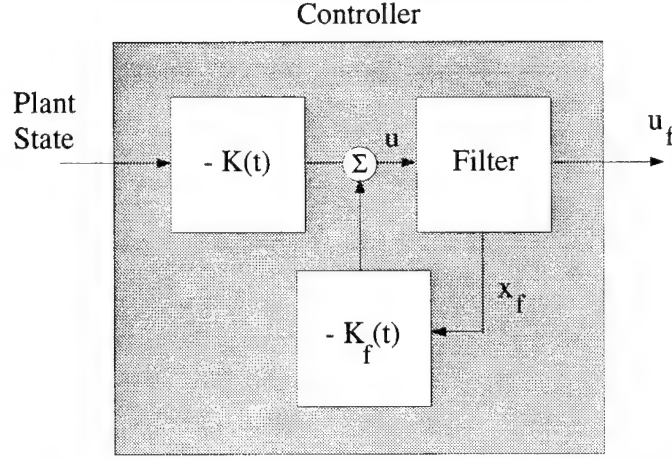
Figure 4.5: **Frequency-Shaped Terminal-Controller Implementation**

Implementing the frequency-shaped terminal controller requires filtering **u** *to generate the actual control input* **u**$_f$, *as well as including an additional feedback term based on the prefilter state.*

states and n_i inputs, specifying the weighting matrices requires selecting n^2 elements of $\mathbf{Q}_x(t)$ and n_i^2 elements of $\mathbf{Q}_u(t)$ for $0 \leq t \leq t_f$, and the n^2 elements of $\mathbf{S}_f$. For a final time t_f and a sample period T_s, $\mathbf{Q}_u(t)$ and $\mathbf{Q}_x(t)$ must be specified for $\frac{t_f}{T_s}$ time steps.

Although $\mathbf{Q}_u(t)$ must be varied with time to meet the trajectory requirements, selection of the weighting matrices can be simplified by choosing $\mathbf{Q}_x(t)$ to be constant for $0 \leq t \leq t_f$. In addition, the selection can be simplified further by regulating the outputs in a coordinated fashion. If the outputs to be controlled, $\mathbf{y}_c \in \mathbb{R}^{n_o}$, can be expressed as

$$\mathbf{y}_c = \mathbf{C}_c\mathbf{x}, \tag{4.15}$$

then the weighting matrices can be selected as

$$\mathbf{S}_f = \mathbf{C}_c^{\mathrm{T}}\mathbf{W}_s\mathbf{C}_c \tag{4.16}$$

$$\mathbf{Q}_x = \mathbf{C}_c^{\mathrm{T}}\mathbf{W}_x\mathbf{C}_c \tag{4.17}$$

$$\mathbf{Q}_u(t) = \rho(t)\mathbf{W}_u \tag{4.18}$$

where $\mathbf{W}_s \in \mathbb{R}^{n_o \times n_o}$ and $\mathbf{W}_x \in \mathbb{R}^{n_o \times n_o}$ are diagonal matrices that weight the terminal and intermediate values of the controlled outputs, $\mathbf{W}_u \in \mathbb{R}^{n_i \times n_i}$ is a constant diagonal matrix, and $\rho(t)$ is a scalar that varies the weighting on the control input $\mathbf{Q}_u$ as a function of time.

Selecting the weighting matrices in this way reduces the design to choosing n_o parameters for both $\mathbf{W}_s$ and $\mathbf{W}_x$, n_i elements of $\mathbf{W}_u$, and the scalar function $\rho(t)$.

The corresponding frequency-limited trajectories can be found by augmenting the model system and output matrices accordingly, and leaving the design parameters unchanged such that

$$\mathbf{S}_{f_s} = \mathbf{C}_s{}^{\mathrm{T}}\mathbf{W}_s\mathbf{C}_s \tag{4.19}$$

$$\mathbf{Q}_{x_s} = \mathbf{C}_s{}^{\mathrm{T}}\mathbf{W}_x\mathbf{C}_s \tag{4.20}$$

$$\mathbf{Q}_{u_s}(t) = \rho(t)\mathbf{W}_u \tag{4.21}$$

where

$$\mathbf{C}_s = \left[\begin{array}{cc} \mathbf{C}_c & \mathbf{0}_{n_o \times (\sum_{i=1}^{n_i} n_{f_i})} \end{array}\right] \tag{4.22}$$

and n_{f_i} corresponds to the order of the prefilter for the ith actuator.

4.3   Design Example: The Flexible Main Arm

The implementation approach adopted in this research is to design and store terminal-controller feedback gains for various values of t_f so that the user can simply select one of the predetermined final times for each repositioning. In this way, once the designs are complete, no additional off-line precomputations are required. This section illustrates the terminal-controller design process for the experimental main arm for a two-second repositioning, and then presents example trajectories for other final times.

4.3.1   Terminal-Controller Design for $t_f = 2$ Seconds

Using the linear model developed in Chapter 3 of the main arm for a ninety degree nominal elbow angle, the controlled outputs $\mathbf{y}_c$, defined in Figure 4.6, are given by
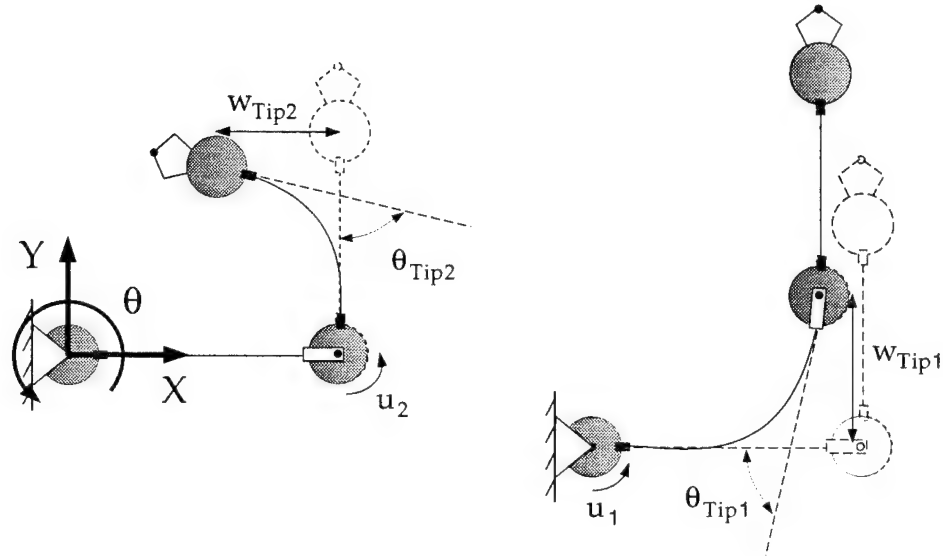
Figure 4.6: **Controlled Outputs**

This figure illustrates the controlled outputs of the manipulator. w_{tipi} and θ_{tipi} represent the lateral deflection and rotation of the tip of link i. The inertial coordinate frame X, Y, Θ is located at the shoulder joint and fixed in inertial space. Also shown are the shoulder and elbow motor inputs u_1 and u_2.

$$
\mathbf{y}_c = \begin{bmatrix} w_{tip2} \\ w_{tip1} \\ \theta_{tip2} \\ \theta_{tip1} \\ \dot{w}_{tip2} \\ \dot{w}_{tip1} \\ \dot{\theta}_{tip2} \\ \dot{\theta}_{tip1} \end{bmatrix} = \mathbf{C}_c \mathbf{x} \tag{4.23}
$$

where w_{tipi} and θ_{tipi} represent the lateral deflection and rotation of the tip of link i. The inertial coordinate frame X, Y, Θ is located at the shoulder joint and fixed in inertial space.

The design parameters were initially chosen as

$$
\mathbf{W}_s = 1500 \times \mathbf{I}_8 \tag{4.24}
$$

$$
\mathbf{W}_x = \mathbf{I}_8 \tag{4.25}
$$

$$
\mathbf{W}_u = \mathbf{I}_2 \tag{4.26}
$$

$$\rho(t) \quad = \quad 1 \tag{4.27}$$

where $\mathbf{I}_j$ is the $j \times j$ identity matrix. Physically, these design parameters weight heavily the terminal error of the controlled outputs to insure that the main arm brings the mini-manipulator close to the desired target very quickly. The corresponding feedback gains are shown in Figure 4.7.   In general, the gains are relatively small at the beginning of the
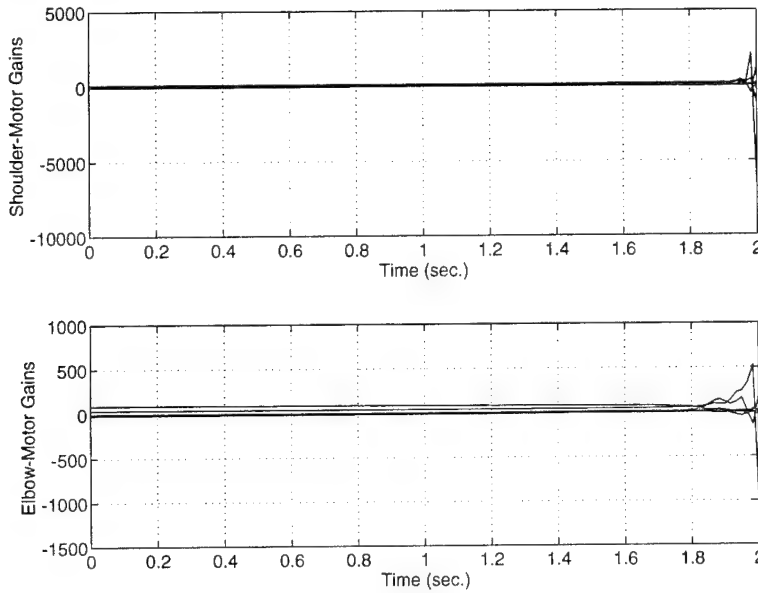
Figure 4.7: **Initial Terminal-Controller Gains**

This figure shows the terminal-controller gains as a function of time. The gains tend to increase near the final time to make the terminal errors small.

slew, and then increase near the end of the slew to make the terminal errors small quickly. Rather than plot all elements of the desired state history for a repositioning in which the tip is commanded to move 10 cm in both the X and Y directions, the corresponding desired tip trajectory and the corresponding feedforward control are shown in Figure 4.8.

Although the tip trajectory is smooth, this design is unacceptable because of the high-frequency content of the torque profiles at the beginning and end of the slews. It is desirable to smooth the torque profiles so that the feedforward input does not excite unmodelled lightly-damped high-frequency modes in the arm.

To limit the frequency content of the feedforward input, the model is augmented with actuator prefilters as described in the previous section. The prefilters for both the shoulder
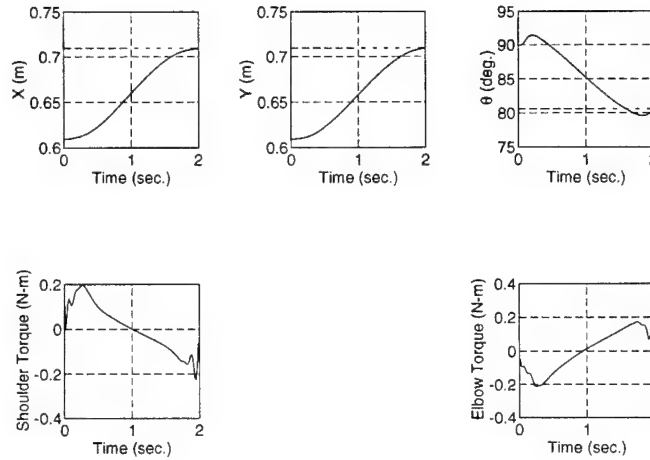
Figure 4.8: **Initial Trajectory**

This figure displays the desired tip response that corresponds to the generated desired state history, as well as the control inputs that are generated by the feedback gains of Figure 4.7. The dashed lines in the tip response indicate the desired terminal values. The high-frequency content at the beginning and end of the torque profiles is undesirable when lightly-damped unmodelled modes are present. Consequently, the trajectory displayed in this figure motivates the need for a frequency-shaped design.

and elbow motors are fifth-order Butterworth filters with a 5 Hz cut-off frequency. The resulting frequency-limited trajectory is given in Figure 4.9.

To achieve a smooth control-mode transfer, it is necessary to modify the design so that $\mathbf{u}(t_f) \approx 0$. Consequently, it is desirable to select a scalar function $\rho(t)$ such that the weighting on the control $\mathbf{Q}_u(t)$ becomes larger as t approaches t_f. Figure 4.10 shows the $\rho(t)$ that was selected in this design. The physical interpretation of this function is that the cost of control is low and constant for $t < 0.8t_f$, and then becomes increasingly high for $t \geq 0.8t_f$. For this design, $\rho(t) = 1$ for $t < 0.8t_f$, and for $t \geq 0.8t_f$

$$\rho(t) = \left(\frac{t}{T_s} - 0.8\frac{t_f}{T_s} + 1\right)^2 \tag{4.28}$$

where $T_s = \frac{1}{60} sec.$
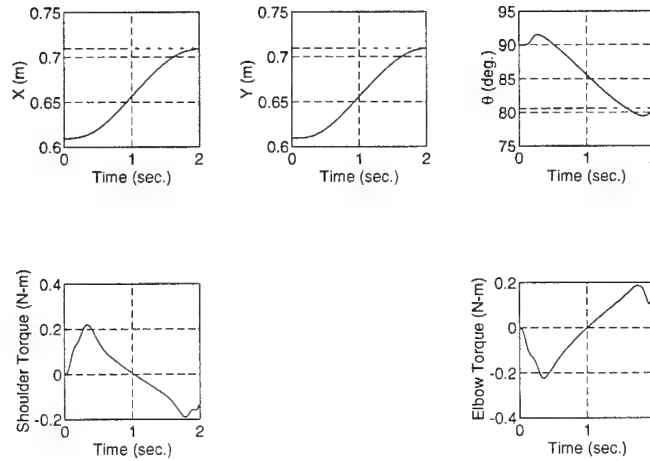
Figure 4.9: **Frequency-Shaped Trajectory**

This figure shows the feedforward-control input and the desired tip response for the frequency-shaped design. The torque profiles are smoother than the profiles in Figure 4.8 due to the introduction of actuator prefilters.

By time-weighting the cost function, the cost of control is very high near the end of the slew. The controller, therefore, attempts to effect most of the motion early when control is cheap, and thereby needs to make only fine adjustments during the last part of the slew when control is expensive.

The final terminal-controller trajectory for a two-second terminal time is given in Figure 4.11. The symmetric torque profiles in Figure 4.11 correspond to a "near-minimum-time" response. The actuators "push" hard during the first half of the slew, and "pull" equally hard during the second half of the slew to bring the system to rest.

4.3.2   Additional Designs

For the same weighting matrices, terminal controllers were designed for slew times of 1.5, 2.5, and 3 seconds by simply changing the final time in the backward sweep solution. The corresponding trajectories are displayed in Figures 4.12 through 4.14 for a specific
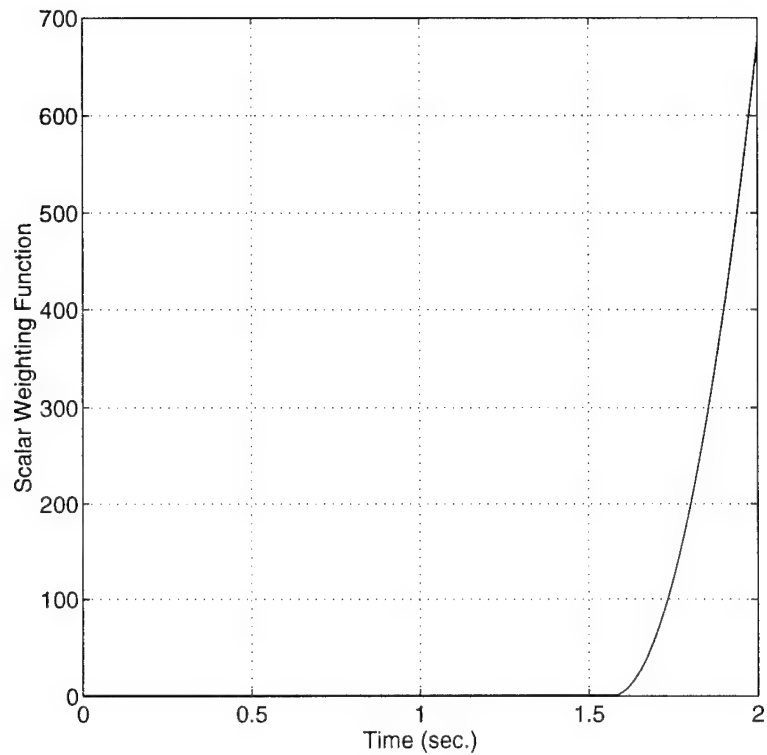
Figure 4.10: **Scalar Weighting Function** $\rho(t)$

This figure shows the scalar function that makes the cost of control a function of time. This particular function will penalize increasingly the control after $t = 0.8t_f$ to force $\mathbf{u}(t_f) \approx 0$.

repositioning in which the manipulator tip is commanded to move 10 cm in both the X and Y directions.
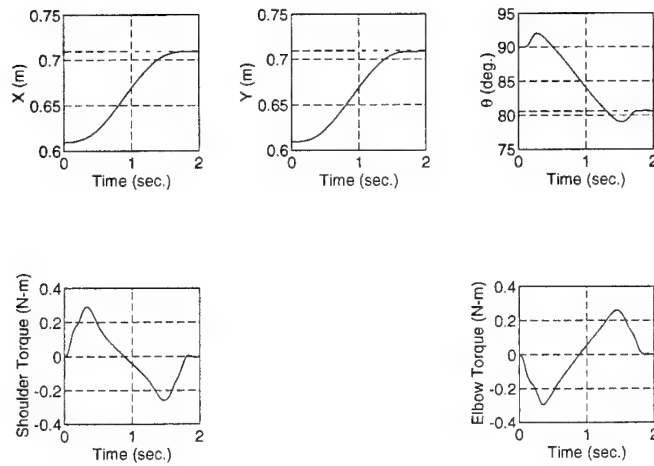
Figure 4.11: **Trajectory for** $t_f = 2.0$ **Seconds**
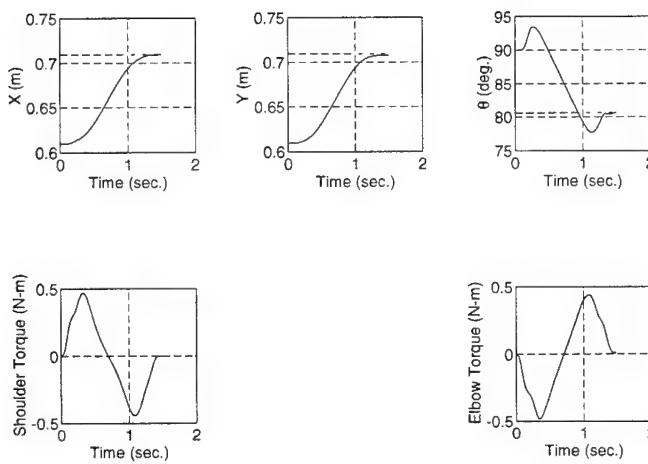
Figure 4.12: **Trajectory for** $t_f = 1.5$ **Seconds**
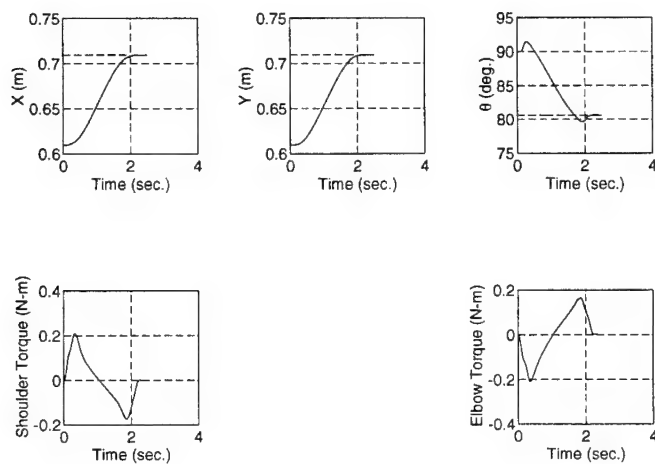
Figure 4.13: **Trajectory for** $t_f = 2.5$ **Seconds**
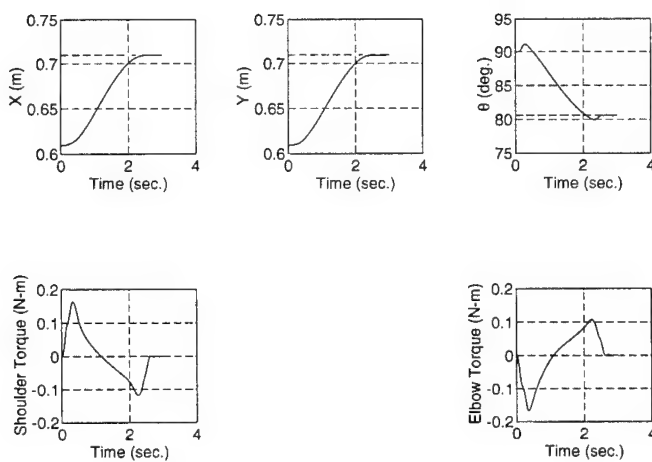
Figure 4.14: **Trajectory for** $t_f = 3.0$ **Seconds**

4.4   Summary

This chapter described a new trajectory-generation approach that computes an optimal state history and corresponding feedforward-control input for point-to-point repositionings of multi-link flexible manipulators with a specified final time. By formulating the repositioning problem as a terminal-control problem, this approach exploits two characteristics of the point-to-point repositioning problem addressed in this research: (1) the soft-terminal-control approach enabled by the redundancy introduced by the mini-manipulator, and (2) the opportunity to follow an optimal path during the repositioning since only the final tip position is specified.

This approach is based on a model-following implementation of a terminal controller that regulates in real time a plant model to the reference commands. The output of the terminal controller is sent to the plant as a feedforward-control input. The corresponding response of the plant model represents the desired state history for the plant to follow during the repositioning.

A terminal-controller design for the main arm was used to illustrate the design process. The resulting feedforward component of the control system will be used – together with the feedback component – in Chapter 6 to generate – and execute – optimal trajectories for point-to-point repositionings of the experimental system.

Chapter 5

Feedback Control

This chapter describes the control approach developed in this research for multi-link flexible systems, and presents an application of this approach to the experimental apparatus. Figure 5.1 illustrates how the resulting feedback-control component fits into the control-system framework described in Chapter 1. Feedback control combines with the feedforward input
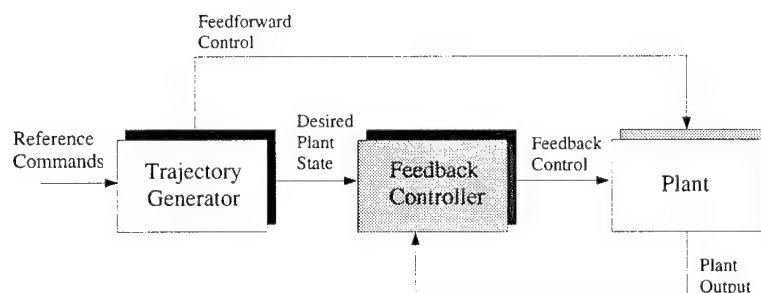
Figure 5.1: **Control Framework**

Chapter 4 presented the trajectory-generation component of the solution framework. This chapter presents the feedback-control approach developed in this research. The feedback controller generates a control input that augments the feedforward input to regulate the plant to the desired plant-state history in the presence of disturbances and unmodelled effects.

to regulate the plant to the desired plant-state history in the presence of disturbances and unmodelled effects.

The control approach developed in this dissertation enables the development of high-performance controllers for *predominantly* one-way coupled system to be partitioned into

73

sequential subsystem designs. This sequential process exploits the one-way coupling that characterizes the system within the frequency range of interest for control. Because the one-way coupling assumption is inaccurate outside of this frequency range, the subsystem controllers are designed to be robust to this model uncertainty. As a result, this approach enables design for *high-performance* control of complex systems to be partitioned into design steps for smaller, more tractable subsets.

5.1   Background

Eric Schmitz demonstrated, on a single-link flexible manipulator, a factor of four improvement in control bandwidth over conventional joint-based control through a linear-quadratic-gaussian (LQG) control strategy that incorporated end-point measurements ([4] and [6]). Similar performance improvements were demonstrated by Celia Oakley who achieved high-performance end-point control of a two-link flexible manipulator [5]. This previous work generated two important findings:

- First, end-point feedback is critical to achieving high-performance control of flexible manipulators.

- Second, LQG theory provides a framework for developing control systems that incorporate effectively end-point feedback.

Based on the results of this previous work, an LQG framework incorporating end-point feedback was chosen as the *basis* of the control approach developed in this research for predominantly one-way coupled systems.

Systems that are *predominantly* one-way coupled can be modelled as one-way coupled within the frequency range of interest for control. Specifically, within this frequency range, the equations of motion for a predominantly one-way coupled system made up of two subsystems represented by $\mathbf{x}_1(t)$ and $\mathbf{x}_2(t)$ are of the form

$$\left[\begin{array}{c} \dot{\mathbf{x}}_1(t) \\ \dot{\mathbf{x}}_2(t) \end{array} \right] = \left[\begin{array}{cc} \mathbf{A}_{11} & \mathbf{A}_{12} \\ \mathbf{0} & \mathbf{A}_{22} \end{array} \right] \left[\begin{array}{c} \mathbf{x}_1(t) \\ \mathbf{x}_2(t) \end{array} \right] + \left[\begin{array}{cc} \mathbf{B}_{11} & \mathbf{B}_{12} \\ \mathbf{0} & \mathbf{B}_{22} \end{array} \right] \left[\begin{array}{c} \mathbf{u}_1(t) \\ \mathbf{u}_2(t) \end{array} \right]. \tag{5.1}$$

The subsystems of Equation (5.1) are one-way state and input coupled since $\mathbf{x}_2(t)$ is independent of both $\mathbf{x}_1(t)$ and $\mathbf{u}_1(t)$. Because Equation (5.1) accurately represents the system

within the frequency range of interest, it is a suitable model for control design. However, a model of the plant that is accurate for all frequencies is given by

$$
\begin{bmatrix} \dot{\mathbf{x}}_1(t) \\ \dot{\mathbf{x}}_2(t) \end{bmatrix} = \begin{bmatrix} \tilde{\mathbf{A}}_{11} & \tilde{\mathbf{A}}_{12} \\ \tilde{\mathbf{A}}_{21} & \tilde{\mathbf{A}}_{22} \end{bmatrix} \begin{bmatrix} \mathbf{x}_1(t) \\ \mathbf{x}_2(t) \end{bmatrix} + \begin{bmatrix} \tilde{\mathbf{B}}_{11} & \tilde{\mathbf{B}}_{12} \\ \tilde{\mathbf{B}}_{21} & \tilde{\mathbf{B}}_{22} \end{bmatrix} \begin{bmatrix} \mathbf{u}_1(t) \\ \mathbf{u}_2(t) \end{bmatrix}. \tag{5.2}
$$

Equation (5.2) subsumes Equation (5.1) in that the models are identical within the frequency range of interest, and deviate outside of this frequency range. As a result, control design based on Equation (5.1) must be made robust to model uncertainty for the frequency ranges where the model is inaccurate.

5.2 Control Approach

The control approach developed here consists of two steps:

- First, based on a model of the form of Equation (5.1), design sequentially LQG sub-system controllers that yield desired performance.

- Second, make the subsystem designs robust to model uncertainty outside the frequency range for which Equation (5.1) is accurate.

5.2.1 Sequential Design Process

The initial subsystem designs are performed sequentially based on a model of the form

$$
\begin{bmatrix} \dot{\mathbf{x}}_1(t) \\ \dot{\mathbf{x}}_2(t) \end{bmatrix} = \begin{bmatrix} \mathbf{A}_{11} & \mathbf{A}_{12} \\ \mathbf{0} & \mathbf{A}_{22} \end{bmatrix} \begin{bmatrix} \mathbf{x}_1(t) \\ \mathbf{x}_2(t) \end{bmatrix} + \begin{bmatrix} \mathbf{B}_{11} & \mathbf{B}_{12} \\ \mathbf{0} & \mathbf{B}_{22} \end{bmatrix} \begin{bmatrix} \mathbf{u}_1(t) \\ \mathbf{u}_2(t) \end{bmatrix}. \tag{5.3}
$$

Exploiting the fact that the coupling between the subsystems is one way and that the control $\mathbf{u}_1(t)$ does not affect $\mathbf{x}_2(t)$, an LQG controller is designed for $\mathbf{x}_2(t)$ based solely on the equation

$$
\dot{\mathbf{x}}_2(t) = \mathbf{A}_{22}\mathbf{x}_2(t) + \mathbf{B}_{22}\mathbf{u}_2(t). \tag{5.4}
$$

Specifically, assuming for simplicity that full knowledge of $\mathbf{x}_1(t)$ and $\mathbf{x}_2(t)$ is available, a control law for $\mathbf{u}_2(t)$ is designed of the form

$$
\mathbf{u}_2(t) = -\mathbf{K}_2\mathbf{x}_2(t). \tag{5.5}
$$

Substituting Equation (5.5) into Equation (5.3) results in the following system equations

$$
\begin{bmatrix} \dot{\mathbf{x}}_1(t) \\ \dot{\mathbf{x}}_2(t) \end{bmatrix} = \begin{bmatrix} \mathbf{A}_{11} & \mathbf{A}_{12} - \mathbf{B}_{12}\mathbf{K}_2 \\ 0 & \mathbf{A}_{22} - \mathbf{B}_{22}\mathbf{K}_2 \end{bmatrix} \begin{bmatrix} \mathbf{x}_1(t) \\ \mathbf{x}_2(t) \end{bmatrix} + \begin{bmatrix} \mathbf{B}_{11} \\ 0 \end{bmatrix} \mathbf{u}_1(t). \tag{5.6}
$$

Equation (5.6) represents a system containing two subsystems that are one-way coupled with a control input $\mathbf{u}_1(t)$.

Next, based on Equation (5.6), a control law for $\mathbf{u}_1(t)$ is designed of the form

$$
\mathbf{u}_1(t) = -\mathbf{K}_1\mathbf{x}(t) \tag{5.7}
$$

where

$$
\mathbf{x}(t) = \begin{bmatrix} \mathbf{x}_1(t) \\ \mathbf{x}_2(t) \end{bmatrix} \tag{5.8}
$$

and

$$
\mathbf{K}_1 = \begin{bmatrix} \mathbf{K}_{11} & \mathbf{K}_{12} \end{bmatrix}. \tag{5.9}
$$

Equations (5.5) and (5.7) together represent a total-system controller for the system of Equation (5.3). The corresponding closed loop system is given by

$$
\begin{bmatrix} \dot{\mathbf{x}}_1(t) \\ \dot{\mathbf{x}}_2(t) \end{bmatrix} = \begin{bmatrix} \mathbf{A}_{11} - \mathbf{B}_{11}\mathbf{K}_{11} & \mathbf{A}_{12} - \mathbf{B}_{12}\mathbf{K}_2 - \mathbf{B}_{11}\mathbf{K}_{12} \\ 0 & \mathbf{A}_{22} - \mathbf{B}_{22}\mathbf{K}_2 \end{bmatrix} \begin{bmatrix} \mathbf{x}_1(t) \\ \mathbf{x}_2(t) \end{bmatrix}. \tag{5.10}
$$

5.2.2   Subsystem Control-Design Approach

For the resulting total-system controller to meet desired system performance objectives, the subsystem controllers must meet corresponding subsystem performance objectives. An additional requirement is that the subsystem designs be robust to model uncertainty. This section illustrates the delegation of subsystem requirements based on total-system specifications, the initial subsystem control designs to meet these requirements, and then the approach to develop the corresponding robust subsystem controllers.

Subsystem Performance Requirements

One method of specifying control-system performance requirements for flexible manipulators is to establish minimum damping ratios and frequencies for the system modes. These

specifications can then be expressed in terms of *regions* of the s plane in which the LQG design must place the closed-loop roots.

The one-way coupling characteristic of Equation (5.1) enables system performance objectives, expressed in terms of closed-loop-root regions, to be partitioned into subsystem performance requirements. The closed-loop roots λ_c are the eigenvalues of the closed-loop system matrix

$$\lambda_c = eig \left(\begin{bmatrix} \mathbf{A}_{11} - \mathbf{B}_{11}\mathbf{K}_{11} & \mathbf{A}_{12} - \mathbf{B}_{12}\mathbf{K}_2 - \mathbf{B}_{11}\mathbf{K}_{12} \\ 0 & \mathbf{A}_{22} - \mathbf{B}_{22}\mathbf{K}_2 \end{bmatrix} \right). \tag{5.11}$$

Furthermore, because of the matrix of zeros in the lower left corner, λ_c can also be expressed as

$$\lambda_c = \{\lambda_1, \lambda_2\} \tag{5.12}$$

where

$$\lambda_1 = eig \left(\mathbf{A}_{11} - \mathbf{B}_{11}\mathbf{K}_{11} \right) \tag{5.13}$$

and

$$\lambda_2 = eig \left(\mathbf{A}_{22} - \mathbf{B}_{22}\mathbf{K}_2 \right). \tag{5.14}$$

Physically, λ_i represents the closed-loop roots of subsystem i. Consequently, designing the subsystem controllers so that the subsystem eigenvalues are within the desired regions implies that closed-loop system requirements will be met.

Initial Subsystem Control Design

The ith subsystem control design is based on the equation

$$\dot{\mathbf{x}}_i(t) = \mathbf{A}_i\mathbf{x}_i(t) + \mathbf{B}_i\mathbf{u}_i(t). \tag{5.15}$$

Assuming full state feedback, the LQG subsystem design involves formulating a linear-quadratic cost function

$$\mathbf{J}_i = \frac{1}{2} \int_0^\infty [\mathbf{x}_i(t)^\mathrm{T}\mathbf{Q}_{x_i}\mathbf{x}_i(t) + \mathbf{u}_i(t)^\mathrm{T}\mathbf{Q}_{u_i}\mathbf{u}_i(t)]dt, \tag{5.16}$$

and then minimizing this cost function with respect to the control input $\mathbf{u}_i$. $\mathbf{Q}_{x_i}$ and $\mathbf{Q}_{u_i}$ are weighting matrices that enable a trade off between performance and actuator effort.

The resulting controller is a gain vector $\mathbf{K}_i$ [46], and the corresponding control law is given by

$$\mathbf{u}_i(t) \quad = \quad -\mathbf{K}_i\mathbf{x}_i(t). \tag{5.17}$$

The subsystem control design involves varying the weighting matrices $\mathbf{Q}_{x_i}$ and $\mathbf{Q}_{u_i}$ until a gain matrix $\mathbf{K}_i$ results that places the subsystem eigenvalues λ_i within the desired region.

It is desirable to design a controller that regulates the subsystem outputs in a coordinated fashion. Given the controlled outputs of subsystem i, $\mathbf{y}_{c_i} \in \mathbb{R}^{n_{oi}}$, expressed as

$$\mathbf{y}_{c_i} = \mathbf{C}_{c_i}\mathbf{x}_i, \tag{5.18}$$

the weighting matrix $\mathbf{Q}_{x_i}$ is selected as

$$\mathbf{Q}_{x_i} \quad = \quad \mathbf{C}_{c_i}{}^{\mathrm{T}}\mathbf{W}_{x_i}\mathbf{C}_{c_i} \tag{5.19}$$

where $\mathbf{W}_{x_i} \in \mathbb{R}^{n_{oi} \times n_{oi}}$ is a diagonal matrix that weights directly the controlled outputs.

Robust Subsystem Control Design

The LQG subsystem controllers are designed to meet performance criteria (i.e. subsystem root locations) within the frequency range for which the model is accurate. Because the model is inaccurate outside of this range, a mechanism is needed to maintain performance in the frequency range of interest and provide robustness to model uncertainty outside of this range.

This can be done following the techniques of Gupta [47] (also described in [9]). The standard subsystem LQG cost function given in Equation (5.16), can be transformed to the frequency domain using Parseval's Theorem:

$$J_{i_\omega} \quad .= \quad \int_{-\infty}^{\infty}[\mathbf{x}_i^*(j\omega)\mathbf{Q}_{x_i}(j\omega)\mathbf{x}_i(j\omega) + \mathbf{u}_i^*(j\omega)\mathbf{Q}_{u_i}(j\omega)\mathbf{u}_i(j\omega)]d\omega \tag{5.20}$$

where * implies complex conjugate. By varying $\mathbf{Q}_{x_i}(j\omega)$ and $\mathbf{Q}_{u_i}(j\omega)$ over frequency, the performance of the controller can be made a function of frequency. Since the objective is to vary performance over frequency, it will be sufficient to vary the actuator weighting matrix only resulting in

$$J_{i_\omega} \quad = \quad \int_{-\infty}^{\infty}[\mathbf{x}_i^*(j\omega)\mathbf{Q}_{x_i}\mathbf{x}_i(j\omega) + \mathbf{u}_i^*(j\omega)\mathbf{Q}_{u_i}(j\omega)\mathbf{u}_i(j\omega)]d\omega. \tag{5.21}$$

In order to achieve robust subsystem designs and still meet performance requirements, the strategy is to make control effort very expensive (large $\mathbf{Q}_{u_i}(j\omega)$ and hence little actuator response) at frequencies where the model is inaccurate and to make it cheap (small $\mathbf{Q}_{u_i}(j\omega)$ and hence large actuator response) at frequencies where the model is well characterized.

The actuator weighting matrix, $\mathbf{Q}_{u_i}(j\omega)$, must be positive definite such that

$$\mathbf{Q}_{u_i}(j\omega) = \mathbf{P}_i^*(j\omega)\mathbf{P}_i(j\omega). \tag{5.22}$$

The cost function can then be converted back to the time domain by substituting Equation (5.22) into Equation (5.21)

$$
\begin{aligned}
J_{i_\omega} &= \int_{-\infty}^{\infty} [\mathbf{x}_i^*(j\omega)\mathbf{Q}_{x_i}\mathbf{x}_i(j\omega) + \mathbf{u}_i^*(j\omega)\mathbf{P}_i^*(j\omega)\mathbf{P}_i(j\omega)\mathbf{u}_i(j\omega)]d\omega & \text{(5.23)} \\
&= \int_{-\infty}^{\infty} [\mathbf{x}_i^*(j\omega)\mathbf{Q}_{x_i}\mathbf{x}_i(j\omega) + \tilde{\mathbf{u}}_i^*(j\omega)\tilde{\mathbf{u}}_i(j\omega)]d\omega & \text{(5.24)}
\end{aligned}
$$

where

$$\tilde{\mathbf{u}}_i(j\omega) = \mathbf{P}_i(j\omega)\mathbf{u}_i(j\omega). \tag{5.25}$$

The weighting matrices are no longer a function of frequency, so minimizing the frequency-domain cost function is equivalent to minimizing the time-domain cost function

$$J_{i_\omega} = \int_0^{\infty} [\mathbf{x}_i^{\mathrm{T}}(t)\mathbf{Q}_{x_i}\mathbf{x}_i(t) + \tilde{\mathbf{u}}_i^{\mathrm{T}}(t)\tilde{\mathbf{u}}_i(t)]dt. \tag{5.26}$$

If $\mathbf{P}(j\omega)$ is invertible (if $\mathbf{P}(j\omega)$ is not invertible, see [47] for an alternative implementation), $\tilde{\mathbf{u}}_i$ satisfies

$$\mathbf{u}_i(j\omega) = \mathbf{P}_i^{-1}(j\omega)\tilde{\mathbf{u}}_i(j\omega) \tag{5.27}$$

where the control generated by the control design must be physically filtered to generate the control $\mathbf{u}_i$ that is actually sent to the plant. The frequency-domain problem of Equation (5.21) can now be solved as a time-domain problem of Equation (5.26) by augmenting the plant with the filter $\mathbf{P}_i^{-1}(j\omega)$. The prefilter $\mathbf{P}_i^{-1}(j\omega)$ is defined by the state-space model

$$
\begin{aligned}
\dot{\mathbf{x}}_{f_i} &= \mathbf{A}_{f_i}\mathbf{x}_{f_i} + \mathbf{B}_{f_i}\tilde{\mathbf{u}}_i & \text{(5.28)} \\
\mathbf{u}_i &= \mathbf{C}_{f_i}\mathbf{x}_{f_i} + \mathbf{D}_{f_i}\tilde{\mathbf{u}}_i & \text{(5.29)}
\end{aligned}
$$

where the output of the filter, $\mathbf{u}_i$, is the input to the physical plant. The filter state is defined by $\mathbf{x}_{f_i} \in \mathbb{R}^{n_{f_i}}$. The augmented plant equations that are used in the design are given by

$$\dot{\mathbf{x}}_{s_i} = \mathbf{A}_{s_i}\mathbf{x}_{s_i} + \mathbf{B}_{s_i}\tilde{\mathbf{u}}_i \tag{5.30}$$

where

$$\mathbf{A}_{s_i} \;=\; \begin{bmatrix} \mathbf{A}_i & \mathbf{B}_i\mathbf{C}_{f_i} \\ \mathbf{0} & \mathbf{A}_{f_i} \end{bmatrix} \tag{5.31}$$

$$\mathbf{B}_{s_i} \;=\; \begin{bmatrix} \mathbf{B}_i\mathbf{D}_{f_i} \\ \mathbf{B}_{f_i} \end{bmatrix}. \tag{5.32}$$

A frequency-shaped subsystem controller that maintains the performance of the initial subsystem controller is achieved by solving the standard LQG problem for the augmented plant with $\mathbf{Q}_{u_i}$ equal to identity and

$$\mathbf{Q}_{x_i} \;=\; \mathbf{C}_{s_i}{}^{\mathrm{T}}\mathbf{W}_{x_i}\mathbf{C}_{s_i} \tag{5.33}$$

where

$$\mathbf{C}_{s_i} = \begin{bmatrix} \mathbf{C}_{c_i} & \mathbf{0}_{n_{oi}\times n_{f_i}} \end{bmatrix} \tag{5.34}$$

and $\mathbf{W}_{x_i}$ chosen to be the same as in the initial subsystem design (see Equation (5.19)).

5.2.3   Generalization

This sequential control approach can be extended to predominantly one-way coupled systems with any number of subsystems. Specifically, if a system comprised of n subsystems is described by

$$\begin{bmatrix} \dot{\mathbf{x}}_1(t) \\ \vdots \\ \dot{\mathbf{x}}_n(t) \end{bmatrix} = \begin{bmatrix} \mathbf{A}_{11} & \mathbf{A}_{12} & \cdots & \mathbf{A}_{1(n-1)} & \mathbf{A}_{1n} \\ 0 & \mathbf{A}_{22} & \cdots & \mathbf{A}_{2(n-1)} & \mathbf{A}_{2n} \\ \vdots & \vdots & \ddots & \vdots & \vdots \\ 0 & 0 & \cdots & \mathbf{A}_{(n-1)(n-1)} & \mathbf{A}_{(n-1)n} \\ 0 & 0 & \cdots & 0 & \mathbf{A}_{nn} \end{bmatrix} \begin{bmatrix} \mathbf{x}_1(t) \\ \vdots \\ \mathbf{x}_n(t) \end{bmatrix} +$$

$$\begin{bmatrix} \mathbf{B}_{11} & \mathbf{B}_{12} & \cdots & \mathbf{B}_{1(n-1)} & \mathbf{B}_{1n} \\ 0 & \mathbf{B}_{22} & \cdots & \mathbf{B}_{2(n-1)} & \mathbf{B}_{2n} \\ \vdots & \vdots & \ddots & \vdots & \vdots \\ 0 & 0 & \cdots & \mathbf{B}_{(n-1)(n-1)} & \mathbf{B}_{(n-1)n} \\ 0 & 0 & \cdots & 0 & \mathbf{B}_{nn} \end{bmatrix} \begin{bmatrix} \mathbf{u}_1(t) \\ \vdots \\ \mathbf{u}_n(t) \end{bmatrix}, \tag{5.35}$$

within the frequency range of interest, then a total-system controller can be designed based on n sequential, robust, subsystem designs.

The specific procedure is as follows:

1. Design a robust control law for actuator n of the form

$$\mathbf{u}_n(t) = -\mathbf{K}_n \mathbf{x}_n(t) \tag{5.36}$$

from the equation

$$\dot{\mathbf{x}}_n(t) = \mathbf{A}_{nn} \mathbf{x}_n(t) + \mathbf{B}_{nn} \mathbf{u}_n(t) \tag{5.37}$$

such that the subsystem closed-loop roots λ_n are within the desired region.

2. Incorporate Equation (5.36) into Equation (5.35), and design a robust control law for actuator $n - 1$ based on the equations describing coordinates $\mathbf{x}_n$ and $\mathbf{x}_{n-1}$.

3. Repeat step 2 sequentially until the final control design for actuator 1 based on the equations describing coordinates $\mathbf{x}_1, \mathbf{x}_2, \mathbf{x}_3, \cdots, \mathbf{x}_n$.

5.3 Example: Control Design for the Experimental System

This section presents an application of the control approach described in the last section to develop a controller for the experimental system. Because the mini-manipulator tip dynamics are assumed to be decoupled from the main arm (see Chapter 3), the control design is partitioned into designing independent main-arm and mini-manipulator controllers.

5.3.1 Main-Arm Design

As described in Chapter 3, the main arm is represented accurately as a predominantly one-way coupled system. Consequently, within the frequency range of interest for control, the main-arm dynamics are given by

$$
\begin{bmatrix} \dot{\mathbf{x}}_1(t) \\ \dot{\mathbf{x}}_2(t) \end{bmatrix} = \begin{bmatrix} \mathbf{A}_{11} & \mathbf{A}_{12} \\ \mathbf{0} & \mathbf{A}_{22} \end{bmatrix} \begin{bmatrix} \mathbf{x}_1(t) \\ \mathbf{x}_2(t) \end{bmatrix} + \begin{bmatrix} \mathbf{B}_{11} & \mathbf{B}_{12} \\ \mathbf{0} & \mathbf{B}_{22} \end{bmatrix} \begin{bmatrix} u_1(t) \\ u_2(t) \end{bmatrix} \tag{5.38}
$$

where $u_1(t)$ and $u_2(t)$ are the shoulder and elbow-motor control inputs, and $\mathbf{x}_1(t)$ and $\mathbf{x}_2(t)$ represent the dynamics of the first-link and second-link subsystems. Presented here is an application of the sequential control approach to develop a regulator for the main arm.[1]

---

[1]Because access to all the states of this system is of course not possible, estimation is required. Appendix E details the estimator design for the main arm.

Requirements The dynamic response of the main arm is dominated by two rigid-body modes and the first two flexible modes of the system. Consequently, it is desired to achieve close to .707 damping on the corresponding closed-loop roots, while at the same time pushing the rigid-body poles well beyond the limitations corresponding to joint-based control (i.e. the frequency corresponding to the first cantilever zero). Because of the one-way coupling characteristics, these specifications correspond directly to subsystem performance requirements. Specifically, each subsystem controller is required to achieve close to .707 damping on the first subsystem flexible mode and the rigid-body mode, while at the same time pushing the subsystem rigid-body poles beyond the first cantilever zero of the subsystem.

Control Design for Subsystem 2

Control design for subsystem two is based on the model

$$\dot{\mathbf{x}}_2(t) \quad = \quad \mathbf{A}_{22}\mathbf{x}_{22}(t) + \mathbf{B}_{22}u_2(t). \tag{5.39}$$

The controlled outputs for subsystem two, defined in Figure 5.2, are given by

$$\mathbf{y}_{c_2} = \begin{bmatrix} w_{tip2} \\ \theta_{tip2} \end{bmatrix} = \mathbf{C}_{c_2}\mathbf{x}_2 \tag{5.40}$$

where w_{tip2} and θ_{tip2} represent the lateral deflection and rotation of the tip of the second link. [2]

Initial Design The weighting matrices for the subsystem designs were varied until the requirements on the closed-loop roots were satisfied. The final weighting matrices for the subsystem-two design are defined by

$$\mathbf{Q}_{u_2} \quad = \quad 1 \ (\text{N-m})^{-2} \tag{5.41}$$

$$\mathbf{Q}_{x_2} \quad = \quad \mathbf{C}_{c_2}{}^{\mathrm{T}}\mathbf{W}_{x_2}\mathbf{C}_{c_2} \tag{5.42}$$

with

$$\mathbf{W}_{x_2} \quad = \quad \begin{bmatrix} 125 \ \text{m}^{-2} & 0 \\ 0 & 25 \ \text{rad}^{-2} \end{bmatrix}. \tag{5.43}$$

---

[2]Because the system modes corresponding to the second link closely resemble a pinned-pinned beam, controlling the lateral tip deflection w_{tip2} alone is insufficient. To meet the damping requirements on the first mode of subsystem two, it is also necessary to control the rotation at the tip of link θ_{tip2}.
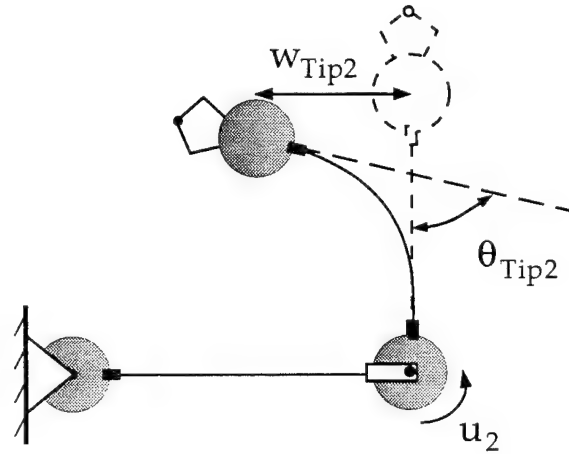
Figure 5.2: **Controlled Outputs of Subsystem 2**

This figure illustrates the controlled outputs of subsystem two. w_{tip2} and θ_{tip2} represent the lateral deflection and rotation of the tip of link 2. Also shown is the elbow-motor input u_2.

The resulting control law is of the form

$$u_2(t) \quad = \quad -\mathbf{K}_2\mathbf{x}_2(t). \tag{5.44}$$

The corresponding closed-loop-root locations for this design are shown in Figure 5.3. This controller meets the damping and frequency requirements on the first flexible mode and the rigid-body mode of subsystem two. The experimental response of this controller, however, is unstable as shown in Figure 5.4. With the manipulator initially at rest, the controlled real system's first unmodelled mode, at approximately 20 Hz, is seen to be unstable. Consequently, the design of the subsystem-two controller needs to be made robust to these unmodelled dynamics.
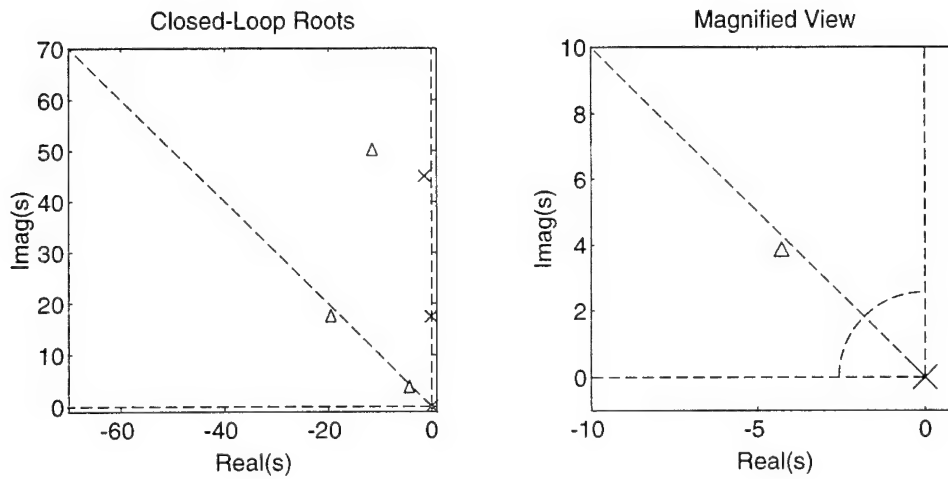
Figure 5.3: **Initial Design for Subsystem 2**

*This figure shows the closed-loop-root locations for the initial control design for subsystem two. The **x**'s represent the open-loop roots, and the △'s represent the closed-loop roots. The diagonal dashed line corresponds to .707 damping. The figure on the right is a magnified view of the figure on the left. The quarter circle corresponds to the first-cantilever-mode natural frequency.*
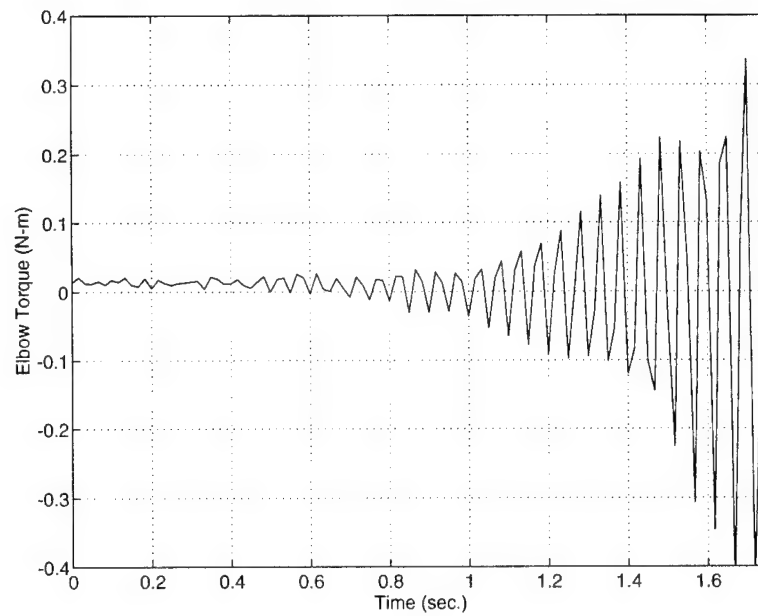
Figure 5.4: **Experimental Response of Initial Design for Subsystem 2**

Shown in the figure is the elbow torque generated by the initial controller for subsystem two. With the manipulator initially at rest, the first unmodelled mode of the controlled system, at approximately 20 Hz, is seen to be unstable.

Robust Design   To make the initial design for subsystem two robust to the unmodelled dynamics, a frequency-shaped design was achieved by implementing a fifth-order Butterworth filter with a 5 Hz cut-off frequency. The corresponding closed-loop roots for this design are given in Figure 5.5.   The figure contains additional open-loop and closed-loop
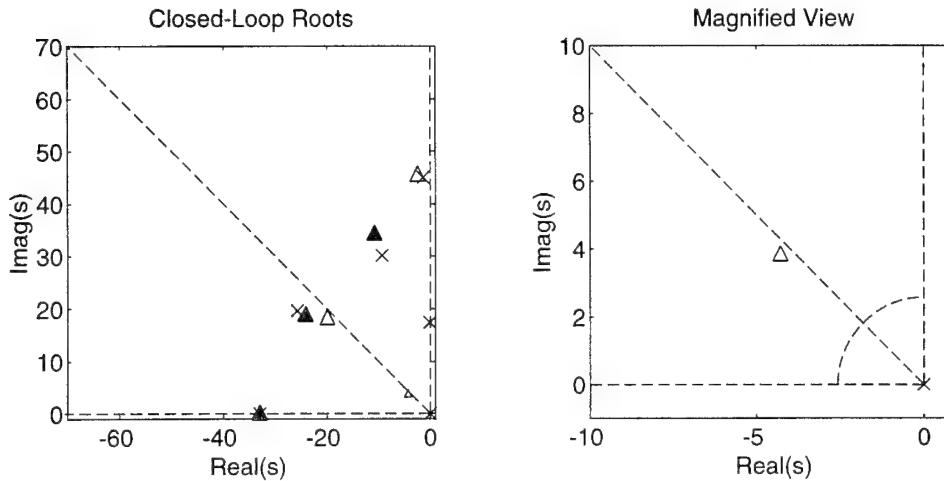
Figure 5.5: **Robust Design for Subsystem 2**

This figure shows the closed-loop root locations for the robust control design for subsystem two. This figure contains additional open-loop poles due to the prefilters. The filter closed-loop roots are represented by the black triangles. Because of the high cost of control at high frequencies, the controller makes essentially no effort to damp the second flexible mode of subsystem two. However, comparison of this figure with Figure 5.3 indicates that the root locations of the rigid- body mode and the first mode are unaffected by the frequency-weighted design.

poles due to augmenting the filter to the plant. The filter closed-loop roots are represented by the black triangles. The frequency-shaped design limits the output of the feedback controller above 5 Hz. Because of the high cost of control at high frequencies, the controller makes essentially no effort to damp the second flexible mode of subsystem two. However, comparison of this figure with Figure 5.3 indicates that the root locations of the rigid body and first mode are affected very little by the frequency-weighted design.

The robustness of this design is verified by the experimental response of Figure 5.6. In this response, the initial subsystem controller is active from 1.5 to 3 seconds. At three seconds, a control-swap is performed, and the robust subsystem controller is activated. The
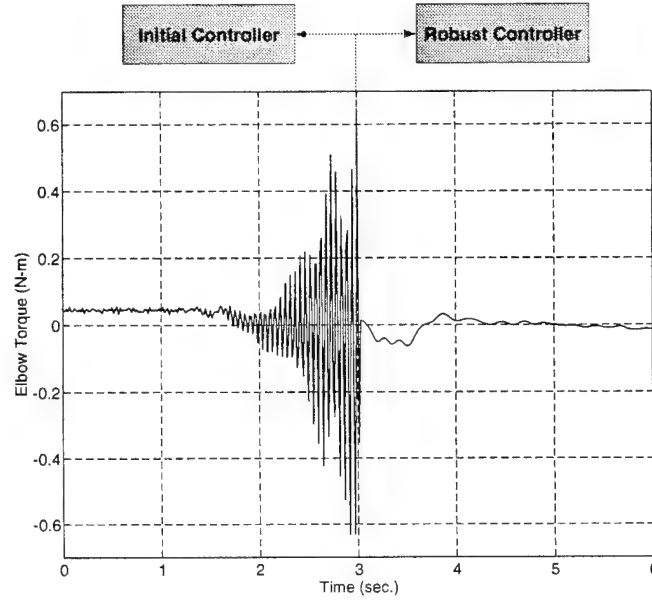
Figure 5.6: **Experimental Response of Robust Design for Subsystem 2**

In this response, the initial subsystem controller is active from 1.5 to 3 seconds. At 3 seconds, a control-swap is performed, and the robust subsystem controller is activated. The frequency-shaped controller stabilizes the system, and this torque history demonstrates the robustness of this design to high-frequency modelling uncertainty.

frequency-shaped controller stabilizes the system, and this torque history demonstrates the robustness of this design to high-frequency modelling uncertainty.

Control Design for Subsystem 1

With the second-subsystem controller designed, a controller for subsystem one was designed in a similar fashion based on a model of the form

$$
\begin{bmatrix} \dot{\mathbf{x}}_1(t) \\ \dot{\mathbf{x}}_2(t) \end{bmatrix} = \begin{bmatrix} \mathbf{A}_{11} & \mathbf{A}_{12} - \mathbf{B}_{12}\mathbf{K}_2 \\ 0 & \mathbf{A}_{22} - \mathbf{B}_{22}\mathbf{K}_2 \end{bmatrix} \begin{bmatrix} \mathbf{x}_1(t) \\ \mathbf{x}_2(t) \end{bmatrix} + \begin{bmatrix} \mathbf{B}_{11} \\ 0 \end{bmatrix} u_1(t). \tag{5.45}
$$

The controlled outputs for subsystem one, defined in Figure 5.7, are given by

$$
\mathbf{y}_{c_1} = \begin{bmatrix} w_{tip1} \\ \theta_{tip1} \end{bmatrix} = \mathbf{C}_{c_1}\mathbf{x}_1 \tag{5.46}
$$

where w_{tip1} and θ_{tip1} represent the lateral deflection and rotation of the tip of link 1.
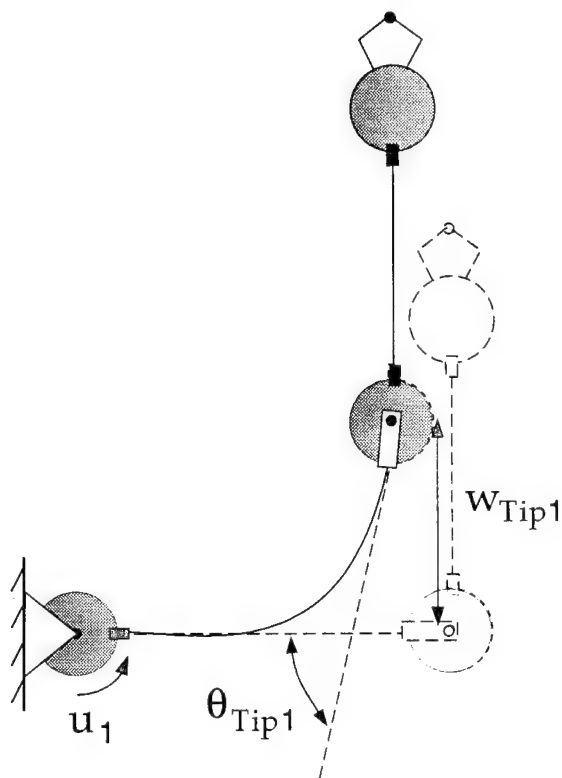
Figure 5.7: **Controlled Outputs of Subsystem 1**

This figure illustrates the controlled outputs of subsystem one. w_{tip1} and θ_{tip1} represent the lateral deflection and rotation of the tip of link 1. Also shown is the shoulder-motor input u_1.

Initial Design The weighting matrices for the first-subsystem design were varied until the requirements on the closed-loop roots were satisfied. The final weighting matrices for the subsystem-one design are given as

$$\mathbf{Q}_{u_1} = 1 \ (\text{N-m})^{-2} \tag{5.47}$$

$$\mathbf{Q}_{x_1} = \mathbf{C}_{c_1}{}^{\mathrm{T}} \mathbf{W}_{x_1} \mathbf{C}_{c_1} \tag{5.48}$$

with

$$\mathbf{W}_{x_1} = \begin{bmatrix} 100 \ \text{m}^{-2} & 0 \\ 0 & 20 \ \text{rad}^{-2} \end{bmatrix}. \tag{5.49}$$

The resulting control law is

$$u_1(t) = -\mathbf{K}_1 \mathbf{x}(t) \tag{5.50}$$

where

$$\mathbf{x}(t) = \begin{bmatrix} \mathbf{x}_1(t) \\ \mathbf{x}_2(t) \end{bmatrix} \tag{5.51}$$

and

$$\mathbf{K}_1 = \begin{bmatrix} \mathbf{K}_{11} & \mathbf{K}_{12} \end{bmatrix}. \tag{5.52}$$

The corresponding subsystem-one closed-loop-root locations for this design are shown in Figure 5.8. Both the rigid-body mode and the first flexible mode meet the damping specifications, and the rigid-body poles are well beyond the frequency of the first-cantilever zero of subsystem one.
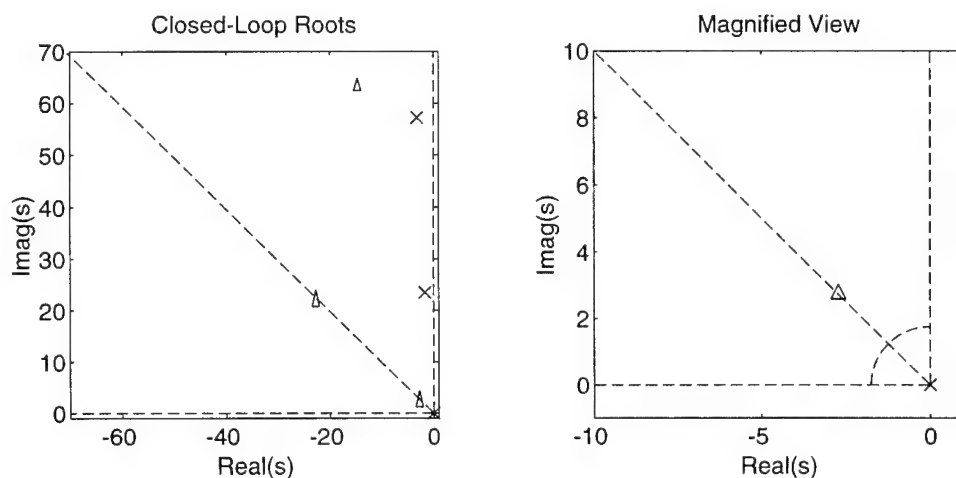
Figure 5.8: **Initial Design for Subsystem 1**

This figure shows the subsystem-one closed-loop root locations for the initial control design. The x's represent the open-loop roots, and the △'s represent the closed-loop roots. The diagonal dashed line corresponds to .707 damping. The figure on the right is a magnified view of the figure on the left. The quarter circle corresponds to the first-cantilever-mode natural frequency.

Robust Design   From the initial design for subsystem one, the frequency shaped-design was obtained by augmenting the plant with a fifth-order Butterworth filter with a 5 Hz cut-off frequency. The resulting closed-loop roots for subsystem one are shown in Figure 5.9. Because of the high cost of control at high frequencies, the controller makes essentially no
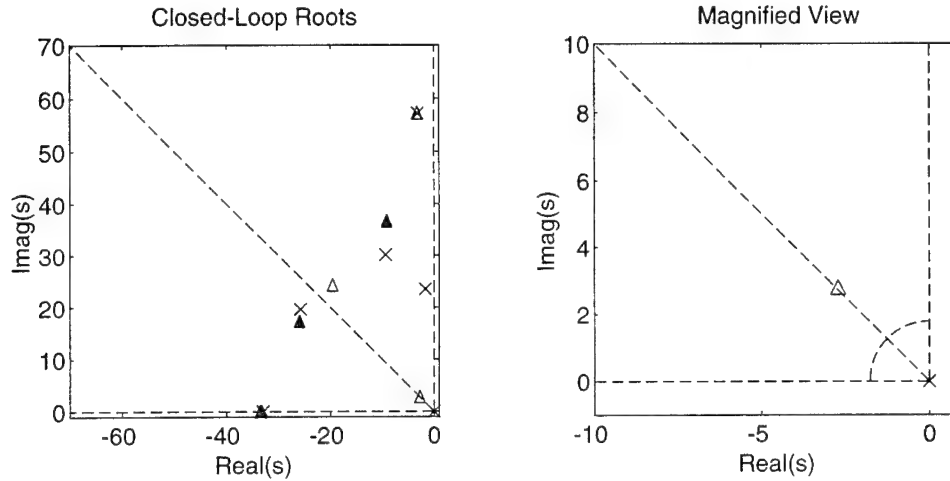
Figure 5.9: **Robust Design for Subsystem 1**

This figure shows the subsystem-one closed-loop root locations for the robust control design. This figure contains additional open-loop poles due to the prefilters. The filter closed-loop roots are represented by the black triangles. Because of the high cost of control at high frequencies, the controller makes essentially no effort to damp the second flexible mode of subsystem one. However, comparison of this figure with Figure 5.8 indicates that the root locations of the rigid- body mode and the first mode are essentially unaffected by the frequency-weighted design.

effort to damp the second flexible mode of subsystem one. There is a slight difference in the first-flexible-mode root locations between the robust design and the initial design. This is due to the prefilter cut-off frequency being very close to the frequency of the damped flexible mode. However, this discrepancy was not sufficiently significant to warrant redesign.

Resulting Closed-Loop System

Equations (5.44) and (5.50) together represent a total-system controller for the system of Equation (5.38). The gain matrices are given in Appendix F. The corresponding closed-loop

system is given by

$$
\begin{bmatrix} \dot{\mathbf{x}}_1(t) \\ \dot{\mathbf{x}}_2(t) \end{bmatrix} = \begin{bmatrix} \mathbf{A}_{11} - \mathbf{B}_{11}\mathbf{K}_{11} & \mathbf{A}_{12} - \mathbf{B}_{12}\mathbf{K}_2 - \mathbf{B}_{11}\mathbf{K}_{12} \\ 0 & \mathbf{A}_{22} - \mathbf{B}_{22}\mathbf{K}_2 \end{bmatrix} \begin{bmatrix} \mathbf{x}_1(t) \\ \mathbf{x}_2(t) \end{bmatrix}. \tag{5.53}
$$

The corresponding closed-loop roots of the plant are given in Figure 5.10.   Figure 5.11
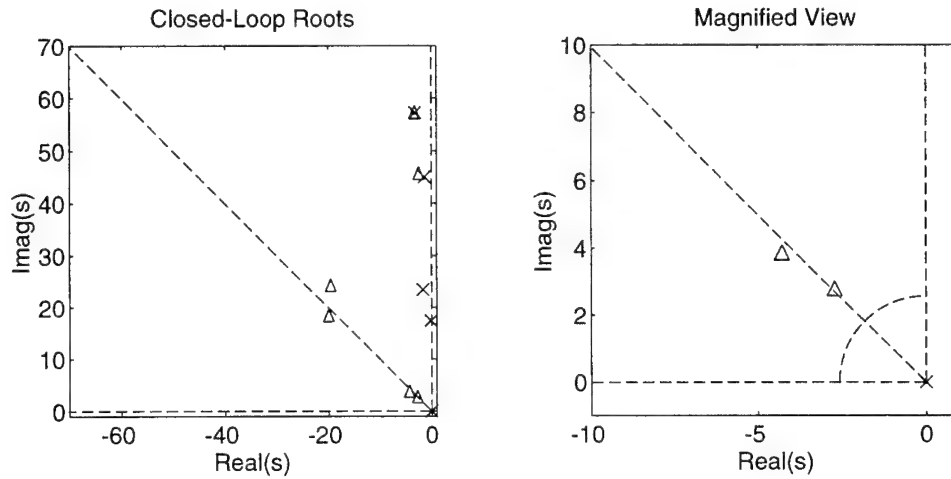
Figure 5.10: **System Controller**

This figure shows the closed-loop-root locations corresponding to the total-system controller.

shows the experimental response of the closed-loop system in following a desired end-point trajectory.   From the desired end-point position, corresponding joint angles are determined through inverse kinematics assuming rigid links.   The manipulator is then commanded to follow the desired motor positions. The corresponding end-point response is shown in Figure 5.11, along with the motor torque histories. Because the controller is error based, the actual end-point position trails the desired position. This response illustrates the need for feedforward control to follow more closely a desired state history.
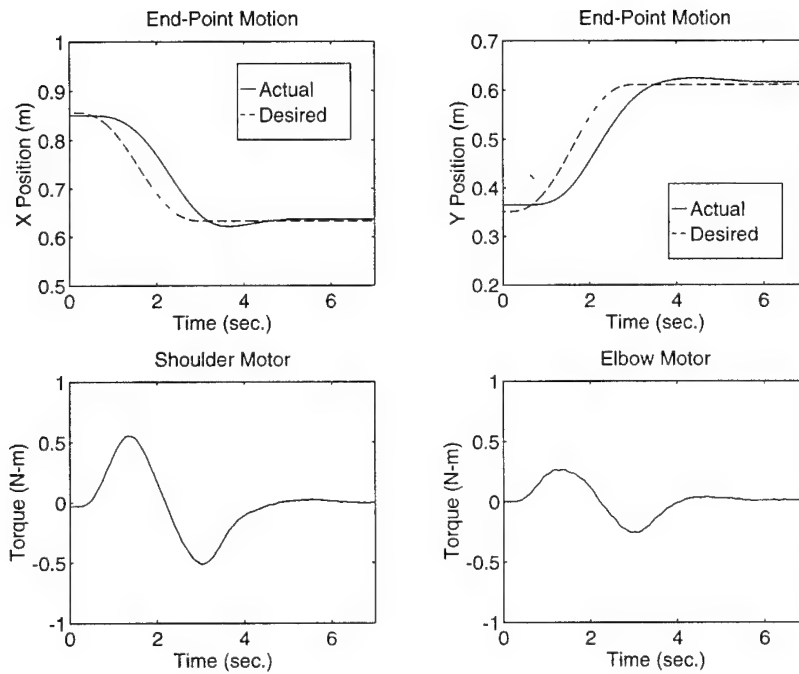
Figure 5.11: **Experimental Response**

This figure shows the response of the closed-loop system in following a desired end-point trajectory. Because the controller is error based, the actual end-point position trails the desired position. This response illustrates the need for feedforward control to follow more closely a desired state history.

5.3.2   Mini-Manipulator Control Design

The goal of the mini-manipulator control design is to generate the torques τ_1 and τ_2 to control the mini-manipulator tip to the desired tip position in inertial space. As described in Chapter 3, the dynamics of the mini-manipulator can be well represented as a tip mass controlled by linear actuators. The corresponding equations of motion are given by

$$
\begin{bmatrix} \dot{x}_{m_T} \\ \dot{y}_{m_T} \\ \ddot{x}_{m_T} \\ \ddot{y}_{m_T} \end{bmatrix} = \begin{bmatrix} 0 & 0 & 1 & 0 \\ 0 & 0 & 0 & 1 \\ 0 & 0 & 0 & 0 \\ 0 & 0 & 0 & 0 \end{bmatrix} \begin{bmatrix} x_{m_T} \\ y_{m_T} \\ \dot{x}_{m_T} \\ \dot{y}_{m_T} \end{bmatrix} + \begin{bmatrix} 0 & 0 \\ 0 & 0 \\ \frac{1}{m_T} & 0 \\ 0 & \frac{1}{m_T} \end{bmatrix} \begin{bmatrix} F_x \\ F_y \end{bmatrix} \tag{5.54}
$$

where x_{m_T} and y_{m_T} are the tip position relative to the base as shown in Figure 5.12.   For
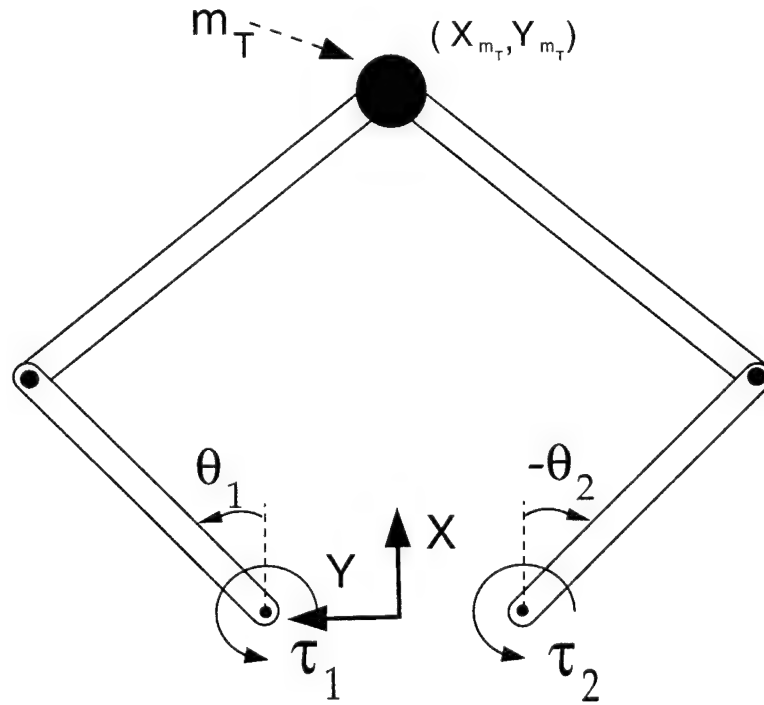
Figure 5.12: **Mini-Manipulator Subsystem**

The goal of the mini-manipulator control design is to generate the torques τ_1 and τ_2 to control the mini-manipulator tip to the desired tip position in inertial space.

the system of Equation (5.54), a linear-quadratic-regulator (LQR) design was performed.

The weighting matrices chosen were

$$\mathbf{Q}_u \quad = \quad \begin{bmatrix} 1.2 \text{ N}^{-2} & 0 \\ 0 & 1.2 \text{ N}^{-2} \end{bmatrix} \tag{5.55}$$

$$\mathbf{Q}_x \quad = \quad \begin{bmatrix} 10000 \text{ m}^{-2} & 0 & 0 & 0 \\ 0 & 10000 \text{ m}^{-2} & 0 & 0 \\ 0 & 0 & 0 & 0 \\ 0 & 0 & 0 & 0 \end{bmatrix}. \tag{5.56}$$

The regulator is of the form

$$\mathbf{F} \quad = \quad -\mathbf{K}_p \mathbf{x} - \mathbf{K}_v \dot{\mathbf{x}} \tag{5.57}$$

where

$$\mathbf{F} \quad = \quad \begin{bmatrix} F_x \\ F_y \end{bmatrix} \tag{5.58}$$

$$\mathbf{x} \quad = \quad \begin{bmatrix} x_{m_T} \\ y_{m_T} \end{bmatrix} \tag{5.59}$$

$$\dot{\mathbf{x}} \quad = \quad \begin{bmatrix} \dot{x}_{m_T} \\ \dot{y}_{m_T} \end{bmatrix} \tag{5.60}$$

and $\mathbf{K}_p$ and $\mathbf{K}_v$ are the 2×2 resulting gain matrices. The corresponding closed-loop-root locations are shown in Figure 5.13. Because the dynamics of the mini in both the x_{m_T} and x_{m_T} coordinates and the weighting on these coordinates were identical, the LQR design placed the closed-loop roots at the same location.

Implementation

The controller in Equation (5.57) was implemented as a joint-based controller. For small displacements, the corresponding joint controller is given by

$$\tau \quad = \quad -\mathbf{J}^{\mathrm{T}} \mathbf{K}_p \mathbf{J} \theta - \mathbf{J}^{\mathrm{T}} \mathbf{K}_v \mathbf{J} \dot{\theta} \tag{5.61}$$

where

$$\tau \quad = \quad \begin{bmatrix} \tau_1 \\ \tau_2 \end{bmatrix} \tag{5.62}$$
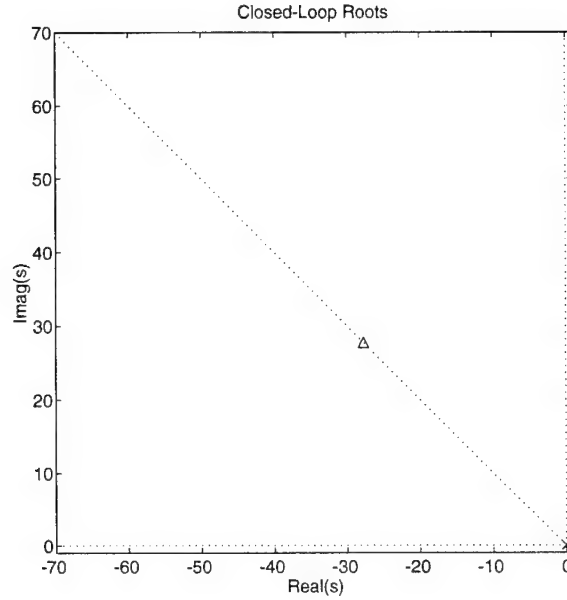
Figure 5.13: **Mini-Manipulator-Subsystem Closed-Loop Roots**

The figure shows the closed-loop-root locations corresponding to the mini-manipulator control design. Because the dynamics of the mini in both the x_{m_T} and x_{m_T} coordinates and the weighting on these coordinates were identical, the LQR design placed the closed-loop roots at the same location.

$$\theta \;=\; \begin{bmatrix} \theta_1 \\ \theta_2 \end{bmatrix} \tag{5.63}$$

$$\dot{\theta} \;=\; \begin{bmatrix} \dot{\theta}_1 \\ \dot{\theta}_2 \end{bmatrix} \tag{5.64}$$

and **J** is the mini-manipulator Jacobian (given in Appendix B) for a nominal mini-manipulator configuration.

Experimental Results

Figures 5.14 and 5.15 show step responses of the mini-manipulator motors.   The corresponding tip motion is primarily in the X direction in Figure 5.14, and primarily in the Y direction in Figure 5.15.

Using the approximate relationships given in [48] between rise time and bandwidth $t_r \approx 1.8/\omega_n$, and overshoot and damping, the responses in Figures 5.14 and 5.15 reflect a
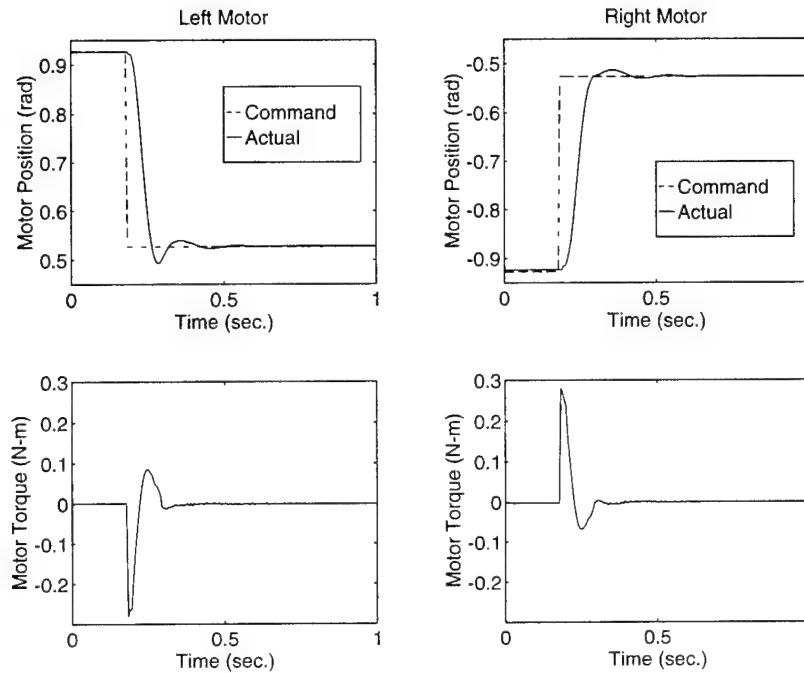
Figure 5.14: **Experimental Step Response**

The motor responses in this figure correspond to tip motion in primarily the X direction.

bandwidth of approximately 25 *rad/sec.* and an approximate damping ratio of .7. These values correspond closely to the theoretical closed-loop roots shown in Figure 5.13.

Given the performance of the joint-based controller, controlling the mini-manipulator tip to a desired target requires specifying appropriate desired joint angles and angular rates. When the target is within reach, these desired values are calculated based on vision-sensor information and inverse-kinematic relations given in Appendix B. When the target is out of reach, the desireds correspond to the point on the boundary of the mini-manipulator workspace that is closest to the desired target. Figure 5.16 demonstrates the ability to generate suitable joint commands to regulate the mini-manipulator tip to a desired target in the presence of base motions. With the main-arm controller off, the base of the mini-manipulator is displaced as shown. The induced error in the mini-manipulator-tip position is also shown. By specifying the proper joint commands, and then regulating the joints
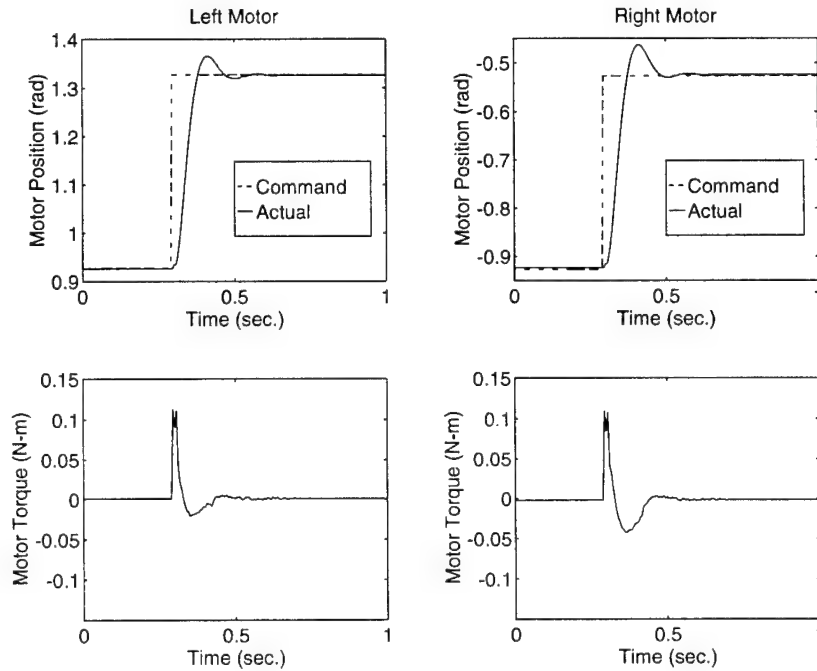
Figure 5.15: **Experimental Step Response**

The motor responses in this figure corresponds to tip motion in primarily the Y direction. Using the approximate relationships given in [48] between rise time and bandwidth ($t_r \approx 1.8/\omega_n$) , and between overshoot and damping, the responses in this figure and Figure 5.14 reflect a bandwidth of approximately 25 rad/sec. and an approximate damping ratio of .7.

to these commands, the mini-manipulator is able to compensate for the base motion and regulate effectively the tip to the desired target.

The redundancy introduced by the mini-manipulator also improves tip-disturbance rejection of the system as shown in Figure 5.17. Figure 5.17 presents two cases in which an approximately constant tip disturbance is applied. In the plot on the left, the joints of the mini-manipulator are locked, and a tip disturbance is applied to the mini-manipulator tip. The disturbance rejection in this case is provided entirely by the shoulder and elbow torques generated by the main-arm controller. The corresponding induced tip errors are much larger than in the plot on the right where the mini-manipulator controller is active.
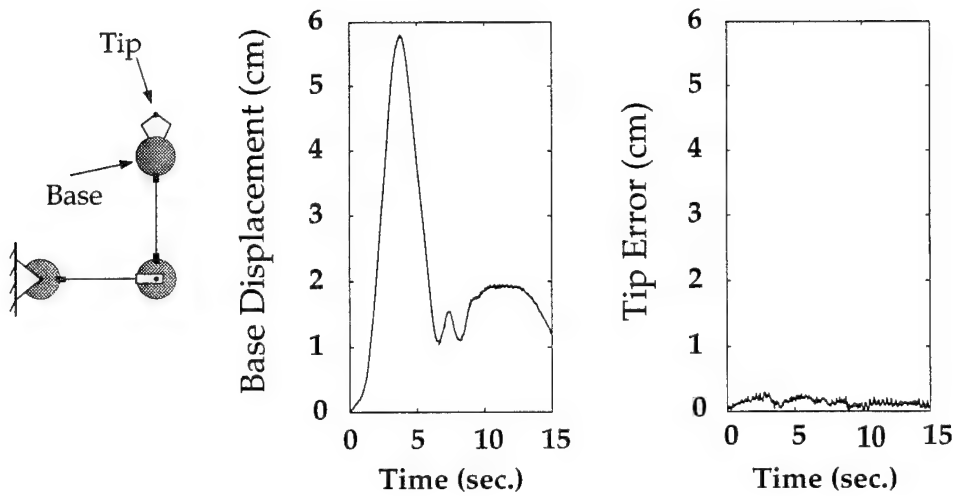
Figure 5.16: **Mini-Controller Base-Disturbance Rejection**

This figure shows experimental results in which the main-arm controller is turned off and the base of the mini-manipulator is displaced as shown. The induced error in the mini-manipulator-tip position is also shown. By specifying the proper joint commands based on end-point sensing of the mini-manipulator's tip location, and then regulating the joints to these commands, the mini-manipulator is able to compensate for the base motion and regulate the tip to the desired target.

The plot on the right illustrates the ability of the redundant system to keep tip errors very small in the presence of a tip disturbance.
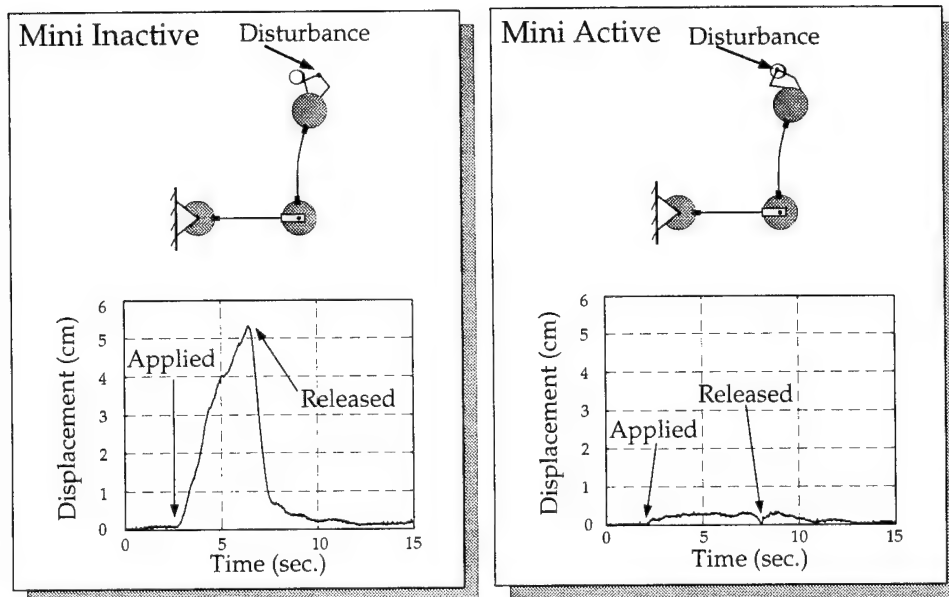
Figure 5.17: **Tip-Disturbance Rejection**

This figure presents two cases in which an approximately constant tip disturbance is applied. In the plot on the left, the joints of the mini-manipulator are locked, and a tip disturbance is applied to the mini-manipulator tip. The disturbance rejection in this case is provided entirely by the shoulder and elbow torques generated by the main-arm controller. The corresponding induced tip errors are much larger (a factor of almost 25) than in the plot on the right where the mini-manipulator controller is active. The plot on the right illustrates the ability of the redundant system to keep tip errors very small in the presence of a tip disturbance.

5.4   Summary

This chapter has presented the feedback-control approach developed in this research for *predominantly* one-way coupled systems. This approach exploits the one-way coupling that characterizes these systems within the frequency range of interest for control. As a result, the development of a total-system controller is partitioned into sequential subsystem designs. Because the one-way coupling characteristic is inaccurate outside of the frequency range of interest, the subsystem controllers are made to be robust to this model uncertainty. Robust subsystem controllers are achieved through a frequency-shaped control design.

This approach has been applied to the experimental apparatus. With this approach, control design for the main arm was partitioned into two sequential subsystem control designs. These subsystem controllers were designed to meet performance specifications (in the form of desired closed-loop regions) within the frequency range of interest, while at the same time achieving robustness to model uncertainty outside of this frequency range. The development of a total-system controller was completed with the mini-manipulator control design. The resulting controller will be used in the following chapter to augment the control input of the trajectory generator in a point-to-point repositioning of the mini-manipulator/main-arm experimental system.

Chapter 6

"Putting It All Together"

Chapters 4 and 5 described the approaches developed in this dissertation to design the trajectory-generator and feedback-controller components of the control-system framework described in Chapter 1. This chapter presents experimental results demonstrating the performance of this control strategy on the mini-manipulator/main-arm system.
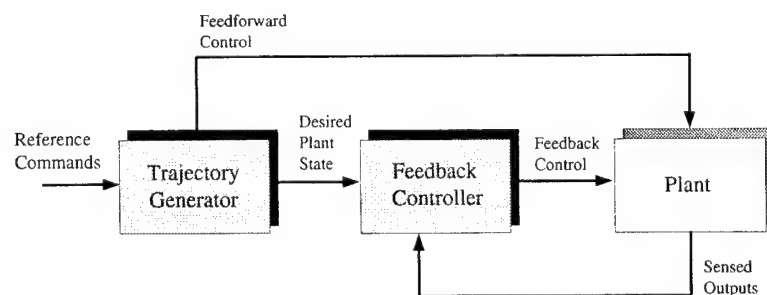
Figure 6.1: **Control Framework**

Chapters 4 and 5 described the approaches developed in this dissertation to design the trajectory-generator and feedback-controller components of the solution framework described in Chapter 1. This chapter present experimental results demonstrating the performance of this control strategy on the mini-manipulator/main-arm system.

6.1 Interface to the Experimental System

A graphical user interface, shown in Figure 6.2, has been developed to enable the user to specify commands to the system in an intuitive fashion. The user interface displays icons of the mini-manipulator tip and desired targets. These icons represent the actual positions provided by the vision sensor. The interface enables the user to specify final tip positions by using a computer mouse to drag the icon of the mini-manipulator to a position on the screen, or by clicking on one of the target icons. Clicking on one of the targets sets the desired tip position to the location of the *center* of the target. The slew time is specified by clicking on the desired time.

6.2 Experimental Point-to-Point Repositionings

To illustrate the contributions of both the feedforward and feedback inputs to the system, results corresponding to two cases are presented (see Figure 6.3). In the first case, the feedforward-control-input connection is broken. The resulting response is due to the feedback controller attempting to regulate the plant to the desired state history provided by the trajectory generator. In the second case, both the feedforward and feedback inputs are sent to the plant, representing the performance of the control strategy developed in this thesis. In addition, for both cases, results are presented with the mini-manipulator active and inactive to illustrate the advantages of the mini-manipulator.

For these experiments, the "acceptable time for repositioning" is set arbitrarily at 2.5 seconds. The experimental response for each case is presented in four plots. The tip error represents the distance between the mini-manipulator-tip position and the desired mini-manipulator-tip position. The base error is the distance between the position of the mini-manipulator base and the nominal steady-state location of the base that corresponds to the desired final configuration. Also shown is the feedforward-control input from the trajectory generator and the total control (feedforward plus feedback) sent to the plant for both the shoulder and elbow actuators. Figures 6.4 through 6.7 correspond to 2.5 second repositionings in which the mini-manipulator tip is commanded to move from $(.9279, .4904)$ to $(.6394, .7675)$ where the X and Y coordinates are defined in Figure 4.6.
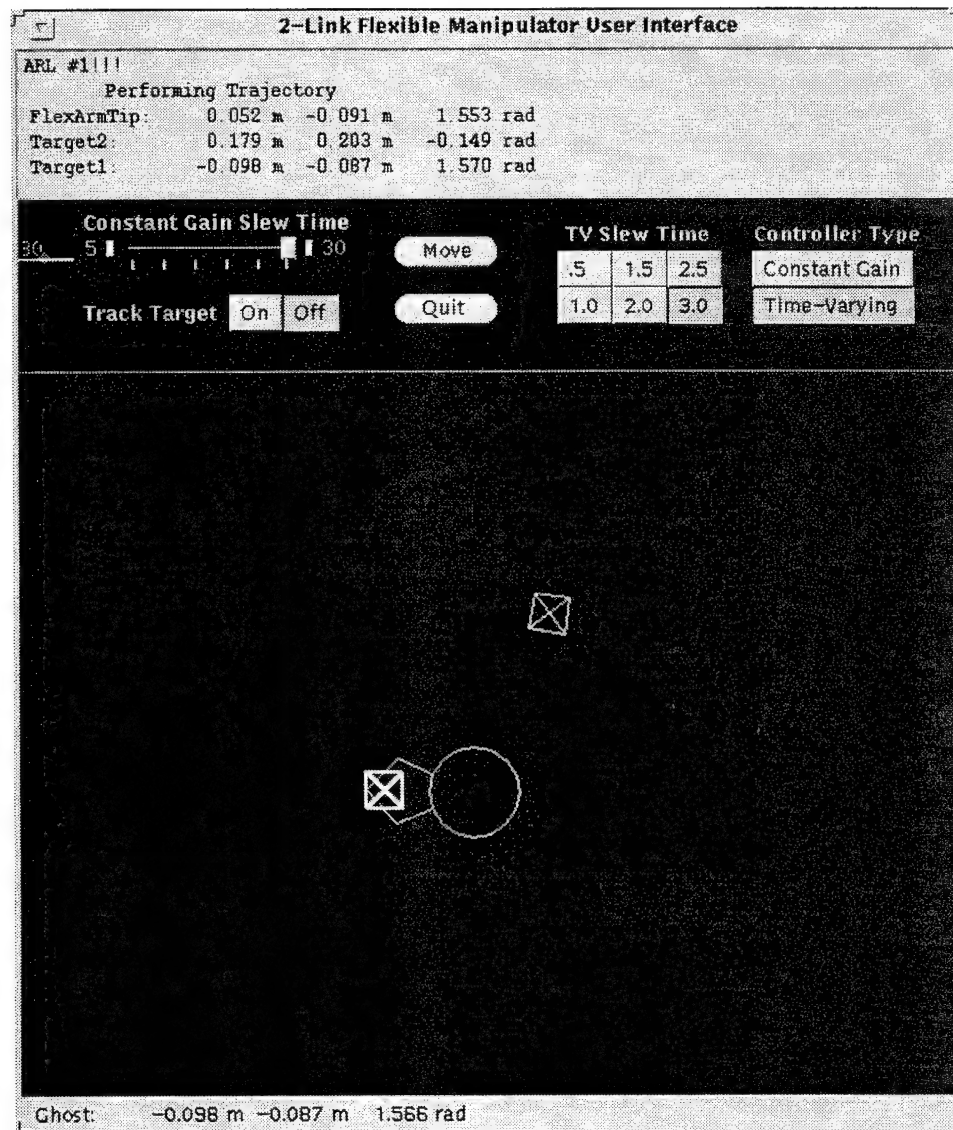
Figure 6.2: **Graphical User Interface to the Experimental System**

This graphical user interface has been developed to enable the user to specify commands to the system in an intuitive fashion.
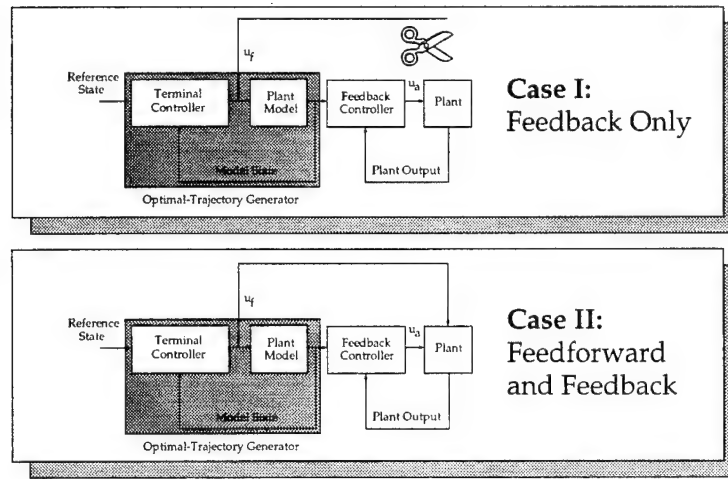
Figure 6.3: **Experimental Cases**

To illustrate the contributions of both the feedforward and feedback inputs to the system, results corresponding to two cases are presented. In Case I, the feedforward-control-input connection is broken. The resulting response is due to the feedback controller attempting to regulate the plant to the desired state history. In Case II, both the feedforward and feedback inputs are sent to the plant, representing the performance of the control strategy developed in this thesis.

6.2.1   Case I: Feedback Only

Mini-Manipulator Inactive   In the response of Figure 6.4, the main arm is controlled by feedback alone, and the mini-manipulator joints are locked. The performance represents the ability of feedback control with the main arm only to track the optimal desired state history produced by the trajectory generator. With feedback and the main arm alone, the system is not able to meet the repositioning-time requirement of 2.5 seconds; it completes the repositioning in approximately 5.2 seconds.

Mini-Manipulator Active   In the response of Figure 6.5, the main arm is controlled by feedback alone, now with the mini-manipulator active. Without feedforward, the system is still not able to quite meet the 2.5 second repositioning-time requirement, but the mini-manipulator is able to acquire the target after 3.2 seconds: the mini-manipulator achieves a 2 second decrease in the repositioning time compared to the previous response.
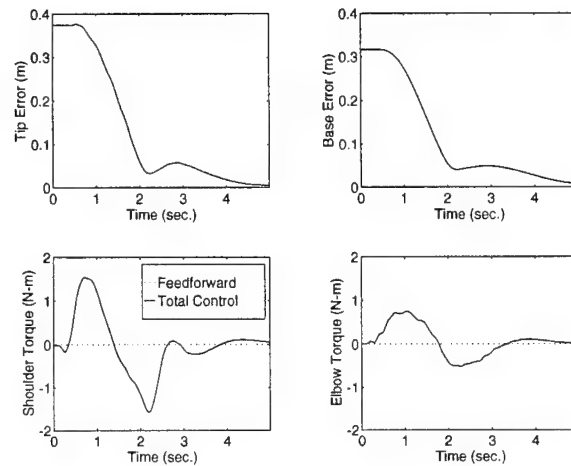
Figure 6.4: **Experimental Response: Feedback Only/Mini-Manipulator Inactive**

The tip reaches the target in 5.2 seconds.
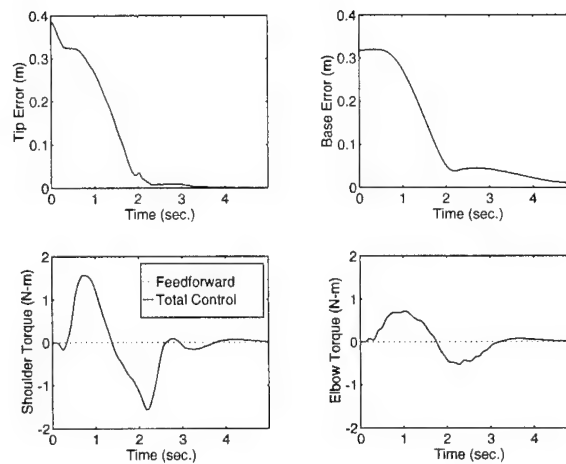
Figure 6.5: **Experimental Response: Feedback Only/Mini-Manipulator Active**

The tip reaches the target in 3.2 seconds.

6.2.2   Case II: Feedback and FeedForward

Mini-Manipulator Inactive   In the response of Figure 6.6, the main arm is controlled by both feedback and feedforward control, and the mini-manipulator joints are locked. The repositioning is completed in approximately 4.5 seconds. Comparison with Figures 6.4
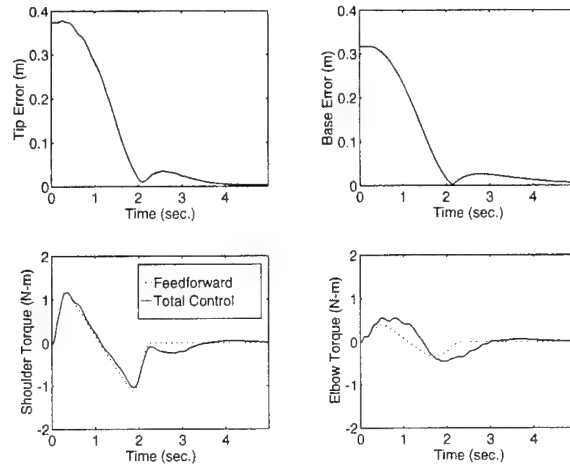
Figure 6.6: **Feedback and FeedForward/Mini-Manipulator Inactive**

The tip reaches the target in 4.5 seconds.

and 6.5 indicate that the use of feedforward and feedback does result however in a more efficient use of control effort, since the total control effort and peak control effort used in Figure 6.6 is less than in Figures 6.4 and 6.5. However, without the mini-manipulator the system is still unable to meet the repositioning-time requirement.

Mini-Manipulator Active   In the response of Figure 6.7, the main arm is controlled by both feedback and feedforward control, and the mini-manipulator is active. This response represents the culmination of this research. The mini-manipulator is now able to acquire the target within 2.5 seconds. Consequently, the control strategy merging feedback and feedforward control is able to meet the stringent repositioning requirement selected for the experimental system.

Figure 6.8 shows a response for the same initial and final tip positions with a 3 second selection for final time, instead of the 2.5 second selection used up to here. An interesting observation of this response is that less feedback-control input is required than in the 2.5
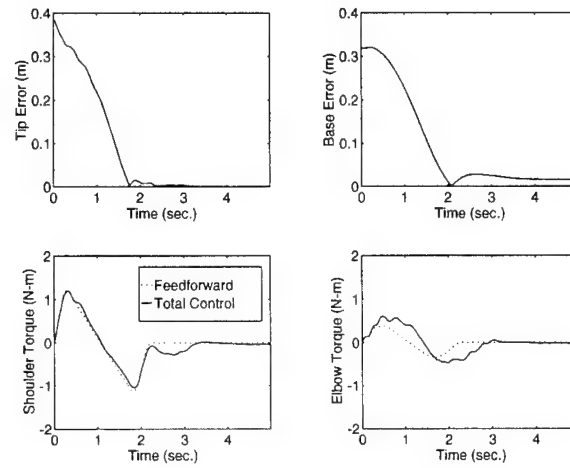
Figure 6.7: **Feedback and FeedForward/Mini-Manipulator Active**

The tip reaches the target in 2.5 seconds.
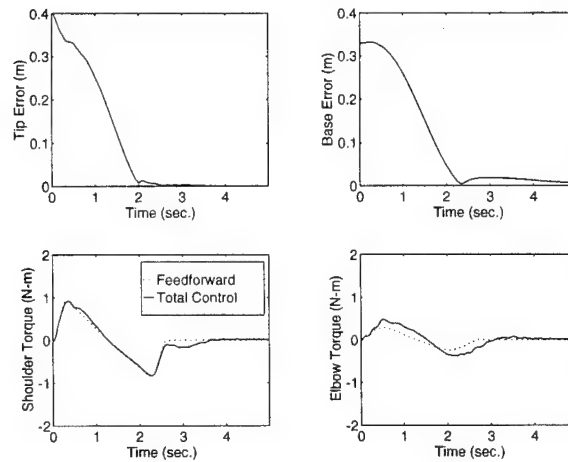
Figure 6.8: **Feedback and FeedForward/Mini-Manipulator Active:** $t_f = 3.0$ **Seconds**

The tip still reaches the target in 2.5 seconds.

second slew. This is because in the 3 second slew, there is significantly less link deflection. Consequently, the model of the main arm that was developed assuming small link deflections is more accurate during this repositioning. Thus, the plant state follows the model state closely from the feedforward input, and less feedback is drawn upon.

Finally, for comparison, Figure 6.9 shows a 3 second repositioning corresponding to a relatively small-motion repositioning. The mini-manipulator tip is commanded to move
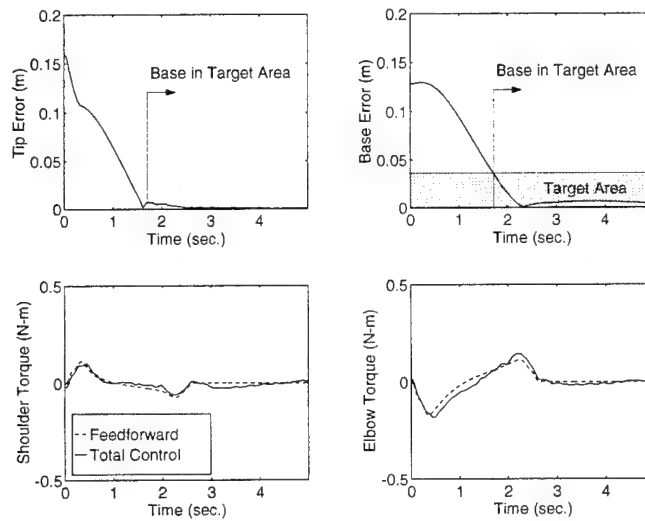
Figure 6.9: **Small-Motion Repositioning:** $t_f = 3.0$ **Seconds**

The tip still reaches the target in 2.5 seconds.

from $(.5069, .6792)$ to $(.6390, .7676)$, a total distance of 15 cm compared with 38 cm in the previous tests. As in the response of Figure 6.8, the corresponding link deflections are small and the manipulator is controlled primarily from the feedforward-control signal. The feedback loop is called upon for only minor additions to the feedforward-control input.

Furthermore, Figure 6.9 also supports the the primary tenet of this thesis. Specifically, once the base of the mini-manipulator is within an *area* (indicated approximately by the shaded region in Figure 6.9), the mini-manipulator is able to acquire the desired position accurately and quickly.

6.3   Summary

This chapter presented experimental results that verify the ability of the control strategy developed in this thesis to reposition quickly the mini-manipulator/main-arm system. From these experiments, a number of observations were made. First, without both feedforward and feedback control, the stringent (2.5 second) time requirement for the repositioning command is not met. Second, for the 2.5 second repositionings presented here, meeting the repositioning-time requirement was only possible with the mini-manipulator active (without it, the move took at best 4.3 seconds). Third, the combination of feedback and feedforward control resulted in a more efficient use of control effort than using feedback alone to follow the desired state erformance was achieved with less peak and total control usage.

$\sim$

Chapter 7

Conclusions

This final chapter consists of two sections. The first section summarizes the findings of this research. The second gives suggestions for future research.

7.1 Summary

This research has addressed increasing the end-point performance of multi-link flexible manipulators through the use of a *mini-manipulator*, or small, high-bandwidth rigid robot. Mounting a mini-manipulator at the tip of a multi-link flexible manipulator introduces high-bandwidth, local-manipulation capability and redundant degrees of freedom that, in conjunction with direct end-point sensing, enable high-performance end-point control in the presence of link flexibility that is substantial.

Contributions made in the course of this research are summarized in Section 1.5. The work has led to the conclusions that follow.

7.1.1 Exploiting the Speed and Redundancy of the Mini-Manipulator

To exploit the high-bandwidth local-manipulation capability and the redundancy introduced by the mini-manipulator, a new control strategy has been developed for multi-link flexible manipulators. Because the mini-manipulator provides quick, precise control, but only within a localized workspace, the end-point performance of the overall system is limited by the speed at which the flexible main arm can transport the mini-manipulator. As a result, this new strategy has focused on controlling quickly the flexible main arm to a *target area*, rather than to a precise location, from which the mini-manipulator can obtain the desired

111

tip position. This new concept of controlling to a target area was pursued in this research through a new technique known as *soft terminal control*. The experiments performed have demonstrated the ability to control to an area much more quickly than to a specific point.

7.1.2   Soft Terminal Control of Multi-Link Flexible Manipulators

Soft terminal control of a multi-link flexible manipulator is made possible by the speed and redundancy introduced by the mini-manipulator. Because of this redundancy, the target can be acquired with the system in more than one configuration. Rather than controlling the flexible main arm to a specific point, high performance of the overall system can be achieved by quickly bringing the main arm near the target, to a target area; an area within which the speed and precision of the mini-manipulator can then be utilized to perform the task at hand.

A new soft-terminal-control approach has been developed for multi-link flexible manipulators. This approach combines feedforward control, produced by a trajectory generator, with feedback control to control quickly the main arm to the target area. The culmination of this research was an experimental verification of this approach on an extremely flexible two-link manipulator with a mini-manipulator mounted at its tip. Experimental results demonstrated increased performance offered by the mini-manipulator using this combination of feedforward and feedback control. For the system repositionings presented in this dissertation, the mini-manipulator enabled nearly a factor of two decrease in repositioning times. Also, the mini-manipulator reduced tip errors due to tip disturbances by a factor of 25.

In developing this new soft-terminal-control approach, fundamental advances were made in trajectory generation, feedback-control design, and modelling of multi-link flexible manipulators.

Trajectory Generation

A new trajectory-generation approach for multi-link flexible manipulators has been developed that incorporates into the trajectory generation the concept of controlling to a target area rather than to a specific point. This approach generates both the optimal-state history and the corresponding feedforward-control input for repositioning multi-link flexible manipulators. This approach is based on an explicit-model-following implementation of a terminal controller, in which the terminal controller drives a plant model to the desired

plant state. The output of the terminal controller is the optimal control for the repositioning, and is fed forward to the plant. The corresponding plant-model state history is the optimal state history for the repositioning, and represents the desired motion of the plant. The target-area concept is incorporated into the terminal-controller design in the form of *soft terminal constraints.*

A method has been developed to shape the frequency content of the generated trajectories so as not to excite lightly-damped unmodelled flexible modes. This method involves frequency weighting the finite-time, linear-quadratic cost function in the terminal-controller design. It worked very well. As a result, this approach is directly applicable to manipulators exhibiting significant link flexibility. Furthermore, time weighting of the cost function and implementation of the terminal controller in a model-following control framework did in fact enable an essentially bumpless control-mode transfer at the end of the large-motion slews.

Feedback-Control Design

As a first step toward reducing the high-performance-control design problem for general multi-link flexible manipulators into smaller more tractable subsets, a sequential control-design approach for predominantly one-way-coupled systems has been developed. By exploiting this limited-coupling characteristic, this control approach enabled a straightforward sequential design process. The subsystem controllers were made robust to model uncertainty outside the frequency range of interest through a frequency-shaped control design. Because system-level coupling information was fully utilized in this process, and not overlooked, high performance was achieved; yet, through a sequential control-design process.

Modelling

A modular approach to modelling multi-link flexible manipulators has been developed. In this approach, a total-system model is generated through a concatenation, or integration, of state-space subsystem models. This technique enables the concatenation by enforcing the physical constraints that couple the subsystems. Thus, a total-system model can be developed by first developing accurate subsystem models, and then integrating to generate a total-system mathematical representation.

This modelling approach was applied to develop an accurate model of the experimental two-link flexible manipulator with a mini-manipulator at its tip. This model was used in the design of optimal trajectories and of a feedback controller for the experimental system.

7.2   Recommendations for Future Work

Performing this research generated a number of ideas for possible future research. The following is a list of possible future project ideas.

1. This research demonstrated the performance advantages of a terminal-control approach. However, inherent in this approach was the assumption that the manipulator could be well represented by a linear-time-invariant state-space model. For increased generality, the prospect of extending this approach to handle configuration dependency should be investigated.

2. This research has illustrated the performance benefits that result from the redundancy introduced by the mini-manipulator. In a similar way, there may be performance benefits inherent in *redundant-link* flexible manipulators. There are certainly applications where redundant manipulators will be required: weaving through space structures, grasping objects in different configurations, etc. As a result, it will be important to understand how best to exploit the redundancy to meet performance objectives.

3. Numerous projects have been performed involving the use of cooperating manipulators to accomplish a coordinated task. To date, this research has involved the use of rigid-link robots only. To investigate cooperative manipulation with two flexible-link robots, the problem of two flexible manipulators with mini-manipulators cooperatively manipulating an object should be looked into. A preliminary step in this investigation will probably require force control capability at the end of a multi-link flexible manipulator with a mini-manipulator.

4. Outside of ARL, there has been a large research effort in the development of *distributed* actuators and sensors [49]. The redundant actuation and sensing introduced by distributed control will enable the development of fundamentally new control approaches for flexible systems. A large-scale mock up of a flexible beam with a number of actuators and sensors mounted along the link would enable the development of new

control approaches while researchers work to improve the actual sensor and actuator technology. Possible approaches that might be used include: the design of independent modal controllers in which a group of actuators are used to control each mode individually; the use of neural networks; the development of a hybrid approach that intelligently merges neural networks and advanced flexible-system control theory.

5. Much of the research in flexible manipulators has been limited to 2-D. Although this limitation has enabled some fundamental flexibility issues to be studied and well understood, there may be fundamental issues, rather than just complexity issues, associated with 3-D out of plane vibrations. Possible issues include coupling between modes, torsion/bending coupling, actuator selection, and sensing.

6. In this research, it was assumed that the manipulator base was fixed. However, for many applications, this assumption may not be valid. Previous research has addressed the problem of controlling a rigid robot mounted on a compliant or mobile base. Extending this capability to include link flexibility will increase the scope of applications for flexible-link manipulators.

7. Recently, there have been significant advances made in robust-control theory. These robust-design approaches could be incorporated into the sequential regulator-design procedure described in Chapter 5.

$\sim$

116

Appendix A

The State-Space Model Concatenation Method

This appendix presents a summary of the State-Space Model Concatenation Method [28] that was utilized in the modular modelling approach presented in Chapter 3.

The State-Space Model Concatenation Method takes as input two subsystem state-space models of the form

$$
\begin{aligned}
\dot{\mathbf{x}}_i &= \mathbf{A}_i\mathbf{x}_i + \mathbf{B}_i^u\mathbf{u}_i(t) + \mathbf{B}_i^e\mathbf{e}_i \\
\mathbf{z}_i &= \mathbf{C}_i^z\mathbf{x}_i \\
\mathbf{f}_i &= \mathbf{C}_i^f\mathbf{x}_i \\
\mathbf{d}_i &= \mathbf{C}_i^d\mathbf{x}_i
\end{aligned}
\tag{A.1}
$$

where the dimensions for subsystem i, $i = 1, 2$, are specified as the state vector $\mathbf{x}_i \in \mathbb{R}^{ns_i}$, external input vector $\mathbf{u}(t)_i \in \mathbb{R}^{nu_i}$, internal effort vector at the interface $\mathbf{e}_i \in \mathbb{R}^{ne_i}$, monitored output vector $\mathbf{z}_i \in \mathbb{R}^{nz_i}$, internal flow vector at the interface $\mathbf{f}_i \in \mathbb{R}^{nf_i}$, and internal displacement vector at the interface $\mathbf{d}_i \in \mathbb{R}^{nd_i}$, with $\mathbf{A}_i$, $\mathbf{B}_i^u$, $\mathbf{B}_i^e$, $\mathbf{C}_i^z$, $\mathbf{C}_i^f$, and $\mathbf{C}_i^d$ having consistent dimensions. The output of the algorithm is a state-space realization for the total system.

Algorithm Summary

Given the subsystem state-space models, the total-system model is found by performing the following steps:

1. Form the output matrices $\mathbf{C}_i^{z_{com}}$ of the form

$$\mathbf{C}_i^{z_{com}} \;=\; \left[\begin{array}{c} \mathbf{C}_i^d \\ \mathbf{C}_i^f \end{array} \right]. \tag{A.2}$$

2. Form the Γ matrix defined by

$$\Gamma \;=\; \left(\mathbf{C}_1^f \mathbf{B}_1^e + \mathbf{C}_2^f \mathbf{B}_2^e \right)^{-1}. \tag{A.3}$$

3. Form the augmented output matrix $\mathbf{C}_2^a$

$$\mathbf{C}_2^a \;=\; \left[\begin{array}{c} \mathbf{C}_2^{z_{com}} \\ \mathbf{C}_2^{z_{ind}} \end{array} \right] \tag{A.4}$$

where [28] gives an algorithm for computing $\mathbf{C}_2^{z_{ind}}$ such that

$$\mathbf{z}_2^{ind} \;=\; \mathbf{C}_2^{z_{ind}} \mathbf{x}_2. \tag{A.5}$$

4. Form the total-system state-space realization of the form

$$\dot{\mathbf{x}} \;=\; \mathbf{A}\mathbf{x} + \mathbf{B}\mathbf{u}$$
$$\mathbf{z} \;=\; \mathbf{C}\mathbf{x}$$

$$\mathbf{x} = \left\{ \begin{array}{cc} \mathbf{x}_1^T & \mathbf{z}_{2ind}^T \end{array} \right\}^T,$$
$$\mathbf{u} = \left\{ \begin{array}{cc} \mathbf{u}_1^T & \mathbf{u}_2^T \end{array} \right\}^T,$$

and

$$\mathbf{z} = \left\{ \begin{array}{cc} \mathbf{z}_1^T & \mathbf{z}_2^T \end{array} \right\}^T.$$

$\mathbf{A}$ and $\mathbf{B}$ are most easily expressed in block form as

$$\mathbf{A} = \left[\begin{array}{cc} \mathbf{A}_{11} & \mathbf{A}_{12} \\ \mathbf{A}_{21} & \mathbf{A}_{22} \end{array} \right], \quad \mathbf{B} = \left[\begin{array}{cc} \mathbf{B}_{11} & \mathbf{B}_{12} \\ \mathbf{B}_{21} & \mathbf{B}_{22} \end{array} \right]$$

such that

$$\begin{aligned}
\mathbf{A}_{11} &= \mathbf{A}_1 - \mathbf{B}_1^e \Gamma \left(\mathbf{C}_1^f \mathbf{A}_1 - \mathbf{C}_2^f \mathbf{A}_2 \mathbf{H}_1^T \mathbf{C}_1^{zcom} \right) \\
\mathbf{A}_{12} &= \mathbf{B}_1^e \Gamma \mathbf{C}_2^f \mathbf{A}_2 \mathbf{H}_2^T \\
\mathbf{A}_{21} &= \mathbf{C}_2^{zind} \mathbf{A}_2 \mathbf{H}_1^T \mathbf{C}_1^{zcom} + \mathbf{C}_2^{zind} \mathbf{B}_2^e \Gamma \left(\mathbf{C}_1^f \mathbf{A}_1 - \mathbf{C}_2^f \mathbf{A}_2 \mathbf{H}_1^T \mathbf{C}_1^{zcom} \right) \\
\mathbf{A}_{22} &= \mathbf{C}_2^{zind} \mathbf{A}_2 \mathbf{H}_2^T - \mathbf{C}_2^{zind} \mathbf{B}_2^e \Gamma \mathbf{C}_2^f \mathbf{A}_2 \mathbf{H}_2^T
\end{aligned}$$

$$\begin{aligned}
\mathbf{B}_{11} &= \mathbf{B}_1^u - \mathbf{B}_1^e \Gamma \mathbf{C}_1^f \mathbf{B}_1^u \\
\mathbf{B}_{12} &= \mathbf{B}_1^e \Gamma \mathbf{C}_2^f \mathbf{B}_2^u \\
\mathbf{B}_{21} &= \mathbf{C}_2^{zind} \mathbf{B}_2^e \Gamma \mathbf{C}_1^f \mathbf{B}_1^u \\
\mathbf{B}_{22} &= \mathbf{C}_2^{zind} \mathbf{B}_2^u - \mathbf{C}_2^{zind} \mathbf{B}_2^e \Gamma \mathbf{C}_2^f \mathbf{B}_2^u
\end{aligned}$$

and the output matrix is given by

$$\mathbf{C} = \left[\begin{array}{cc} \mathbf{C}_1^z & 0_{nz_1 \times (ns_2 - n_c)} \\ \mathbf{C}_2^z \mathbf{H}_1^T \mathbf{C}_1^{zcom} & \mathbf{C}_2^z \mathbf{H}_2^T \end{array} \right].$$

$\mathbf{H}_1$ and $\mathbf{H}_2$ are partitioned matrices of $(\mathbf{C}_2^a)^{-1}$ such that

$$\begin{aligned}
\mathbf{x}_2 &= (\mathbf{C}_2^a)^{-1} \left\{ \begin{array}{c} \mathbf{z}_2^{com} \\ \mathbf{z}_2^{ind} \end{array} \right\} & (A.6) \\
&= \left[\begin{array}{cc} \mathbf{H}_1 & \mathbf{H}_2 \end{array} \right] \left\{ \begin{array}{c} \mathbf{z}_1^{com} \\ \mathbf{z}_2^{ind} \end{array} \right\} & (A.7) \\
&= \mathbf{H}_1 \mathbf{C}_1^{zcom} \mathbf{x}_1 + \mathbf{H}_2 \mathbf{z}_2^{ind}. & (A.8)
\end{aligned}$$

$\sim$

Appendix B

Mini-Manipulator Kinematics

This appendix derives kinematic relations used to calculate the outer-link angles, the Cartesian tip position relative to the mini-manipulator base, and the Jacobian of the mini-manipulator [27]. Various lengths and angles associated with the mini-manipulator are shown in Figure B.1.

B.1 Kinematic Constraints

The closed-kinematic chain configuration of the mini-manipulator imposes the following constraint equations:

$$L_1 u_{m1} s_1 + L_2 u_{m3} s_3 = L_1 u_{m2} s_2 + L_2 u_{m4} s_4 \tag{B.1}$$

$$L_1 u_{m1} c_1 + L_2 u_{m3} c_3 = L_1 u_{m2} c_2 + L_2 u_{m4} c_4 \tag{B.2}$$

where L_1, L_2, and q_{mi} are defined in Figure B.1,

$$s_i = \sin q_{mi} \tag{B.3}$$

$$c_i = \cos q_{mi} \tag{B.4}$$

and

$$u_{mi} = \dot{q}_{mi}. \tag{B.5}$$

Multiplying Equation (B.1) by c_4, Equation (B.2) by s_4, adding the resulting equations, and solving for u_{m3} yields

$$u_{m3} = \frac{L_1}{L_2} \frac{u_{m1} s_{14} - u_{m2} s_{24}}{s_{43}} \tag{B.6}$$

121
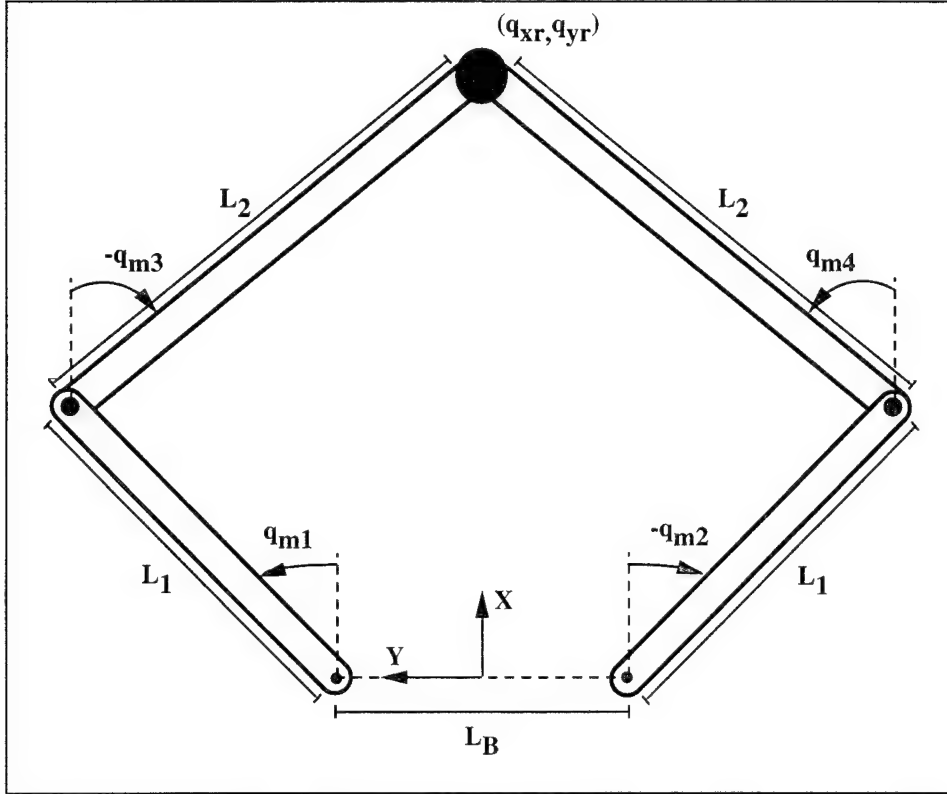
Figure B.1: **Mini-Manipulator Schematic**

Various lengths and angles associated with the mini-manipulator kinematics are shown in this figure.

where

$$s_{ij} = \sin\left(q_{mi} - q_{mj}\right). \tag{B.7}$$

Similarly, multiplying Equation (B.1) by c_3, Equation (B.2) by s_3, adding the resulting equations, and solving for u_{m4} yields

$$u_{m4} = \frac{L_1}{L_2} \frac{u_{m1}s_{13} - u_{m2}s_{23}}{s_{43}}. \tag{B.8}$$

B.2 Outer Joint Angles

Since only the inner motor angles are measured, the outer angles, q_{m3} and q_{m4}, must be calculated based on kinematic relationships. From the following relations:

$$d_1 = L_B + L_1 (s_1 - s_2) \tag{B.9}$$

$$d_2 = L_1 (c_2 - c_1) \tag{B.10}$$

$$d_3^2 = d_1^2 + d_2^2 \tag{B.11}$$

$$\alpha = \tan^{-1} \frac{d_1}{d_2} \tag{B.12}$$

$$\beta = 90 \deg - \alpha \tag{B.13}$$

$$L_2^2 = L_2^2 + d_3^2 - 2L_2 d_3 \cos (q_{M3} - \alpha), \tag{B.14}$$

expressions for q_{m3} and q_{m4} can be determined

$$q_{m3} = \cos^{-1} \frac{d_3}{2L_2} - \alpha \tag{B.15}$$

$$q_{m4} = 180 \deg - 2\alpha - q_{m3}. \tag{B.16}$$

The following sines and cosines of various angle combinations will be used in later calculations:

$$c_3 = \frac{d_1 d_4 + d_2}{2L_2} \tag{B.17}$$

$$s_3 = \frac{d_2 d_4 - d_1}{2L_2} \tag{B.18}$$

$$c_4 = \frac{d_1 d_4 - d_2}{2L_2} \tag{B.19}$$

$$s_4 = \frac{d_2 d_4 + d_1}{2L_2} \tag{B.20}$$

$$s_{43} = \frac{d_3^2}{2L_2^2} d_4 \tag{B.21}$$

where

$$d_4 = \sqrt{\frac{4L_2^2}{d_3^2} - 1}. \tag{B.22}$$

B.3 Cartesian Tip Position

Knowing the outside motor angles, the tip position of the mini-manipulator relative to the mini-manipulator reference frame is given by:

$$q_{xr} = L_1 c_1 + L_2 c_3$$

$$= L_1 c_1 + L_2 \frac{d_1 d_4 + d_2}{2L_2} \tag{B.23}$$

$$q_{yr} = \frac{L_B}{2} + L_1 s_1 + L_2 s_3$$

$$= \frac{L_B}{2} + L_1 s_1 + L_2 \frac{d_2 d_4 - d_1}{2L_2}. \tag{B.24}$$

B.4   Mini-Manipulator Jacobian

The Jacobian relates the motor velocities of the mini-manipulator to the tip velocity. It is defined by the equation

$$\begin{bmatrix} u_{xr} \\ u_{yr} \end{bmatrix} = \mathbf{J_m} \begin{bmatrix} u_{m1} \\ u_{m2} \end{bmatrix}. \tag{B.25}$$

Differentiating Equations (B.23) and (B.24) with respect to time produces

$$u_{xr} = -L_1 s_1 u_{m1} - L_2 s_3 u_{m3} \tag{B.26}$$

$$u_{yr} = L_1 c_1 u_{m1} + L_2 c_3 u_{m3}. \tag{B.27}$$

Substituting Equation (B.6) into this equation results in

$$u_{xr} = -L_1 \left(s_1 + \frac{s_3 s_{14}}{s_{43}} \right) u_{m1} \tag{B.28}$$

$$+ L_1 \frac{s_3 s_{24}}{s_{43}} u_{m2}$$

$$u_{yr} = L_1 \left(c_1 + \frac{c_3 s_{14}}{s_{43}} \right) u_{m1} \tag{B.29}$$

$$- L_1 \frac{c_3 s_{24}}{s_{43}} u_{m2}.$$

Therefore, by the definition of the Jacobian in Equation (B.25), the Jacobian of the mini-manipulator is

$$\mathbf{J_m} = \begin{bmatrix} -L_1 \left(s_1 + \frac{s_3 s_{14}}{s_{43}} \right) & L_1 \frac{s_3 s_{24}}{s_{43}} \\ L_1 \left(c_1 + \frac{c_3 s_{14}}{s_{43}} \right) & -L_1 \frac{c_3 s_{24}}{s_{43}} \end{bmatrix}. \tag{B.30}$$

B.5   Inverse Kinematics

The inverse kinematics of the mini-manipulator were derived following the method described in [50]. Defining

$$\rho_1 = q_{m3} - q_{m1} \tag{B.31}$$

$$\rho_2 = q_{m4} - q_{m2}, \tag{B.32}$$

the relative mini-manipulator tip position can be expressed as follows:

$$q_{xr} \;=\; L_1 c_1 + L_2 \cos(q_{m1} + \rho_1) \tag{B.33}$$

$$q_{yr} \;=\; L_1 s_1 + L_2 \sin(q_{m1} + \rho_1) + \frac{L_B}{2}. \tag{B.34}$$

Squaring and adding Equations (B.33) and (B.34) yields

$$\cos(\rho_1) = \frac{q_{xr}^2 + (q_{yr} - \frac{L_B}{2})^2 - L_1^2 - L_2^2}{2 L_1 L_2}. \tag{B.35}$$

Assuming that q_{xr} and q_{yr} are within the workspace of the mini-manipulator, ρ_1 can be determined from the expression

$$\rho_1 = \tan^{-1} \frac{\sin(\rho_1)}{\cos(\rho_1)} \tag{B.36}$$

where

$$\sin(\rho_1) = -\sqrt{1 - \cos^2(\rho_1)}. \tag{B.37}$$

Having solved for ρ_1, q_{m1} is given as

$$q_{m1} = \tan^{-1} \frac{q_{yr} - \frac{L_B}{2}}{q_{xr}} - \tan^{-1} \frac{k_2}{k_1} \tag{B.38}$$

where

$$k_1 \;=\; L_1 + L_2 \cos(\rho_1) \tag{B.39}$$

$$k_2 \;=\; L_2 \sin(\rho_2). \tag{B.40}$$

q_{m2} can be determined following the same procedure.

$\sim$

Appendix C

Modelling the Flexible Links

The State-Space Model Concatenation Method requires models of the flexible links in the form

$$
\begin{aligned}
\dot{\mathbf{x}}_i &= \mathbf{A}_i\mathbf{x}_i + \mathbf{B}_i^u\mathbf{u}_i(t) + \mathbf{B}_i^e\mathbf{e}_i \\
\mathbf{z}_i &= \mathbf{C}_i^z\mathbf{x}_i \\
\mathbf{f}_i &= \mathbf{C}_i^f\mathbf{x}_i \\
\mathbf{d}_i &= \mathbf{C}_i^d\mathbf{x}_i
\end{aligned}
\tag{C.1}
$$

where the dimensions for subsystem i, $i = 1, 2$, are specified as the state vector $\mathbf{x}_i \in \mathbb{R}^{ns_i}$, external input vector $\mathbf{u}(t)_i \in \mathbb{R}^{nu_i}$, internal effort vector at the interface $\mathbf{e}_i \in \mathbb{R}^{ne_i}$, monitored output vector $\mathbf{z}_i \in \mathbb{R}^{nz_i}$, internal flow vector at the interface $\mathbf{f}_i \in \mathbb{R}^{nf_i}$, and internal displacement vector at the interface $\mathbf{d}_i \in \mathbb{R}^{nd_i}$, with $\mathbf{A}_i$, $\mathbf{B}_i^u$, $\mathbf{B}_i^e$, $\mathbf{C}_i^z$, $\mathbf{C}_i^f$, and $\mathbf{C}_i^d$ having consistent dimensions.

The approach used to develop these subsystem models involved a four-step process. First, finite-element subsystem models of the flexible links were developed. Second, these subsystem models were converted to modal form. Third, model reduction on the subsystem models was performed. Fourth, the resulting reduced-order subsystem models were converted to the state-space form of Equation (C.1). The following sections detail the four steps of this process.

127

C.1   Finite-Element Models

Using the finite-element modelling approach, subsystem models of the links were developed
of the form

$$\mathbf{M}_i\ddot{\mathbf{q}}_i(t) + \mathbf{K}_i\mathbf{q}_i(t) = \mathbf{Q}_i^u\mathbf{u}_i + \mathbf{Q}_i^e\mathbf{e}_i \tag{C.2}$$

where $\mathbf{M}_i$ is the symmetric $n \times n$ mass or inertia matrix, $\mathbf{K}_i$ is the symmetric $n \times n$ stiffness
matrix, and $\mathbf{q}_i(t)$ is an n-dimensional vector of time-dependent generalized coordinates
which completely describe the motion of the subsystem. The subsystem output $\mathbf{z}_i$ and
displacement at the interface $\mathbf{d}_i$ are of the form

$$\mathbf{z}_i = \mathbf{T}_i^z\mathbf{q}_i(t) \tag{C.3}$$

$$\mathbf{d}_i = \mathbf{T}_i^d\mathbf{q}_i(t). \tag{C.4}$$

C.2   Modal Form

Converting the subsystem model in Equation (C.2) to modal form requires first solving the
generalized eigenvalue problem corresponding to the $\mathbf{M}_i$ and $\mathbf{K}_i$ matrices of Equation (C.2)

$$\mathbf{K}_i\mathbf{\Psi}_{i_j} = \omega_{i_j}^2\mathbf{M}_i\mathbf{\Psi}_{i_j} \qquad j = 1, 2, \dots, n \tag{C.5}$$

where the ω_{i_j} are the natural frequencies of subsystem i, and the $\mathbf{\Psi}_{i_j}$ are the corresponding
eigenvectors which represent physically the subsystem natural modes or mode shapes.

By virtue of the expansion theorem [37], any possible motion of the system can be
represented as a linear combination of the system mode shapes. Thus, at any time t, the
vector of generalized coordinates describing the motion may be represented by a linear
combination of the $\mathbf{\Psi}_{i_j}$ with coefficients $m_{i_j}(t)$

$$\mathbf{q}_i(t) = m_{i_1}(t)\mathbf{\Psi}_{i_1} + m_{i_2}(t)\mathbf{\Psi}_{i_2} + \cdots + m_{i_n}(t)\mathbf{\Psi}_{i_n}. \tag{C.6}$$

In matrix form, Equation (C.6) can be written as

$$\mathbf{q}_i(t) = \mathbf{\Psi}_i\mathbf{m}_i(t) \tag{C.7}$$

where the columns of the modal matrix $\mathbf{\Psi}_i$ are the system mode shapes, and $\mathbf{m}_i(t)$ is a
vector containing the coefficients $m_{i_j}(t)$. For time-invariant systems, the modal matrix is a
constant. As a result, it immediately follows from Equation (C.7) that

$$\ddot{\mathbf{q}}_i(t) = \mathbf{\Psi}_i\ddot{\mathbf{m}}_i(t). \tag{C.8}$$

If the coefficients of Equation (C.6) are defined as

$$\mathbf{m}_i(t) = \mathbf{\Psi}_i^T \mathbf{M}_i \mathbf{q}_i(t) \tag{C.9}$$

and the system mode shapes are orthonormal and normalized such that

$$\mathbf{\Psi}_{i_k}^T \mathbf{M}_i \mathbf{\Psi}_{i_j} = \delta_{kj} \qquad k, j = 1, 2, \ldots, n \tag{C.10}$$

then

$$\mathbf{\Psi}_{i_j}^T \mathbf{K}_i \mathbf{\Psi}_{i_j} = \omega_{i_j}^2 \qquad j = 1, 2, \ldots, n. \tag{C.11}$$

Substituting Equations (C.7) and (C.8) into Equation (C.2) yields

$$\mathbf{M}_i \mathbf{\Psi}_i \ddot{\mathbf{m}}_i(t) + \mathbf{K}_i \mathbf{\Psi}_i \mathbf{m}_i(t) = \mathbf{Q}_i^u \mathbf{u}_i + \mathbf{Q}_i^e \mathbf{e}_i \tag{C.12}$$

Due to the normalization in Equation (C.10), premultiplying Equation (C.12) by $\mathbf{\Psi}^T$ yields a set of independent equations

$$\ddot{\mathbf{m}}_i(t) + \omega_i^2 \mathbf{m}_i(t) = \mathbf{\Psi}_i^{\mathrm{T}} \mathbf{Q}_i^u \mathbf{u}_i + \mathbf{\Psi}_i^{\mathrm{T}} \mathbf{Q}_i^e \mathbf{e}_i \tag{C.13}$$

where ω_i^2 is an $n \times n$ matrix with diagonal elements $\omega_{i_j}^2$, and the $m_{i_j}(t)$ are known as normal or modal coordinates. The corresponding subsystem outputs $\mathbf{z}_i$ and displacements $\mathbf{d}_i$ are given as

$$\begin{aligned}
\mathbf{z}_i &= \mathbf{T}_i^z \mathbf{\Psi}_i \mathbf{m}_i(t) \tag{C.14} \\
\mathbf{d}_i &= \mathbf{T}_i^d \mathbf{\Psi}_i \mathbf{m}_i(t). \tag{C.15}
\end{aligned}$$

The Damping Matrix   The experimental system contains inherent damping. As a result, it is necessary to include damping in the model. Damping is incorporated by assuming a damping ratio for each mode. The modal damping ratios are often determined experimentally. The modal damping matrix $\mathbf{C}_i^{modal}$ is given by

$$\mathbf{C}_i^{modal} = \mathrm{diag} \begin{bmatrix} 0 & 2\zeta_{i_1}\omega_{i_1} & 2\zeta_{i_2}\omega_{i_2} & \ldots & 2\zeta_{i_n}\omega_{i_n} \end{bmatrix} \tag{C.16}$$

where ζ_{i_j} are the assumed modal damping ratios.

The resulting modal equations of motion are

$$\ddot{\mathbf{m}}_i(t) + \mathbf{C}_i^{modal} \dot{\mathbf{m}}_i(t) + \omega_i^2 \mathbf{m}_i(t) = \mathbf{\Psi}_i^{\mathrm{T}} \mathbf{Q}_i^u \mathbf{u}_i + \mathbf{\Psi}_i^{\mathrm{T}} \mathbf{Q}_i^e \mathbf{e}_i. \tag{C.17}$$

C.3   Model Reduction

Typically, the number of generalized coordinates in the finite-element model is significantly greater than the number of system modes needed to accurately represent the system for the purposes of control. Consequently, it is necessary to develop a reduced-order model. Model reduction is accomplished by simply truncating high-frequency modes from the model describe in Equation (C.17).

C.4   State-Space Form

Given a model of the form of Equation (C.17) (or its reduced-order equivalent), the state-space model is given by

$$
\begin{aligned}
\dot{\mathbf{x}}_i &= \mathbf{A}_i\mathbf{x}_i + \mathbf{B}_i^u\mathbf{u}_i + \mathbf{B}_i^e\mathbf{e}_i \\
\mathbf{z}_i &= \mathbf{C}_i^z\mathbf{x}_i \\
\mathbf{f}_i &= \mathbf{C}_i^f\mathbf{x}_i \\
\mathbf{d}_i &= \mathbf{C}_i^d\mathbf{x}_i
\end{aligned}
\tag{C.18}
$$

where

$$
\mathbf{x}_i = \begin{bmatrix} \mathbf{m}_i \\ \dot{\mathbf{m}}_i \end{bmatrix}
\tag{C.19}
$$

$$
\mathbf{A}_i = \begin{bmatrix} \mathbf{0} & \mathbf{I} \\ -\boldsymbol{\omega}_i^2 & -\mathbf{C}_i^{modal} \end{bmatrix}
\tag{C.20}
$$

$$
\mathbf{B}_i^u = \begin{bmatrix} \mathbf{0} \\ \boldsymbol{\Psi}_i^{\mathrm{T}}\mathbf{Q}_i^u \end{bmatrix}
\tag{C.21}
$$

$$
\mathbf{B}_i^e = \begin{bmatrix} \mathbf{0} \\ \boldsymbol{\Psi}_i^{\mathrm{T}}\mathbf{Q}_i^e \end{bmatrix}
\tag{C.22}
$$

$$
\mathbf{z}_i = \begin{bmatrix} \mathbf{T}_i^z\boldsymbol{\Psi}_i & \mathbf{0} \end{bmatrix}
\tag{C.23}
$$

$$
\mathbf{d}_i = \begin{bmatrix} \mathbf{T}_i^d\boldsymbol{\Psi}_i & \mathbf{0} \end{bmatrix}
\tag{C.24}
$$

$$
\mathbf{f}_i = \begin{bmatrix} \mathbf{0} & \mathbf{T}_i^d\boldsymbol{\Psi}_i \end{bmatrix}.
\tag{C.25}
$$

Appendix D

Terminal Controllers

This appendix gives a brief background of other applications involving terminal controllers. Also included is an example problem to illustrate the performance advantages introduced by the time-varying gains of the terminal controller and the solution to the terminal controller problem. This solution is described in detail in [46].

D.1   Background

Terminal controllers have been used in a number of applications where the controller requirements are similar to the requirements for the rapid repositioning of multi-link flexible manipulators. The idea was first introduced in [51] where time-varying gains were used to obtain optimal-state estimates in the presence of white noise. It was also pointed out in [51] that because of the duality between the optimal-estimation and optimal-regulation problems, time-varying feedback gains are also the solution of the optimal-regulation problem with a specified final time. Since then, terminal controllers with time-varying gains have been implemented to solve a number of control problems where terminal constraints are present. For example, the guidance system of the Saturn launch vehicle utilized time-varying feedback gains to calculate the optimum thrust direction for minimum-propellant consumption to meet the required end conditions for the flight vehicle [52]. Similarly, [53] discusses the application of time-varying gains to the Mars entry problem where the goal of the controller was to minimize errors in a set of pre-specified terminal conditions in the resence of atmospheric density uncertainties. [46] gives an example in which time-varying

estimator and controller feedback gains are shown to be the optimal solution of the missile intercept guidance problem with random target acceleration.

D.2   Performance Advantages

The performance benefits of this trajectory generation approach stem from the time-varying feedback gains of the terminal controller. To illustrate the performance advantages of terminal controllers over constant-gain controllers, consider the first-order system described by

$$\dot{x} \;=\; -ax + u \tag{D.1}$$

where x, a, and u are scalars, and $x(t_0) = x_0$ is given. The goal is to design a controller which will bring the state from x_0 to a final state, $x(t_f) = x_f$, within a specified final time, t_f, while using a reasonable amount of control. An intuitive approach to solving this problem is to formulate a performance index as in Equation (4.2)

$$J = S_f x(t_f)^2 + \int_{t_0}^{t_f} u(t)^2 dt. \tag{D.2}$$

In Equation (D.2), the scalars $Q_x(t)$ and $Q_u(t)$ have been set to zero and one respectively. Minimizing Equation (D.2) while at the same time satisfying the constraint imposed by Equation (D.1) results in a time-varying feedback gain $K_{TV}(t)$, and the control law

$$u_{TV}(t) = -K_{TV}(t)x(t), \tag{D.3}$$

Now, for purposes of comparison and to isolate the effects of time-varying gains, consider the design of a constant-gain controller defined as:

$$u_{TI}(t) = -K_{TI}x(t), \tag{D.4}$$

where K_{TI} is a constant feedback gain. Substituting Equation (D.4) into Equation (D.1) results in a first-order, linear, homogeneous differential equation in x

$$\dot{x} = -(a + K_{TI})x, \tag{D.5}$$

which has the solution

$$x(t) = x_0 e^{-(a+K_{TI})t}. \tag{D.6}$$

Substituting Equation (D.6) into Equation (D.2) yields

$$J = S_f x_0^2 e^{-2(a+K_{TI})t_f} + \frac{K_{TI}^2 x_0^2}{2(a+K_{TI})} \left[1 - e^{-2(a+K_{TI})t_f} \right], \tag{D.7}$$

Setting the partial derivative of Equation (D.7) with respect to K_{TI} equal to zero, and then using an iterative scheme to solve for K_{TI} will yield the constant feedback gain K_{TI} which minimizes Equation (D.2) while at the same time satisfying the constraint in Equation (D.1).

For the case $a = 1$, $t_f = 1$, and $S_f = 100$, the response of the first-order system for both
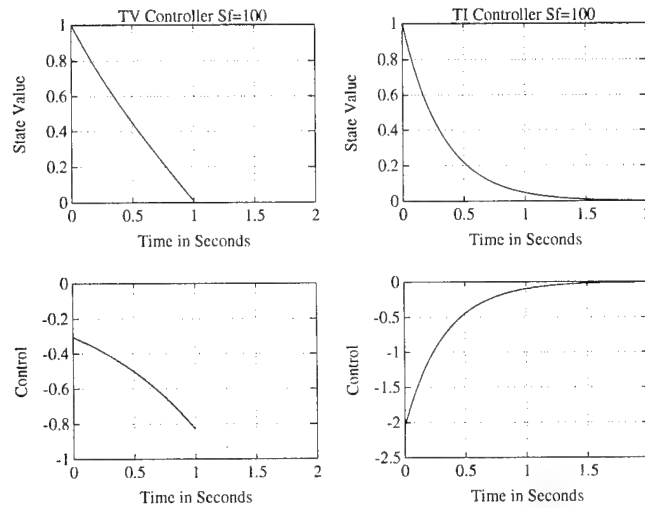
Figure D.1: **TV Controller vs. TI Controller**

Response of the first-order system for both time-varying (TV) and time-invariant (TI) feedback gains. The TV controller brings the state to its desired terminal value while the TI controller is incapable of meeting the terminal constraint

the time-varying and time-invariant controllers is shown in Figure D.1. From Figure D.1 it is evident that while using less peak control effort, the TV controller is able to bring the system to the desired terminal state, at the desired final time, while the TI controller is incapable of meeting the terminal constraints.

Figure D.2 is a plot of the time-varying feedback gain as a function of time. The gain increases exponentially as t approaches the final time t_f. As a result, as the state error decreases, the TV controller is still able to output a sufficient control to quickly bring the state to zero. The TI controller, on the other hand, outputs initially a large control when the state error is largest. As the state error decreases, so does the output of the TI controller. As
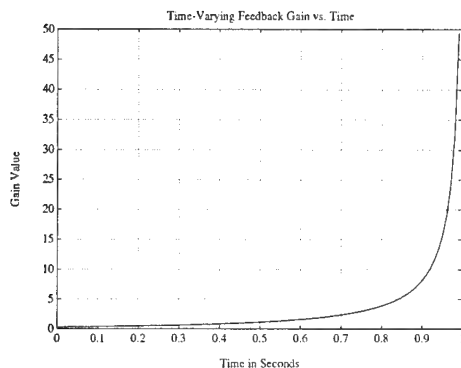
Figure D.2: **TV Feedback Gain vs. Time**

This figure illustrates how the time-varying feedback gain varies with time for the first-order system. Because the feedback gain increases as the state error decreases, the controller is capable of generating a sufficient control signal to meet the terminal constraint.

a result, the TI controller is only able to bring the system asymptotically close to the desired terminal state. Finally, for the responses shown in Figure D.2, the TV controller yields a lower value of J ($J(K_{TV}) = 29.9$) than the TI controller ($J(K_{TI}) = 71.0$), and therefore, the TV controller is a better controller for the performance index of Equation (D.2).

Advantages   As illustrated by this example, the time-varying gains of the terminal controller result in two advantages over a constant-gain controller:

1. The terminal controller yields less terminal-state error.

2. The terminal controller offers improved performance with less peak control effort.

D.3   Terminal-Controller Solution

The terminal controller problem is to minimize a cost function of the form:

$$\mathbf{J} \;\; = \;\; \frac{1}{2}(\mathbf{x}^{\mathrm{T}}\mathbf{S}_f\mathbf{x})_{t=t_f} + \frac{1}{2}\int_{t_0}^{t_f}[\mathbf{x}^{\mathrm{T}}\mathbf{Q}_x(t)\mathbf{x} + \mathbf{u}^{\mathrm{T}}\mathbf{Q}_u(t)\mathbf{u}]dt, \qquad\qquad (\text{D.8})$$

subject to the linear constraints imposed by

$$\dot{\mathbf{x}}(t) \;\; = \;\; \mathbf{A}\mathbf{x}(t) + \mathbf{B}\mathbf{u}(t), \qquad\qquad (\text{D.9})$$

In Equation D.8), $\mathbf{S}_f$ and $\mathbf{Q}_x(t)$ are positive semidefinite matrices which weight the values of the states at the terminal time $\mathbf{x}(t_f)$ and the values of the intermediate states $\mathbf{x}(t)$, and $\mathbf{Q}_u(t)$ is a positive definite matrix which weights the control effort $\mathbf{u}$ expended during the slew. Equation (D.8) is written for the case where the desired terminal state is zero.

Using methods described in [46], we can solve for the control input $\mathbf{u}(t)$ that will minimize Equation (4.2) by simultaneously solving the linear constraints in Equation (D.9) and the following Euler-Lagrange equations:

$$\dot{\lambda}^{\mathrm{T}} = -\frac{\partial \mathbf{H}}{\partial \mathbf{x}}, \tag{D.10}$$

$$\frac{\partial \mathbf{H}}{\partial \mathbf{u}} = 0, \tag{D.11}$$

where

$$\mathbf{H} = \frac{1}{2}\mathbf{x}^{\mathrm{T}}\mathbf{Q}_x\mathbf{x} + \frac{1}{2}\mathbf{u}^{\mathrm{T}}\mathbf{Q}_u\mathbf{u} + \lambda^{\mathrm{T}}(\mathbf{A}\mathbf{x} + \mathbf{B}\mathbf{u}), \tag{D.12}$$

$$\lambda(t_f) = \mathbf{S}_f\mathbf{x}(t_f), \tag{D.13}$$

and λ is a vector of undetermined Lagrange multipliers. Performing the differentiations specified in Equations (D.11) and (D.11) results in the following linear two-point boundary-value problem:

$$\begin{bmatrix} \dot{\mathbf{x}} \\ \dot{\lambda} \end{bmatrix} = \begin{bmatrix} \mathbf{A} & -\mathbf{B}\mathbf{Q}_u^{-1}\mathbf{B}^{\mathrm{T}} \\ -\mathbf{Q}_x & -\mathbf{A}^{\mathrm{T}} \end{bmatrix} \begin{bmatrix} \mathbf{x} \\ \lambda \end{bmatrix}, \tag{D.14}$$

where

$$\lambda(t_f) = \mathbf{S}_f\mathbf{x}(t_f), \tag{D.15}$$

and $\mathbf{x}(t_0)$ is given.

Problem Solution

There are a number of methods by which the two-point boundary-value problem of Equations (D.14) and (D.15) can be solved. The backward sweep method is described here because of its direct application to solving the discrete-time terminal controller problem which is useful for real-time implementation.

Since the two-point boundary-value problem is linear and homogeneous, $\lambda(t)$ will be proportional to $\mathbf{x}(t_0)$. Therefore, defining

$$\lambda(t) \;=\; \mathbf{S}(t)\mathbf{x}(t), \tag{D.16}$$

and substituting Equation (D.16) into Equation (D.14) yields the matrix Riccati equation

$$\dot{\mathbf{S}} \;=\; -\mathbf{S}\mathbf{A} - \mathbf{A}^{\mathrm{T}}\mathbf{S} + \mathbf{S}\mathbf{B}\mathbf{Q}_u^{-1}\mathbf{B}^{\mathrm{T}}\mathbf{S} - \mathbf{Q}_x, \tag{D.17}$$

which is quadratic in $\mathbf{S}$. Equation (D.17) can be integrated backward from from the specified terminal time $\mathbf{t}_f$ to the initial time $\mathbf{t}_0$ to solve for $\mathbf{S}(t)$. Once $\mathbf{S}(t)$ has been found, the continuous control law and time-varying feedback gains can be calculated. Substituting Equation (D.16) into the result of Equation (D.11), the following feedback law for terminal control can be calculated:

$$\mathbf{u}(t) \;=\; -\mathbf{K}(t)\mathbf{x}(t), \tag{D.18}$$

$$\mathbf{K}(t) \;=\; \mathbf{Q}_u(t)^{-1}\mathbf{B}^{\mathrm{T}}(t)\mathbf{S}(t), \tag{D.19}$$

where $\mathbf{K}(t)$ is the optimally determined time-varying feedback gain.

Discrete-Time Solution

As mentioned in Section D.3, for real-time implementation, it is useful to formulate and solve the terminal controller problem in the discrete-time domain. Given the discretized linear constraint equations

$$\mathbf{x}(k+1) \;=\; \Phi\mathbf{x}(k) + \Gamma\mathbf{u}(k), \tag{D.20}$$

$$\tag{D.21}$$

where $k = 0, 1, \ldots, N$ and Φ and Γ are the discrete system matrices, the discrete-time terminal controller problem is to minimize the performance index

$$\begin{aligned}
\mathbf{J} \;=\; & \frac{1}{2}\mathbf{x}^{\mathrm{T}}(N)\mathbf{S}_f\mathbf{x}(N) + \\
& \frac{1}{2}\sum_{k=1}^{N}\mathbf{x}^{\mathrm{T}}(k)\mathbf{Q}_{xd}(k)\mathbf{x}(k) + \\
& \frac{1}{2}\sum_{k=0}^{N-1}\mathbf{u}^{\mathrm{T}}(k)\mathbf{Q}_{ud}(k)\mathbf{u}(k),
\end{aligned} \tag{D.22}$$

subject to the linear constraints imposed by Equation (D.21). Equation (D.22) is written for the case where the desired terminal state is zero.

In many applications, the value of the intermediate state is not important, and $\mathbf{Q}_{xd}(k)$ is set equal to zero for all k. This specification results in a terminal controller which attempts to bring the state to zero in a given number of time steps N with minimum control energy (or minimum integral-square control in the continuous case). Using a backward sweep algorithm, the solution when $\mathbf{Q}_{xd}(k) = 0$ is given in [54] as

$$\psi(k) \quad = \quad \left[\mathbf{Q}_{ud}(k) + \Gamma^{\mathrm{T}} \mathbf{S}(k+1)\Gamma \right]^{-1} \tag{D.23}$$

$$\mathbf{K}(k) \quad = \quad \psi(k)\Gamma^{\mathrm{T}}\mathbf{S}(k+1), \tag{D.24}$$

$$\mathbf{S}(k) \quad = \quad \Phi^{\mathrm{T}} \left[\mathbf{I} - \Gamma\mathbf{K}(k) \right]^{\mathrm{T}} \mathbf{S}(k+1)\Phi, \tag{D.25}$$

where $\mathbf{I}$ is the $n \times n$ identity matrix. Since $\mathbf{S}_f$ is specified by the designer, Equations (D.23), (D.24), and (D.25) can be swept backward to calculate the optimal feedback gain $\mathbf{C}(k)$ at each time step.

D.4 Software

To compute the terminal-controller solution, the following MATLAB file was developed.

```
function [K1,K2] = backwardSweep(F,G,Sf,Qx,Qu,Ts,Tf)
% Matlab.m file for discrete smoother-follower problem as a TPBVP.
% Calculates  terminal-controller time-varying gains.
%
% Assumed plant form:
% xdot = Fx + Gu;
%
% Sample time is Ts;
%
% Final time is Tf;
%
% Solves for terminal controller assuming the following
% performance index:
% J=x(N)'*Sf*x(N) + Integral (0 to tf) [x'*Qx*x + u'*Qu(t)*u]dt;
%
```

```
% Includes a time weighting on Qu(t) given by:
% if k >= .8*(tf/Ts) + (to+Ts)/Ts
% rho = (k-.8*(tf/Ts) + (to+Ts)/Ts)^2;
% else
% rho = 1;
% end
%
%
% Written by Bill Ballhaus
% 12-20-91

% Total number of steps
Nn = tf/Ts;

% System size
[ns,ns]=size(F);
[ns,ni]=size(ga);

% Conversion to discrete domain
[phi,ga]=c2d(F,G,Ts);

% Conversion of weighting matrices
Qud = Qu/Ts;
Qxd = Qx/Ts;
Sbar = Sf/Ts;


% Backward sweep to calculate feedback gain at each step
for k=Nn+(to+Ts)/Ts:-1:(to+Ts)/Ts,

% Compute time weighting on control
if k >= .8* Nn + (to+Ts)/Ts
rho = (k-.8*Nn +(to+Ts)/Ts)^2;
```

```
else
rho = 1;
end


% Gain calculation
Shat = Sbar + Qxd;
reg_gains=inv(rho*Qud*eye(ni)+ga'*Shat*ga)*(ga'*Shat);
K1(k,:)=reg_gains(1,:)*phi;
K2(k,:)=reg_gains(2,:)*phi;
Sbar=phi'*(eye(ns)-ga*reg_gains)'*Shat*phi;

end
```

$\sim$

140

Appendix E

Estimator Design

The control approach presented in Chapter 5 requires full knowledge of the state. Since all states of the system cannot be measured, an estimator is needed. This appendix presents the estimator design for the experimental two-link flexible manipulator with the mini-manipulator at its tip.

E.1 Design Approach

The estimator-design approach consists of an LQG design with a nonlinear output equation. The design is based on the model of the main arm developed in Chapter 3 for a ninety degree elbow angle. The system is assumed to be of the form

$$\dot{\mathbf{x}}(t) \;=\; \mathbf{A}\mathbf{x}(t) + \mathbf{B}\mathbf{u}(t) + \mathbf{B}\mathbf{w}(t) \tag{E.1}$$

$$\mathbf{y}_s(t) \;=\; \mathbf{C}_s\mathbf{x}(t) + \mathbf{v}(t) \tag{E.2}$$

where $\mathbf{x}(t)$ is the state vector, $\mathbf{A}$ is the state transition matrix, $\mathbf{B}$ is the input matrix, $\mathbf{u}(t)$ is the control vector, $\mathbf{y}_s(\mathrm{t})$ is a vector of sensed outputs, $\mathbf{C}_s$ is the output matrix, and the process noise $\mathbf{w}(t)$ and measurement noise $\mathbf{v}(t)$ covariances are given by

$$\mathrm{E}[\mathbf{w}(t)] \;=\; \mathbf{0} \tag{E.3}$$

$$\mathrm{E}[\mathbf{v}(t)] \;=\; \mathbf{0} \tag{E.4}$$

$$\mathrm{E}[\mathbf{w}(t)\mathbf{w}^{\mathrm{T}}(t')] \;=\; \mathbf{R}_w\delta(t - t') \tag{E.5}$$

$$\mathrm{E}[\mathbf{v}(t)\mathbf{v}^{\mathrm{T}}(t')] \;=\; \mathbf{R}_v\delta(t - t') \tag{E.6}$$

$$\mathrm{E}[\mathbf{w}(t)\mathbf{v}^{\mathrm{T}}(t')] \;=\; \mathbf{0}. \tag{E.7}$$

141

The sensed outputs of the experimental main arm are

$$\mathbf{y}_s \;=\; \begin{bmatrix} X_{tip} \\ Y_{tip} \\ \theta_{tip} \\ \dot{\theta}_1 \\ \dot{\theta}_2 \end{bmatrix} \tag{E.8}$$

where X_{tip}, Y_{tip}, and θ_{tip} are the position and orientation of the vision target mounted at the tip of the flexible main arm, and θ_i is the output of the RVDT located at the ith joint.

The state estimate $\hat{\mathbf{x}}$ is given by

$$\dot{\hat{\mathbf{x}}}(t) \;=\; \mathbf{A}\hat{\mathbf{x}}(t) + \mathbf{B}\mathbf{u}(t) + \mathbf{L}\left(\mathbf{y}_s(t) - \hat{\mathbf{y}}(t)\right) \tag{E.9}$$

where $\hat{\mathbf{y}}(t)$ is the estimate of the output and $\mathbf{L}$ is the estimator-gain matrix. The gain matrix is a function of the process and measurement noise properties. Consequently, $\mathbf{R}_w$ and $\mathbf{R}_v$ provide a design mechanism for specifying how much the estimates depend on the model and the sensor output.

For the two-link flexible manipulator, the estimate of the output is actually a nonlinear function such that

$$\hat{\mathbf{y}}(t) \;=\; \mathbf{C}_s(\mathbf{x}(t)). \tag{E.10}$$

This function is given in [5].

E.1.1   Coloring the Noise Spectrum

The measurements corresponding to the end-point position and orientation provide redundant DC information. As a result, in steady state, there is a bias on the state estimate if these three signals do not correspond exactly. Thus, a mechanism is needed to vary the influence a sensor has on the estimator as a function of frequency. To do this, a technique developed by Larry Alder was used which requires coloring the noise spectrum on the sensor noise. [9] details the solution to the colored-noise estimation problem.

E.1.2   Modelling Sensor Delay

The measurments provided by the vision sensor are delayed by approximately two sample periods. The sensor delay can be modelled easily in the discrete domain [55]. The delayed

measurements $\mathbf{y}_{delay}$ are given by

$$\mathbf{y}_{delay} \quad = \quad \begin{bmatrix} X_{tip} \\ Y_{tip} \\ \theta_{tip} \end{bmatrix} = \mathbf{C}_{s_{delay}} \tag{E.11}$$

and the non-delayed (current) measurements are given by

$$\mathbf{y}_{cur} \quad = \quad \begin{bmatrix} \dot{\theta}_1 \\ \dot{\theta}_2 \end{bmatrix} = \mathbf{C}_{s_{cur}}. \tag{E.12}$$

For each sample period of delay, a new set of delay states is augmented to the original plant state. For the two sample period delay associated with the vision system, the resulting discrete system matrices are given by

$$\mathbf{x}_a \quad = \quad \begin{bmatrix} \mathbf{x} \\ \mathbf{y}_{delay}(k-1) \\ \mathbf{y}_{delay}(k-2) \end{bmatrix} \tag{E.13}$$

$$\mathbf{A}_a \quad = \quad \begin{bmatrix} \mathbf{A}_d & \mathbf{0} & \mathbf{0} \\ \mathbf{C}_{s_{delay}} & \mathbf{0} & \mathbf{0} \\ \mathbf{0} & \mathbf{I} & \mathbf{0} \end{bmatrix} \tag{E.14}$$

$$\mathbf{B}_a \quad = \quad \begin{bmatrix} \mathbf{B}_d & \mathbf{0} & \mathbf{0} \end{bmatrix} \tag{E.15}$$

$$\mathbf{C}_{s_a} \quad = \quad \begin{bmatrix} \mathbf{0} & \mathbf{0} & \mathbf{I} \\ \mathbf{C}_{s_{cur}} & \mathbf{0} & \mathbf{0} \end{bmatrix}. \tag{E.16}$$

Using these matrices, the estimator is designed in the discrete domain with no required modifications to the noise spectra.

E.2 Estimator Design

The estimator was designed by varying $\mathbf{R}_v$ and $\mathbf{R}_w$ until acceptable estimator closed-loop roots were obtained. The noise covariances used were

$$\mathbf{R}_w \quad = \quad \begin{bmatrix} .0001 \ (\text{N-m})^2 & 0 \\ 0 & .0001 \ (\text{N-m})^2 \end{bmatrix} \tag{E.17}$$

$$\mathbf{R}_v \;\; = \;\; \begin{bmatrix} .001 \text{ m}^2 \\ .001 \text{ m}^2 \\ .0000002 \text{ (rad)}^2 \\ .000001 \text{ (rad/sec.)}^2 \\ .000001 \text{ (rad/sec.)}^2 \end{bmatrix} . \tag{E.18}$$

In addition, the noise spectrum on the tip-orientation sensor was colored with a first-order filter with a 3 Hz break frequency (shown in Figure E.1).   The closed-loop roots corre-
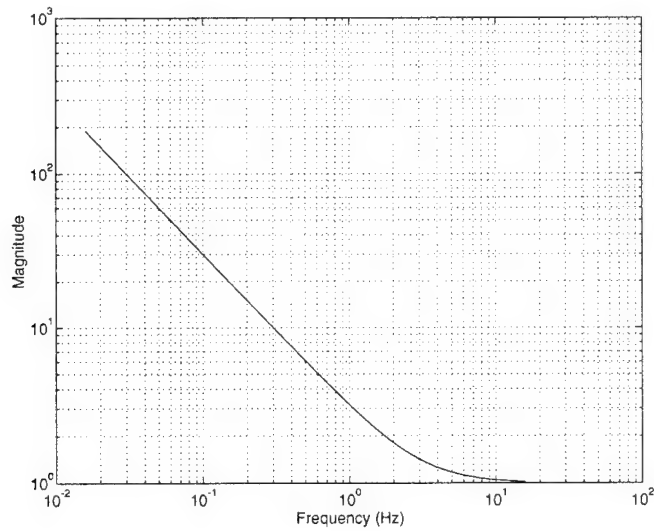
Figure E.1: **Coloring the Tip-Orientation Noise Covariance**

This figure shows how the noise spectrum on the tip-orientation sensor was colored to avoid a bias in the state estimates. This filter is a first-order filter with a 3 Hz break frequency.

sponding to these design parameters are given in Figure E.2.
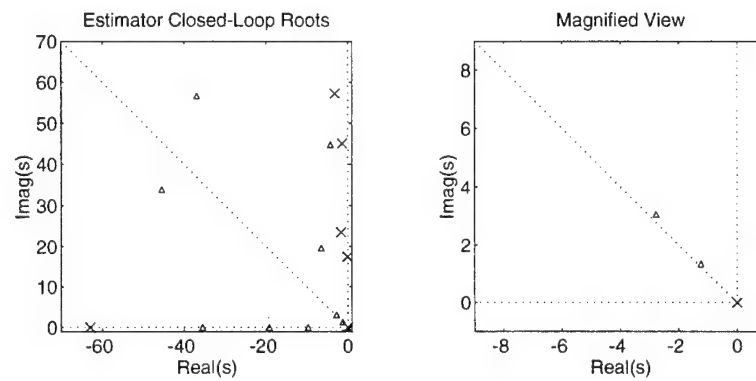
Figure E.2: **Estimator Closed-Loop Roots**

*This figure shows the estimator closed-loop roots. The closed-loop roots are repre-sented by the △'s, while the **x**'s represent the open-loop roots.*

$\sim$

146

Appendix F

Model and Gain Matrices

F.1 Main Arm

F.1.1 Model

The model of the main arm is given by

$$\dot{\mathbf{x}} = \mathbf{A}\mathbf{x} + \mathbf{B}\mathbf{u} \tag{F.1}$$

$$\mathbf{y}_s = \mathbf{C}_s\mathbf{x} \tag{F.2}$$

$$\mathbf{y}_c = \mathbf{C}_c\mathbf{x} \tag{F.3}$$

where the sensed outputs are

$$\mathbf{y}_s = \begin{bmatrix} X_{tip} \\ Y_{tip} \\ \theta_{tip} \\ \dot{\theta}_1 \\ \dot{\theta}_2 \end{bmatrix} \tag{F.4}$$

and the controlled outputs are

$$\mathbf{y}_c = \begin{bmatrix} w_{tip2} \\ w_{tip1} \\ \theta_{tip2} \\ \theta_{tip1} \end{bmatrix}. \tag{F.5}$$

147

The state vector $\mathbf{x}$ is defined as

$$
\mathbf{x} = \begin{bmatrix}
x_{20} \\
x_{10} \\
x_{21} \\
x_{11} \\
x_{22} \\
x_{12} \\
\dot{x}_{20} \\
\dot{x}_{10} \\
\dot{x}_{21} \\
\dot{x}_{11} \\
\dot{x}_{22} \\
\dot{x}_{12} \\
\dot{\theta}_{1_f} \\
\dot{\theta}_{2_f}
\end{bmatrix} \tag{F.6}
$$

where x_{ij} corresponds to the jth mode of subsystem i, and $\dot{\theta}_{1_f}$ and $\dot{\theta}_{2_f}$ are the states corresponding to the rate filters. The system matrices are

$$
\mathbf{A} = 1000 \times \begin{bmatrix} \mathbf{A}_1 & \mathbf{A}_2 \end{bmatrix} \tag{F.7}
$$

$$
\mathbf{A}_1 = \begin{bmatrix}
0 & 0 & 0 & 0 & 0 & 0 & 0.0010 \\
0 & 0 & 0 & 0 & 0 & 0 & 0 \\
0 & 0 & 0 & 0 & 0 & 0 & 0 \\
0 & 0 & 0 & 0 & 0 & 0 & 0 \\
0 & 0 & 0 & 0 & 0 & 0 & 0 \\
0 & 0 & 0 & 0 & 0 & 0 & 0 \\
0 & 0 & 0 & 0 & 0 & 0 & 0 \\
0 & 0 & 0 & 0 & 0 & 0 & 0 \\
0 & 0 & -0.3036 & 0 & 0 & 0 & 0 \\
0 & 0 & 0 & -0.5540 & 0 & 0 & 0 \\
0 & 0 & 0 & 0 & -2.0285 & 0 & 0 \\
0 & 0 & 0 & 0 & 0 & -3.2812 & 0 \\
0 & 0 & 0 & 0 & 0 & 0 & 0 \\
0 & 0 & 0 & 0 & 0 & 0 & 0.0701
\end{bmatrix} \tag{F.8}
$$

$$
\mathbf{A}_2 \;=\; \begin{bmatrix}
0 & 0 & 0 & 0 & 0 & 0 & 0 \\
0.001 & 0 & 0 & 0 & 0 & 0 & 0 \\
0 & 0.0010 & 0 & 0 & 0 & 0 & 0 \\
0 & 0 & 0.0010 & 0 & 0 & 0 & 0 \\
0 & 0 & 0 & 0.0010 & 0 & 0 & 0 \\
0 & 0 & 0 & 0 & 0.0010 & 0 & 0 \\
0 & 0 & 0 & 0 & 0 & 0 & 0 \\
0 & 0 & 0 & 0 & 0 & 0 & 0 \\
0 & -0.0002 & 0 & 0 & 0 & 0 & 0 \\
0 & 0 & -0.0033 & 0 & 0 & 0 & 0 \\
0 & 0 & 0 & -0.0027 & 0 & 0 & 0 \\
0 & 0 & 0 & 0 & -0.0063 & 0 & 0 \\
0.051 & 0 & 0.6182 & 0 & 0.7071 & -0.063 & 0 \\
-0.051 & 0.3620 & 0.4781 & 0.5599 & -0.6249 & 0 & -0.063
\end{bmatrix} \tag{F.9}
$$

$$
\mathbf{B} \;=\; \begin{bmatrix}
0 & 0 \\
0 & 0 \\
0 & 0 \\
0 & 0 \\
0 & 0 \\
0 & 0 \\
0 & 1.1137 \\
0.8056 & -0.8056 \\
0 & 5.7506 \\
9.8209 & 7.5953 \\
0 & 8.8939 \\
11.2331 & -9.9268 \\
0 & 0 \\
0 & 0
\end{bmatrix} \tag{F.10}
$$

$$\mathbf{C}_s \; = \; \begin{bmatrix} -0.6790 & 0 & 1.1137 & 0 & 0 \\ 0 & 0.4195 & 0 & 0 & 0 \\ -0.1733 & 0 & -7.6187 & 0 & 0 \\ 0 & 0.6040 & 0 & 0 & 0 \\ 0.3145 & 0 & 6.7744 & 0 & 0 \\ 0 & -0.8520 & 0 & 0 & 0 \\ 0 & 0 & 0 & 0 & 1.1137 \\ 0 & 0 & 0 & 0.8056 & -0.8056 \\ 0 & 0 & 0 & 0 & 5.7506 \\ 0 & 0 & 0 & 9.8209 & 7.5953 \\ 0 & 0 & 0 & 0 & 8.8939 \\ 0 & 0 & 0 & 11.2331 & -9.9268 \\ 0 & 0 & 0 & 0 & 0 \\ 0 & 0 & 0 & 0 & 0 \end{bmatrix}^{\mathrm{T}} \tag{F.11}$$

$$\mathbf{C}_c \; = \; \begin{bmatrix} -0.6790 & 0 & 1.1137 & 0 \\ 0 & 0.4195 & 0 & 0.8056 \\ -0.1733 & 0 & -7.6187 & 0 \\ 0 & 0.6040 & 0 & -7.5953 \\ 0.3145 & 0 & 6.7744 & 0 \\ 0 & -0.8520 & 0 & 9.9268 \\ 0 & 0 & 0 & 0 \\ 0 & 0 & 0 & 0 \\ 0 & 0 & 0 & 0 \\ 0 & 0 & 0 & 0 \\ 0 & 0 & 0 & 0 \\ 0 & 0 & 0 & 0 \\ 0 & 0 & 0 & 0 \\ 0 & 0 & 0 & 0 \end{bmatrix}^{\mathrm{T}} . \tag{F.12}$$

F.1.2 Gain Matrices

The corresponding discrete gain matrices for 60.0 Hz sampling are

$$
\mathbf{L}_d \;=\;
\begin{bmatrix}
-0.0001 & -0.0001 & -0.1397 & -0.0073 & 0.0076 \\
0.0002 & 0.0000 & 0.0695 & 0.1055 & -0.0075 \\
0.0001 & 0.0000 & -0.0076 & 0.0013 & -0.0270 \\
0.0003 & 0.0004 & -0.0043 & 0.0030 & -0.0005 \\
0.0001 & 0.0003 & 0.0004 & 0.0005 & 0.0065 \\
0.0004 & -0.0003 & -0.0002 & -0.0003 & -0.0004 \\
-0.0001 & 0.0010 & -0.3781 & -0.0193 & 0.0190 \\
0.0007 & -0.0009 & 0.2314 & 0.1406 & -0.0152 \\
0.0031 & 0.0164 & 0.1610 & 0.0274 & -0.1156 \\
0.0319 & 0.0258 & 0.0628 & -0.0464 & 0.0636 \\
-0.0038 & 0.0221 & -0.0499 & 0.0001 & -0.1379 \\
0.0251 & -0.0235 & -0.0139 & 0.0325 & -0.0421 \\
0.4525 & -0.0096 & 0.4559 & 0.0603 & 0.1197 \\
-0.0096 & 0.5231 & 0.2278 & -0.3435 & -0.5922 \\
0.0001 & 0.0001 & 0.0926 & 0.0047 & 0.0014 \\
0.0000 & -0.0000 & 0.0246 & 0.0461 & -0.0037 \\
0.0002 & 0.0013 & -0.0656 & -0.0112 & 0.2376 \\
0.0001 & 0.0000 & 0.0887 & 0.0045 & -0.0002 \\
0.0001 & -0.0003 & 0.0227 & 0.0453 & -0.0039 \\
0.0004 & 0.0007 & -0.0459 & -0.0083 & 0.1777 \\
-0.0000 & -0.0001 & 0.0024 & 0.0003 & 0.0146
\end{bmatrix}
\tag{F.13}
$$

$$\mathbf{K}_d \;=\; \begin{bmatrix} -0.6723 & 58.8643 \\ 31.7784 & 0 \\ 59.3503 & -86.7588 \\ -85.5838 & 0 \\ -6.5682 & 30.7111 \\ 15.5604 & 0 \\ 5.2245 & 24.3039 \\ 15.5783 & 0 \\ -1.0358 & 5.0660 \\ -0.6785 & 0 \\ -0.1619 & -1.0293 \\ 0.0130 & 0 \\ 0 & 0 \\ 0 & 0 \end{bmatrix}^{\mathrm{T}} \tag{F.14}$$

$$\mathbf{K}_d^{filter} \;=\; \begin{bmatrix} 0.7727 & 0 \\ 1.1630 & 0 \\ 2.0618 & 0 \\ 0.9176 & 0 \\ -0.3286 & 0 \\ 0.0467 & 0.8995 \\ 0.0722 & 1.4695 \\ 0.1048 & 2.8389 \\ -0.0493 & 1.7221 \\ -0.2352 & 0.2615 \end{bmatrix}^{\mathrm{T}} \tag{F.15}$$

where $\mathbf{L}_d$ is the estimator gain matrix with the delay modelled, $\mathbf{K}_d$ is the feedback gain on the plant state, and $\mathbf{K}_d^{filter}$ is the feedback gain on the filter states.

F.2 Mini-Manipulator

F.2.1 Model

The equations of motion for the mini-manipulator tip dynamics are given by

$$\dot{\mathbf{x}}_3 = \mathbf{A}_3\mathbf{x}_3 + \mathbf{B}_3^u\mathbf{u}_3(t)$$

$$\mathbf{z}_3 = \mathbf{C}_3^z\mathbf{x}_3 \tag{F.16}$$

$$\tag{F.17}$$

where

$$\mathbf{x}_3 = \begin{bmatrix} x_{m_T} \\ y_{m_T} \\ \dot{x}_{m_T} \\ \dot{y}_{m_T} \end{bmatrix} \tag{F.18}$$

$$\mathbf{u}_3 = \begin{bmatrix} F_x \\ F_y \end{bmatrix} \tag{F.19}$$

$$\mathbf{A}_3 = \begin{bmatrix} 0 & 0 & 1 & 0 \\ 0 & 0 & 0 & 1 \\ 0 & 0 & 0 & 0 \\ 0 & 0 & 0 & 0 \end{bmatrix} \tag{F.20}$$

$$\mathbf{B}_3^u = \begin{bmatrix} 0 & 0 \\ 0 & 0 \\ \frac{1}{m_T} & 0 \\ 0 & \frac{1}{m_T} \end{bmatrix} \tag{F.21}$$

and $m_T = 0.065$ kg.

F.2.2 Gain Matrices

The corresponding controller is of the form

$$\mathbf{F} = -\mathbf{K}_p\mathbf{x} - \mathbf{K}_v\dot{\mathbf{x}} \tag{F.22}$$

where

$$\mathbf{F} = \begin{bmatrix} F_x \\ F_y \end{bmatrix} \tag{F.23}$$

$$\mathbf{x} \;=\; \begin{bmatrix} x_{m_T} \\ y_{m_T} \end{bmatrix} \tag{F.24}$$

$$\dot{\mathbf{x}} \;=\; \begin{bmatrix} \dot{x}_{m_T} \\ \dot{y}_{m_T} \end{bmatrix}. \tag{F.25}$$

$\mathbf{K}_p$ and $\mathbf{K}_v$ are the 2×2 gain matrices

$$\mathbf{K}_p \;=\; \begin{bmatrix} 91.2871 & 0 \\ 0 & 91.2871 \end{bmatrix} \tag{F.26}$$

$$\mathbf{K}_v \;=\; \begin{bmatrix} 3.4449 & 0 \\ 0 & 3.4449 \end{bmatrix}. \tag{F.27}$$

The discrete gain matrices for 180.0 Hz sampling are

$$\mathbf{K}_{p_d} \;=\; \begin{bmatrix} 78.8009 & 0 \\ 0 & 78.8009 \end{bmatrix} \tag{F.28}$$

$$\mathbf{K}_{v_d} \;=\; \begin{bmatrix} 3.2006 & 0 \\ 0 & 3.2006 \end{bmatrix}. \tag{F.29}$$

Bibliography

[1] P. Kumar, P. Truss, and C. G. Wagner-Bartak. System design features of the space shuttle remote manipulator. In *Proceedings of the Fifth World Congress on Theory of Machines and Mechanisms*, pages 839–842. American Society of Mechanical Engineers, 1979.

[2] P. K. Nguyen, R. Ravindran, R. Carr, and D. M. Gossiain. Structural flexibility of the shuttle remote manipulator system mechanical arm. In *Proceedings of the AIAA Guidance, Navigation and Control Conference*, pages 246–256, San Diego, CA, August 1982.

[3] R. Ravindran and R. H. Doetsen. Design aspects of the shuttle remote manipulator control. In *Proceedings of the AIAA Guidance, Navigation and Control Conference*, pages 456–465, San Diego, CA, August 1982.

[4] Eric Schmitz. *Experiments on the End-Point Position Control of a Very Flexible One-Link Manipulator.* PhD thesis, Stanford University, Department of Aeronautics and Astronautics, Stanford, CA 94305, June 1985. Also published as SUDAAR 548.

[5] Celia M. Oakley. *Experiments in Modelling and End-Point Control of Two-Link Flexible Manipulators.* PhD thesis, Stanford University, Department of Mechanical Engineering, Stanford, CA 94305, April 1991.

[6] Robert H. Cannon, Jr. and Eric Schmitz. Initial Experiments on the End-Point Control of a Flexible One-Link Robot. *The International Journal of Robotics Research*, 3(3):62–75, Fall 1984.

[7] James A. Maples. *Force Control of Robotic Manipulators with Structural Flexibility.* PhD thesis, Stanford University, Department of Electrical Engineering, Stanford, CA 94305, June 1985. Also published as SUDAAR 549.

[8] Daniel Mark Rovner. *Experiments in Adaptive Control of a Very Flexible One-Link Manipulator.* PhD thesis, Stanford University, Department of Aeronautics and Astronautics, Stanford, CA 94305, August 1987.

[9] Lawrence Alder. *Control of a Flexible-Link Robotic Arm Manipulating An Unknown Dynamic Payload.* PhD thesis, Stanford University, Stanford, CA 94305, February 1993. Also published as SUDAAR 632.

[10] C. M. Oakley and R. H. Cannon, Jr. Initial Experiments on the Control of a Two-Link Manipulator with a Very Flexible Forearm. In *Proceedings of the American Control Conference*, Atlanta, GA, June 1988.

[11] C. M. Oakley and R. H. Cannon, Jr. End-Point Control of a Two-Link Manipulator with a Very Flexible Forearm: Issues and Experiments. In *Proceedings of the American Control Conference*, Pittsburgh, PA, June 1989.

[12] C. M. Oakley and R. H. Cannon, Jr. Theory and Experiments in Selecting Mode Shapes for Two-Link Flexible Manipulators. In *Proceedings of the First International Symposium on Experimental Robotics*, Montréal, Canada, June 1989.

[13] C. M. Oakley and R. H. Cannon, Jr. Equations of Motion for an Experimental Planar Two-Link Flexible Manipulator. In *Proceedings of the ASME Winter Annual Meeting*, San Francisco, CA, December 1989.

[14] C. M. Oakley and R. H. Cannon, Jr. Anatomy of an Experimental Two-link Flexible Manipulator under End-point Control. In *Proceedings of the IEEE Conference on Decision and Control*, Honolulu, HI, December 1990.

[15] E. Bayo, R. Movaghar, and M. Medus. Inverse dynamics of a single-link flexible robot. analytical and experimental results. *International Journal of Robotics and Automation*, 3(3):150–157, 1988.

[16] E. Bayo and R. Ledesma. Non-recursive lagrangian solution of the non-causal inverse dynamics of flexible multibody systems: The planar case. *International Journal for Numerical Methods in Engineering*, 36(16):2725–2741, 1993.

[17] E. Bayo, H. Moulin, and B. Paden. Existence and uniqueness of solutions of the inverse dynamics of multilink flexible arms: Convergence of a numerical scheme. *Journal of Robotic Systems*, 10(1):73–102, 1993.

[18] W. Book and D. Kwon. Tracking control of a nonminimum-phase flexible manipulator. In *Modelling and Control of Compliant and Rigid Motion Systems*, pages 27–37. American Society of Mechanical Engineers, 1991.

[19] S. Yurkovich and J. Watkins. Vibration control for slewing flexible structures. In *Proceedings of the American Control Conference*, Green Valley AZ, 1992.

[20] Neil C. Singer and Warren P. Seering. Preshaping command inputs to reduce system vibrations. *ASME Journal of Dynamic Systems, Measurement, and Control*, March 1990.

[21] N. Singer and W. Seering. Experimental verification of command shaping methods for controlling residual vibration in flexible robots. In *Proceedings of the American Control Conference*, pages 1738–1744. American Automatic Control Council, 1990.

[22] W. Book and D. Magee. Implementing modified command filtering to eliminate multiple modes of vibration. In *Proceedings of the 1993 American Control Conference*, pages 2700–2704, San Francisco, CA, June 1993. American Automatic Control Council.

[23] W. Book and D. Magee. Eliminating multiple modes of vibration in a flexible manipulator. In *Proceedings of the IEEE Conference on Robotics and Automation*, pages 474–479. IEEE, 1993.

[24] Wen-Wei Chiang. *Rapid Precise End Point Control of a Wrist Carried by a Flexible Manipulator*. PhD thesis, Stanford University, Department of Aeronautics and Astronautics, Stanford, CA 94305, March 1986. Also published as SUDAAR 550.

[25] Scott W. Tilley and Robert H. Cannon, Jr. End Point Position and Force Control of a Flexible Manipulator with a Quick Wrist. In *Proceedings of the AIAA Guidance, Navigation and Control Conference*, pages 41–49, Williamsburg, VA, August 1986.

[26] Raymond H. Kraft. *Experiments in End-Point Control of a Flexible Robot with a Mini-Manipulator.* PhD thesis, Stanford University, Department of Aeronautics and Astronautics, Stanford, CA 94305, May 1989. Also published as SUDAAR 581.

[27] Brian L. Andersen. *Experiments in End-Point Position and Force Control of a Minimanipulator on a Flexible-Drive Manipulator.* PhD thesis, Stanford University, Department of Aeronautics and Astronautics, Stanford, CA 94305, September 1990. Also published as SUDAAR 596.

[28] S. D. Ims, W. L. Ballhaus, L. J. Alder, and S. M. Rock. State-space model concatenation: A new model concatenation approach. In *ARL Memo*, 1994.

[29] Ross Koningstein. *Experiments in Cooperative-Arm Object Manipulation with a Two-Armed Free-Flying Robot.* PhD thesis, Stanford University, Department of Aeronautics and Astronautics, Stanford, CA 94305, October 1990. Also published as SUDAAR 597.

[30] Vincent W. Chen. *Experiments in Adaptive Control of Multiple Cooperating Manipulators on a Free-Flying Space Robot.* PhD thesis, Stanford University, Stanford, CA 94305, December 1992. Also published as SUDAAR 631.

[31] S. Schneider. *Experiments in the Dynamic and Strategic Control of Cooperating Manipulators.* PhD thesis, Stanford University, Stanford, CA 94305, September 1989. Also published as SUDAAR 586.

[32] Wind River Systems, Inc., 1351 Ocean Ave., Emeryville, CA 94608. *VxWorks User's Manual*, 1989.

[33] Real-Time Innovations, Inc., 954 Aster, Sunnyvale, CA 94086. *ControlShell: Object-Oriented Framework for Real-Time System Software User's Manual*, 4.0a edition, June 1991.

[34] C. Moler, J. Little, S. Bangert, and S. Kleiman. *PRO-MATLAB User's Guide for Sun Workstations.* The MathWorks, Inc., Natick, MA, January 1990. Version 3.5-SUN.

[35] Real-Time Innovations, Inc., 954 Aster, Sunnyvale, CA 94086. *StethoScope Real-Time Graphical Monitoring and Data Collection Utility User's Manual*, 3.2 edition, December 1990.

[36] Y. Takahashi, M. Rabins, and D. Auslander. *Control and Dynamic Systems*. Addison-Wesley Publishing Company, Menlo Park, CA, 1970.

[37] Leonard Meirovitch. *Elements of Vibration Analysis*. Macmillan Series in Applied Mechanics. MacGraw-Hill Book Company, New York, NY, second edition, 1986.

[38] William C. Dickson. *Experiments in Cooperative Manipulation of Objects by Free-Flying Robot Teams*. PhD thesis, Stanford University, Department of Aeronautics and Astronautics, Stanford, CA 94305, December 1993. Also published as SUDAAR 643.

[39] Bong Wie. *On the Modeling and Control of Flexible Space Structures*. PhD thesis, Stanford University, Department of Aeronautics and Astronautics, Stanford, CA 94305, June 1981. Also published as SUDAAR 525.

[40] Rhonda Slattery. *Optimal Control of Closed Chain Robotic Systems*. PhD thesis, Stanford University, Stanford, CA 94305, June 1991.

[41] Ronald C. Rosenberg and Dean C. Karnopp. *Introduction to Physical System Dynamics*. McGraw-Hill Series in Mechanical Engineering. McGraw-Hill, New York, NY, 1983.

[42] J. Rastegar, Q. Tu, M. Mattice, and N. Coleman. Trajectory pattern method applied to a nonlinear flexible pointing system. In *Proceedings of the American Control Conference*, pages 1622–1626, San Francisco, CA, June 1993. American Automatic Control Council.

[43] Q. Tu, J. Rastegar, and F. Tangerman. Trajectory synthesis and inverse dynamics formulation for minimal vibrational excitation for flexible structures based on trajectory patterns. In *Proceedings of the American Control Conference*, pages 2716–2720, San Francisco, CA, June 1993. American Automatic Control Council.

[44] S. P. Bhat and D. K. Miu. Precise point-to-point positioning control of flexible structures. *ASME Journal of Dynamic Systems, Measurement, and Control*, 112:667–674, 1990.

[45] K. Hillsley and S. Yurkovich. Vibration control of a two-link flexible robot arm. In *Proceedings of the 1991 IEEE International Conference on Robotics and Automation*, Sacramento CA, April 1991.

[46] Arthur E. Bryson, Jr. and Yu-Chi Ho. *Applied Optimal Control: Optimization, Estimation, and Control.* Hemisphere Publishing Corporation, 1025 Vermont Ave., N.W., Washington, D.C., 1975. Revised Printing.

[47] Narendra K. Gupta. Frequency-shaped cost functionals: Extension of linear-quadratic-gaussian design methods. *AIAA Journal of Guidance and Control*, 3(6):529–535, November–December 1980.

[48] Gene F. Franklin, J. David Powell, and Abbas Emami-Naeini. *Feedback Control of Dynamic Systems.* Addison-Wesley, Reading, MA, June 1986.

[49] E. F. Crawley and J. De Luis. Use of piezoelectric actuators as elements of intelligent structures. *AIAA Journal*, 5(1):60–66, 1980.

[50] John J. Craig. *Introduction to Robotics Mechanics and Control.* Addison-Wesley, Reading, MA, 1986.

[51] R. E. Kalman and R. S. Bucy. New results in linear filtering and prediction theory. *ASME Transactions*, pages 95–108, March 1961.

[52] W. Haeussermann. Saturn launch vehicle's navigation guidance and control system. *Automatica*, 7:537–556, 1971.

[53] G. T. Schmidt. Closed-loop control of stochastic non-linear systems. *Automatica*, 7:557–566, 1971.

[54] A. E. Bryson Jr. Optimal control and estimation. In *Stanford University AA278B Course Notes*, 1991.

[55] Gene F. Franklin, J. David Powell, and Michael Workman. *Digital Control of Dynamic Systems.* Series in Electrical and Computer Engineering: Control Engineering. Addison-Wesley, Reading, MA, second edition, 1990.